

RICE UNIVERSITY

**Engineering Deep Brain Stimulation as a Treatment for
Parkinson's Disease: from Models to Materials**

by

Samantha Rose Summerson

A THESIS SUBMITTED
IN PARTIAL FULFILLMENT OF THE
REQUIREMENTS FOR THE DEGREE

Doctor of Philosophy

APPROVED, THESIS COMMITTEE:

Dr. Behnaam Aazhang, *Chair*
J.S. Abercrombie Professor of Electrical
and Computer Engineering

Dr. Richard Baraniuk
Vice E. Cameron Professor of Electrical
and Computer Engineering

Dr. Caleb T. Kemere
Assistant Professor of Electrical and
Computer Engineering

Dr. Steve Cox
Professor of Computational and Applied
Mathematics

Dr. Jacob T. Robinson
Assistant Professor of Electrical and
Computer Engineering
HOUSTON, TEXAS

APRIL 2014

ABSTRACT

Engineering Deep Brain Stimulation as a Treatment for Parkinson's Disease: from
Models to Materials

by

Samantha R. Summerson

This thesis analyzes deep brain stimulation (DBS) as a treatment for the motor symptoms of Parkinson's disease (PD) at multiple levels. Although this treatment is currently used on human patients, little is understood about the mechanism of action which allows patients to experience therapeutic benefits. The work here investigates efficacy of DBS in computational and experimental manners in order to enhance the understanding of the effects on neural activity and behavior. First, I examine computational models of the nuclei within the motor circuit of the brain and used these models to test novel electrical stimulation signal designs. I show that irregular spacing of stimulation pulses allows for increased variability in neuronal firing rate responses within the basal ganglia. Also, I develop a model of the stimulation-frequency-dependent nature of antidromic spiking induced in the motor cortex as a result of DBS. Second, I use the hemi-Parkinsonian rat model to demonstrate motor and cognitive behavioral effects of DBS in the globus pallidus internus (GPi). The work validates this animal model for translational research on DBS of the GPi and demonstrates results consistent with reports for DBS of the subthalamic nucleus (STN) in the same model. Additionally I study recorded neural activity in the motor cortex while stimulating the STN in order to characterize the corresponding changes in neural activity. I found that regular and irregular stimulation patterns both decrease Parkinsonian entropic noise in the output layer of the motor cortex, with irregular stimulation having the greatest benefit towards reducing this noise. Third,

I consider a new material for its biocompatibility and applicability as a material for stimulating electrodes. In the rat model that I previously validated, I verify that behavioral results using a stimulating electrode made from carbon nanotube fibers (CNTf) match results from previous experiments using standard platinum iridium (PtIr) electrodes. Additionally, it is shown that CNTf electrodes produce lower inflammation, gliosis and damage to the blood brain barrier. Together, all three aspects of the work demonstrate significant contributions to the functionality and engineering of DBS as a neuromodulation therapy for PD.

ACKNOWLEDGEMENTS

I would like to begin by giving thanks to my primary advisor, Dr. Behnaam Aazhang, who allowed me to embark on this crazy neuroengineering journey and who has helped me grow academically in so many ways. Thank you for giving me this opportunity and believing in me. This work would not have been possible without the guidance and support of Dr. Caleb Kemere, who has been a advisor, cheerleader and confidant throughout this process. I couldn't have done it without you.

To all my fellow Ph.D. students, thank you for filling my time here at Rice with wonderful memories. Together we have survived a hurricane, government shutdown, and many sticky summers. David, you've been there since the beginning and I will continue to chase you with hugs the rest of my days. Achal, I wish my mind worked more like yours and I look forward to seeing you in scrubs. Corina, you have been like a sister - you have seen all sides of me and I can't thank you enough for your never-ending compassion. Eva, I have looked up to you since we both arrived broke in Houston and I can't wait to see the amazing things ahead of you. Rakesh, you have tested the limits of my patience in ways I didn't know were possible but at the end of it all I'm happy to affectionately refer to you as my little (academic) brother. Flavia, this final year of graduate school has been a push and I couldn't have survived it without your mentorship and friendship.

My deepest, most sincere thanks go to my family who have shaped me into the person I am and have never stopped believing in me.

To Thomas Frederick and Rose Violet Summerson: you taught me how to love and how to dream. I love and miss you.

Pedro, your support has been unwavering and has carried me to the finish line. There are not enough words to describe all that you have given me. Thank you for all your faith, optimism and love.

Contents

1	Introduction	1
2	Background and Related Literature	5
3	Computational Modeling	11
3.1	Cell Models	12
3.2	Nuclei Models	17
3.3	Regular and Irregular DBS	19
3.4	Mixture of Response	21
3.5	Antidromic Spiking	24
4	Hemi-Parkinsonian Rodent Model	28
4.1	Animal Model	29
4.2	Behavior Tests	33
4.2.1	Rotation Test	33
4.2.2	Cylinder Test	35
4.2.3	Open Field Task	36
4.2.4	Reaction Time Task	38
4.2.5	Sucrose Preference Test	40
4.3	Behavioral Results	42
4.3.1	Motor Asymmetry	42
4.3.2	Ambulation	45
4.3.3	Hypokinesia	47
4.3.4	Cognition and Mood	48
4.4	Correlations Between Tasks	50

4.5	Conclusions for GPi-DBS	51
5	Cortical Recording with DBS	53
5.1	Microdrive Design	54
5.2	Microdrive Implant and Placement of Electrodes	55
5.3	Regular and Irregular Stimulation	57
5.4	Data Capturing and Processing	58
5.5	Spike Results	60
5.6	LFP Results	67
6	Carbon Nanotube Fiber Electrodes	74
6.1	Fabrication	76
6.2	Stimulating Electrode	77
6.3	Recording Electrode	78
6.4	Histology	80
6.4.1	Acute Histology	80
6.4.2	Chronic Histology	83
7	Conclusions	93
	References	95

List of Figures

2.1 Major pathways within the basal ganglia, and the pathways for the main input and output nuclei for the basal ganglia. The GABAergic pathways (inhibitory) are shown with solid lines and the glutamatergic pathways (excitatory) are with dotted lines. The dopaminergic projection from the substantia nigra pars compacta (SNc) to the striatum is depicted with a dashed line. Marked with gray shading are the two main target nuclei, GPi (a.k.a. the entopeduncular nucleus in the rat brain) and STN, for DBS to treat the motor symptoms of PD.	6
3.1 Cartoon depiction of antidromic versus orthodromic spikes. Spikes traveling in the normal direction of propagation are known as orthodromic spikes. They travel along the axon to the axon terminal that connects to the post-synaptic cell. Conversely, antidromic spikes travel in the opposite direction and may collide with the normal (orthodromic) spikes.	13
3.2 Cartoon showing synaptic connectivity for a small network with four model neurons per structure. Excitatory connections are depicted with solid lines and inhibitory connections are depicted with dotted lines. The dark circle in the middle of the STN neurons represents the DBS electrode. The white-colored cells in Layer V - M1 are the IN cells, where each IN cell forms a feedback loop with one of the PY cells.	18
3.3 Example activity of GPi, GPe, and STN model cells. The left column depicts activity when the system model is in the normal (a.k.a. healthy) state and the right column depicts activity when the system model is in the Parkinsonian state.	20

3.4	Distribution of changes in firing rates experienced by neurons while stimulation is administered, relative to the firing rates from the preceding time period without stimulation.	22
3.5	Average firing rate of the PY cells with regular DBS administered to the efferent STN cells at various frequencies. Values are the mean firing rate \pm S.D.	26
3.6	Average firing rate of the IN cells with regular DBS administered to the efferent STN cells at various frequencies. Values are the mean firing rate \pm S.D.	27
3.7	ISI entropy computed from the cortical computational model.	27
4.1	Approximate locations of the electrode positions for all subjects with one marker per subject and the EP (GPi) shaded in gray. Each image is a depiction of a coronal section that is 2-4 mm lateral and 7-9 mm ventral from Bregma, with solid and dashed lines demarcating neighboring nuclei. (a) Section is -2.16 mm posterior to Bregma. (b) Section is -2.28 mm posterior to Bregma. (c) Section is -2.4 mm posterior to Bregma. (d) Section is -2.52 mm posterior to Bregma. (e) Section is -2.64 mm posterior to Bregma. (f) Section is -2.76 mm posterior to Bregma.	31
4.2	Representative image of THir cells in the SNc on the left lateral and right lateral sides of a 50 μ m slice. Scale bar is 1 mm. TH positive cells appear darker than the surrounding tissue.	32
4.3	Photo of the cylindrical environment used in the rotation task. The cylinder was kept in an isolation chamber to limit distractions.. The cable from the stimulator was mounted on the the ceiling of the isolation chamber, so as not to impair the rats' movements.	33
4.4	Cartoon describing a block of stimulation epochs for the rotation test. A two minute period of stimulation is represented with a numbered white box, which is bordered by black boxes represented the three minute control periods where no stimulation is administered. Eleven conditions are tested, which includes one test of baseline stimulation with no stimulation, and the order of the conditions is randomized per test.	34
4.5	Example of rotation of rat over time.	35

4.6	Image of a subject rearing against the walls of an acrylic cylinder, as in the cylinder test.	36
4.7	Image of a subject in the open field environment.	37
4.8	Depiction of the RT task. (a) The rat places its head above milk well for a random time interval, with an early head withdrawl termed a premature response. Time to correctly withdrawl head at end of interval is the reaction time. (b) Following correct head withdrawl a lever is extended and the time until lever depression is the motor time.	38
4.9	Image of a subject performing a sucrose preference test. Two identical bottles are presented to the subject and the volume of fluid consumed from each bottle is used to determine the anhedonic state.	41
4.10	The normalized rotation rate and total angular distance traveled are presented above for the rotation task using methamphetamine and apomorphine. Different alphabetical characters indicate significant differences determined from post-hoc LSD tests ($p < 0.05$).	43
4.11	The ipsilateral to total paw touch ratio in the cylinder task. The number of times the rat reared against the side of the cylinder environment and made contact using each forelimb was recorded. The total number of times the rat used the paw ipsilateral to the 6-OHDA lesion was divided by the total number paw touches to create the paw touch ratio. Different alphabetical characters indicate significant differences determined from post-hoc LSD tests ($p < 0.05$).	45
4.12	Total number of outer squares traversed and number of rears during open field task. Different alphabetical characters indicate significant differences determined from post-hoc LSD tests ($p < 0.05$).	46
4.13	Measures of akinesia and bradykinesia. Bars represent mean \pm SEM. Mean MT and RT are shown on the left and right, respectively ($n = 10$). Significant differences were found between states. * $p < 0.05$ and ** $p < 0.01$	47
4.14	Measures of cognition. Data is shown as mean \pm SEM. (a) Mean PPR in the RT task ($n = 10$). The mean PPR across the states were determined to be significantly different. * $p < 0.05$ and ** $p < 0.01$. (b) Mean SPI ($N = 10$). The mean SPI across the states was not equal. * $p < 0.05$	49
5.1	Views of a microdrive designed for bilateral M1 recording and STN-DBS.	56

5.2	Arduino Uno used to generate irregular DBS pulse patterns.	59
5.3	Example average spike waveforms acquired from well-isolated single neurons during <i>in vivo</i> recording.	61
5.4	Average <i>in vivo</i> firing rate of neurons with and without stimulation administered. For reference, the results from the computational model are also plotted here. Values reported are the mean \pm SEM.	61
5.5	62
5.6	Empirical pmf of the ISI for the healthy state, computed using activity from the intact hemisphere.	64
5.7	Empirical pmf of the ISI for the Parkinsonian state. The ISIs for the Parkinsonian state were computed using activity from the lesioned hemisphere.	64
5.8	PSTH for 40 Hz irregular DBS. There is a peak in the distribution of spike times following the stimulus which indicates stimulus-locked antidromic firing of the M1 cell.	65
5.9	ISI pmf for 40 Hz irregular DBS.	66
5.10	ISI pmf for 130 Hz irregular DBS.	66
5.11	ISI entropy under multiple conditions, computed with pmfs using 10 ms bins.	67
5.12	Example traces over a 10 s time window of a (a) raw LFP signal and (b) low-pass filtered LFP signal.	68
5.13	Normalized power spectra computed by using the multitaper estimation of the power spectra over the frequency window [0, 100] Hz. . . .	71
5.14	Comparison of power spectra under four different stimulation conditions.	72
5.15	Frequency at which the peak normalized power in the β -band (13-30 Hz) occurs. Error bars are SEM.	72
5.16	Peak normalized power in the β -band (13-30 Hz). Error bars are SEM.	73
5.17	Total power in the β -band (13-30 Hz). Error bars are SEM.	73

6.1	<i>In-vivo</i> characterization of CNT fiber electrodes for DBS: a) 6-OHDA dopaminergic lesion was induced on the right hemisphere. CNT fiber electrodes were implanted in the entopeduncular nucleus (EP) ipsilateral to the lesion. Commercial PtIr electrodes were in the left EP, and used as control; b) Results of the metamphetamine rotation test: average normalized rotation rate of a population of 4 Long-Evans rats implanted with CNT fiber electrodes and comparison with PtIr electrodes (error bars: SEM). Repeated measures ANOVA showed that there was significant difference between treatment conditions ($p < 0.05$). Pairwise comparison across frequencies was performed with post-hoc least square difference (LSD, $p < 0.05$). Frequencies are significantly different when do not share a letter.	78
6.2	Average single-unit waveform recorded using a CNTf electrode. The shaded region indicates the S.D. of the mean waveform values.	80
6.3	Example clusters formed by plotting the peak waveform amplitudes recorded across three of the four channels from two different tetrodes. The z-axis shows the peak amplitude on either the CNTf channel of a CNTf tetrode or on a NiCr channel of a standard tetrode. The x- and y-axes are peak waveform amplitudes from two of the NiCr channels in the same tetrode as the channel shown on the z-axis.	81
6.4	Raw LFP signal from a CNTf channel and a NiCr channel of the same tetrode.	81
6.5	Hystological analysis of the acute damage to the BBB due to electrode insertion: a) CNT fiber electrode at the entry location, and b) at the tip; c) PtIr electrode at the entry location and d) at the tip (scale bars: 100 μ m; error bars: SEM).	84
6.6	Fluorescence intensity profiles from the center of the electrode at the entry point and at the tip (error bars: SEM).	85
6.7	Two markers are used to characterize the gliosis that occurs after chronic implantation of the PtIr electrode. (a) Astrocyte marker (GFAP), (b) Microglia marker (Iba1), (c) Overlay with DAPI.	87
6.8	Presence of activated macrophages is used to classify the level of inflammation induced from the PtIr electrode implant. (a) General stain for activated macrophages, (b) M1 macrophages, (c) M2 macrophages, (d) Overlay image with DAPI.	88

6.9 Laminin lines the blood vessels and staining for laminin may be used to indicate damage to the BBB due to the chronic presence of a PtIr electrode. (a) Laminin, (b) Laminin and DAPI co-stain.	88
6.10 NeuN stain of tissue with PtIr implant. NeuN antibody identifies neuronal nuclei in order to label neurons. (a) NeuN, (b) NeuN and DAPI overlay. Recall that DAPI is a nuclei stain and labels all cells, including neurons.	89
6.11 Two markers are used to characterize the gliosis that occurs after chronic implantation of the CNTf electrode. (a) Astrocyte marker (GFAP), (b) Microglia marker (Iba1), (c) Overlay with DAPI.	89
6.12 Presence of activated macrophages is used to classify the level of inflammation induced from the CNTf electrode implant. (a) General stain for activated macrophages, (b) M1 macrophages, (c) M2 macrophages, (d) Overlay image with DAPI.	90
6.13 Laminin lines the blood vessels and staining for laminin may be used to indicate damage to the BBB due to the chronic presence of a CNTf electrode. (a) Laminin, (b) Laminin and DAPI co-stain.	90
6.14 NeuN stain of tissue with CNTf implant. NeuN antibody identifies neuronal nuclei in order to label neurons. (a) NeuN, (b) NeuN and DAPI overlay. Recall that DAPI is a nuclei stain and labels all cells, including neurons.	91
6.15 Fluorescence intensity profiles at increasing lateral distance from electrode tract: a) astrocytes, b) microglia, c) activated macrophages, d) M1 macrophages, e) M2 macrophages, f) laminin, g) neuronal count. Error bar: SEM	92

CHAPTER 1

Introduction

Parkinson's disease (PD) is a neurodegenerative disorder which stems from dysfunction in the basal ganglia (BG), a group of deep brain nuclei that play a prominent role in the motor circuit of the brain. This disorder follows cell loss of dopaminergic neurons in the substantia nigra pars compacta (SNc), which projects to the striatum, and the disrupted balance of excitatory and inhibitory activity in the downstream structures. When the motor symptoms of PD become pharmacologically intractable, deep brain stimulation (DBS) is a possible alternative treatment. This technique of electrical neuromodulation consists of stimulating brain structures with implanted neural electrodes which are connected to a implanted pulse generator (IPG) that is surgically placed in the pectoral region of the patient. Some have described it as a "pacemaker for the brain" [1].

There are many advantages of DBS over other surgical solutions, such as resection. The treatment is reversible, meaning that if the device is bothersome to the patient or nonfunctional, it can be removed with minimal to no damage to brain function. Surgical strategies generally involve permanently removing or destroying part of the brain and tend to have more complications [2]. DBS treatment is adjustable, so the electrical stimulation can be adapted over time to improve the responsiveness of the

patient. Also, medications can typically be reduced when DBS is effective in reducing the motor symptoms of PD, which may result in reduced side effects and improved quality of life [2].

Like any treatment, however, there are disadvantages as well. These include the limited life span of the IPG and the need to have battery replacement surgery, although some newer models have rechargeable batteries now, as well high cost and possibility of device failure, among others. Perhaps the most problematic aspect of DBS, though, is the poor mechanistic understanding of the therapeutic action of the electrical modulation on the neural activity in BG and other nuclei in the motor circuit. Although much progress has been made towards understanding what firing patterns, coherence and other neurological changes are induced by the stimulation, the sufficient conditions for therapeutic efficacy are unknown and the optimal stimulation strategy remains an open question. Also, currently two target nuclei are used for stimulation: the subthalamic nucleus (STN) and globus pallidus internus (GPi). Although the function of the these nuclei are very different, studies on which target is more efficacious are equivocal and it not understood how they each may play different roles in producing the same therapeutic end result.

This thesis seeks to add to our current understanding of DBS as a treatment for PD on multiple levels. First, I develop system-level models of important BG structures, as well as the output layer of the primary motor cortex and the thalamus, which relays information from the BG to the cortex. These models are used to examine new stimulation signal designs and their influence on firing rate changes and patterns. Biological models are an important tool for gaining insights into neural function and, in this case, serve as an effective testbed for innovative new DBS paradigms. We represent the activity of a given nucleus using a small number (< 20) of conductance-based models of individual cells. This construction allows us to consider changes occurring at both the single-unit and population level.

Second, the hemi-Parkinsonian rat model is used to study the translational aspects of GPi-DBS and novel irregular stimulation patterns for STN-DBS. There are many reasons why the rodent model is a good model to study for PD and modulation of symptoms via DBS. Unlike human and non-human primate models of PD, there is rapid access to histopathological changes and it's easier to develop longitudinal studies due to the short lifespan of the animal. The hemi-Parkinsonian rodent model has been well developed [3–16] and allows for simultaneous disease and control behavior in the same animal. No prior work had established the relationship between the stimulation parameters and measures of motor behavior for GPi-DBS in this model. To fill this knowledge gap, I consider multiple motor and cognitive metrics, and investigate the behavior tuning as a function of stimulation frequency. Since there is a large existing body of literature on STN-DBS in the hemi-Parkinsonian rodent model, we choose to switch DBS targets when considering the proposed irregular current pulse pattern for DBS and the induced changes in cortical activity. Neural activity in the output layer of the motor cortex is recorded while stimulation is administered and the resultant changes are characterized. We find that stimulation reduces pathological entropic noise and alters firing rate patterns in the cortex via the hyperdirect pathway to the STN.

Third, the same animal model is used as a vehicle for determining the biocompatibility of a potential new material for fabricating stimulating and recording electrodes. Carbon nanotube fibers are highly conductive, electrochemically stable, strong, flexible, and microscale in size. These properties make it an attractive alternative to current materials. I show that a stimulating electrode made from this material works just as well as standard commercial electrodes in terms of the therapeutic benefits achieved with GPi-DBS in the hemi-Parkinsonian rat model. Also, I show that recording electrodes made from this material achieve good signal-to-noise ratio (SNR) for single-unit and local field potential (LFP) recordings. Finally, the immunoresponse

to acute and chronic damage is characterized. It is hypothesized the that flexibility of the fiber allows it to flex with micromovements of the tissue, thus resulting in a lower negative reaction to the presence of the electrode in brain tissue.

CHAPTER 2

Background and Related Literature

The BG are an organized network of subcortical nuclei that are responsible for many aspects of brain activity. They are involved in movement, associative learning, planning, working memory and emotion. The largest nucleus of the BG is the striatum, which is mainly composed of medium spiny neurons. These are GABAergic cells, so they inhibit the cells that they synapse onto. The striatum is also the main input source of the BG, although the cortex does have a direct connection to the subthalamic nucleus (STN) and this connection is known as the hyperdirect pathway. The striatum receives input from the cortex and the substantia nigra pars compacta (SNc), which is one of the two main areas of the brain that produces dopamine. As a neurotransmitter, dopamine modulates striatal activity.

There are two major pathways throughout the BG: the direct and indirect pathway. The direct pathway is responsible for initiating and executing movement. It consists of the cortex stimulating the striatum, which inhibits the substantia nigra pars compacta (SNc) and globus pallidus internus (GPi). These targets disinhibit activity in the thalamus which in turn stimulates cortical activity that stimulates muscles. Conversely, the indirect pathway is responsible for inhibiting movement. In this pathway, the cortex stimulates the striatum, which then inhibits the globus pal-

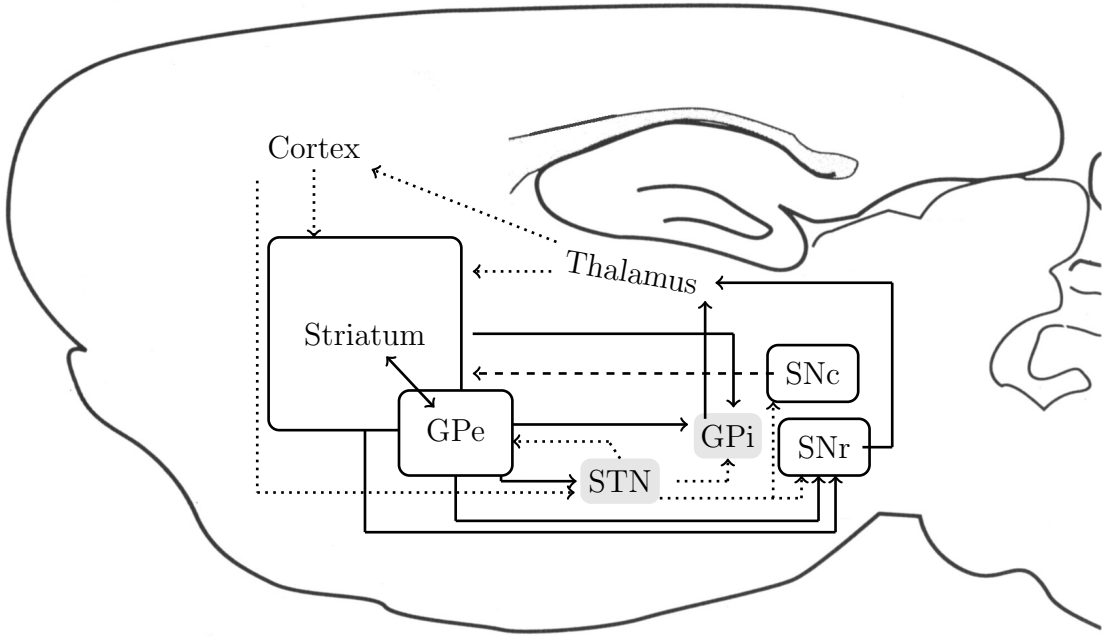


Figure 2.1: Major pathways within the basal ganglia, and the pathways for the main input and output nuclei for the basal ganglia. The GABAergic pathways (inhibitory) are shown with solid lines and the glutamatergic pathways (excitatory) are with dotted lines. The dopaminergic projection from the substantia nigra pars compacta (SNc) to the striatum is depicted with a dashed line. Marked with gray shading are the two main target nuclei, GPi (a.k.a. the entopeduncular nucleus in the rat brain) and STN, for DBS to treat the motor symptoms of PD.

latus externus (GPe). The GPe disinhibits activity in STN, which stimulates activity in the SNr and GPi. These nuclei inhibit the Thalamus, so it stimulates less the area of the cortex responsible for stimulating muscles. These pathways are depicted in Fig. 2.1.

The dopaminergic pathway from SNc to the striatum modulates the antagonist functions of the direct and indirect pathways. When there is a lack of dopamine, as in PD when the dopaminergic cells are degenerating, the direct pathway is less functional and the indirect pathway operates in overdrive. This leads to excessive inhibition of movement, which is responsible for the hypokinetic state affiliated with PD. Common motor symptoms are shaking, rigidity, difficulty initiating movement

(akinesia), difficulty executing movement (bradykinesia), and problems with gait. Late stage PD also tends to have cognitive symptoms associated with it, such as dementia and depression.

There are many pathological changes of the neural activity within the BG in the Parkinsonian state, some of which have been correlated to impaired motor movement. Throughout the BG, there is an increase in beta band power [11] and bradykinesia has been correlated with increased in beta band beta in the monkey model of PD [17]. The activity in STN, which is a glutamatergic nucleus in the indirect pathway, and GPe becomes more phasic and bursty [18]. The firing rate in GPi, the main output nucleus of the BG, significantly increases, causing increased inhibition of thalamic activity [18].

The motor symptoms of PD are commonly initially treated with Levodopa, which is a dopamine precursor that is metabolized into dopamine when taken as a pharmaceutical treatment. Over time, patients may tend to grow resistant to medication. DBS is typically recommended when drug therapy is insufficient to manage the symptoms of the disease and has been a FDA-approved treatment for PD since 2002. It is also FDA-approved for essential tremor and dystonia, and under investigation for treatment of many other neurodegenerative and neuropsychiatric disorders. The two main target nuclei for DBS to treat PD are the STN and GPi. The STN is an attractive target because it plays a unique role in regulating the BG activity [19], while the GPi is appealing because it serves as the main output connector of the BG to the thalamus.

Although stimulation of both targets, STN and GPi, has been shown to provide therapeutic benefits in human patients [20–26], there remains a deficient mechanistic comprehension of DBS. For treatment of human patients, targeting the STN is considered preferential by some [27], though recent studies have indicated that the difference in effectiveness between the two targets is equivocal [20–23]. However, there

is some indication that there are more cognitive side effects of STN-DBS due to its relationship with the limbic system [24, 25] and that GPi-DBS may have more benefits in this regard [23]. In human studies, impulsivity and depression are associated with both targets [21, 25, 28], and anger has been specifically linked to STN-DBS [21]. In general the side effects associated with GPi-DBS are not as well characterized as those for STN-DBS [25].

Consequently, optimizing stimulation patterns for DBS in order to maximize therapeutic benefits is challenging. The 6-hydroxydopamine (6-OHDA) rodent model has frequently been used to study PD and DBS [3–12, 29]. Typically a unilateral injection of 6-OHDA is administered in the brain of a naive rat to induce one hemisphere to be Parkinsonian, thus creating a hemi-Parkinsonian model. The hemi-Parkinsonian rodent model is advantageous for behavioral studies because it is more feasible to study larger populations, which are required to meaningfully interpret statistical findings of behavioral data. Thus, the rodent model is an appropriate vehicle for investigating motor improvement associated with GPi-DBS, and impulsivity and depression as potential side effects. The 6-hydroxydopamine (6-OHDA) rodent model has frequently been used to study PD and DBS [3–12, 29], but this work has focused almost exclusively on STN-DBS and no previous work has developed the relationship between behavior and stimulation frequency for GPi-DBS.

Aside from examining how the two targets differ in their efficacy for DBS, the optimal way to stimulate these structures remains an open question. Standard DBS consists of a train of regularly spaced bi-phasic current or voltage pulses. The rate of these pulses, the amplitude, and the pulse widths are the parameters that are tuned on a per-subject basis in order to find a stimulation signal that works well. This is done in an ad-hoc fashion, although in many animal and human DBS studies it has been verified that high frequencies (> 90 Hz) are more effective than low frequencies for stimulation in both GPi and STN [10, 11, 25, 27, 30]. Although therapeutic benefit

is attained using this basic strategy of regularly spaced pulses, the neural activity is not restored to its non-pathological state. In fact, stimulated neurons become pulse-locked and create an increase in power in the frequency band around the pulse frequency [11]. Although this is effective because bad information can no longer be transmitted by these entrained neurons, this “informational lesion” may also be a limiting feature of the treatment since good information cannot be transmitted by the neurons either.

More complex signal designs have been considered. In [31] it was shown that the temporal pattern of stimulus pulses influences the potency of the treatment. Previous work has found that stimulation signal with pulse times drawn from a gamma distribution and instantaneous pulse frequencies drawn from a log-uniform distribution were not therapeutically effective [32, 33] and suggest that regularization of neural activity is the key to the therapeutic benefit. The work in [33] in particular showed that long pauses between stimulation pulses is the main culprit for the reduction of efficacy. Much of the signal design work takes advantages of animal and biological computational models, because they are useful tools for studying novel designs and allow for multiple layers of analysis.

A final thrust of DBS that is relevant to this thesis is the investigation of new materials for electrode design. Two considerations for electrode design are the charge density that is able to be achieved for particular electrical contact geometries and the immunoresponse induced by the foreign material in the brain tissue. This second consideration is of interest to myself. Standard electrodes are made with metals such as platinum or platinum-iridium, which are intrinsically limited in the maximum currents and charge density that can be delivered through capacitive or reversible faradaic mechanisms [34]. Minimization of the device footprint is of research interest because it may reduce the inflammatory foreign-body response and the mechanical damage caused by the relative micromotion with brain tissue, thus improving the overall bio-

compatibility of the implanted electrode [35]. Naturally, better biocompatibility is an additional factor that contributes to the long-term efficacy of DBS.

CHAPTER 3

Computational Modeling

The use of neuronal models is an important tool in the field of neuroscience. There are a variety of models, from abstract neural network models to biophysical models along the lines of conductance-based Hodgkin-Huxley cell models [36]. The latter are the type of cell models used in this work. The differential equations that govern the model provide a mathematical description of how the synaptic, ionic and other (e.g. injected) currents influence the voltage potential across the membrane of the cell over time, which is appropriate level of complexity necessary when modeling how an added current source (i.e. the stimulating electrode) influences the spiking behavior of the cells and extrapolating population-level activity. Also, by adjusting the cell model parameters the properties exhibited in a variety of phenotypic states can be replicated, such as healthy and Parkinsonian neural activity.

The biophysical models used consist of a set of ordinary differential equations, which characterize the voltage potential across the membrane of the neurons over time. Six cell types are models here, one type per nucleus in the basal ganglia and then two cell types to model activity in the motor cortex. Below the six models are described. Note that it is understood that current varies with time and a current x is denoted as I_x , which is shorthand for $I_x(t)$. The neuron models used are based on

previous work [37–39], though parameter adjustments have been made so that the spiking activity of the neurons in the full network match experimental data [11, 17, 40] and the construction of the full-scale model is novel. We also add noise to the models by incorporating noise currents, I_z , into the differential equations, where z is zero-mean Gaussian variable.

3.1 Cell Models

Single compartment models were used for cortical pyramidal (PY) cells, the excitatory cells in the motor cortex, and interneurons (IN), which are inhibitory cells. Every PY cell i was described by the following equation:

$$C_m \frac{\partial}{\partial t} V_i = -g_L(V_i - E_L) - \sum_j I_{j,i}^{int} - \sum_k I_{k,i}^{syn} - d_i I_{dbs} - I_z, \quad (3.1)$$

where V_i is the membrane potential of cell i and C_m is the specific capacity of the membrane. The first term on the right hand side represents a leak current, the second term is the sum of ionic currents, and the third term is due to synaptic inputs from pre-synaptic cells. The current I_{dbs} results from the DBS current source (i.e. the electrode) and I_z is the noise current, which accounts for variations in input that are not explicitly modeled. Although PY cells are not directly directed, Layer V cortical cells project to STN, which is the modeled target for stimulation. With the projection axons being excited, antidromic spiking is induced at the PY cells, which is why the current I_{dbs} attenuated by d_i is incorporated into the differential equation.

Since the current pulse from a DBS electrode changes the extracellular potential in the STN tissue close to the electrical contact, it's possible that depolarization of the descending axon of the pre-synaptic M1 cells occurs and an action potential is excited in the axon. Conduction of a spike along the axon towards the soma and away from the axon terminal is referred to as antidromic spiking, because it is conduction of

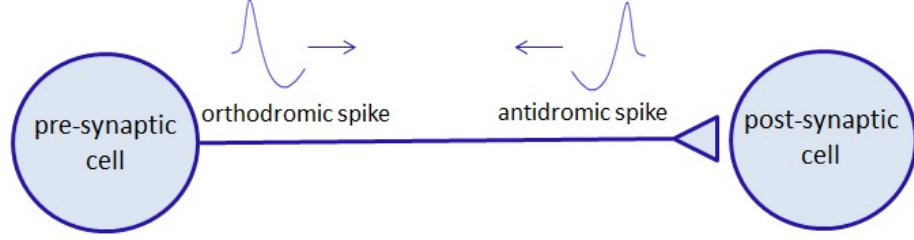


Figure 3.1: Cartoon depiction of antidromic versus orthodromic spikes. Spikes traveling in the normal direction of propagation are known as orthodromic spikes. They travel along the axon to the axon terminal that connects to the post-synaptic cell. Conversely, antidromic spikes travel in the opposite direction and may collide with the normal (orthodromic) spikes.

spikes in the direction opposite of normal travel. Normal spikes travel away from the soma along the axon towards the axon terminal and are called orthodromic spikes. This is depicted in the cartoon in Fig. 3.1. Antidromic spikes can be detected by verifying collisions with orthodromic spikes and by observing the appearance of action potentials at the soma with relatively low, fixed latency from the time of the stimulation pulse.

The equation for governing the IN cells is very similar and is given by

$$C_m \frac{\partial}{\partial t} V_i = -g_L(V_i - E_L) - \sum_j I_{j,i}^{int} - \sum_k I_{k,i}^{syn} - I_z. \quad (3.2)$$

The meaning for the terms on the right hand side is the same, although there is no direct DBS input to these cells. This is because interneurons are not directly stimulated nor do they project to the nucleus which is stimulated. However, PY cells do synapse onto IN cells and thus DBS induces indirect modulation of the firing activity of the IN cells.

Intrinsic current j due to ion flow across the membrane of cell i is denoted as $I_{j,i}$ and represented by the form

$$I_{j,i}^{int} = \bar{g}_j m_j^M h_j^N (V_i - E_j). \quad (3.3)$$

Parameter	Value
\bar{g}_L	0.1 mS/cm ²
E_L	-70 mV
\bar{g}_{Na}	50 mS/cm ²
\bar{g}_K	5 mS/cm ²
\bar{g}_M	0.07 mS/cm ²

Table 3.1: Parameters for PY cells.

Parameter	Value
\bar{g}_L	0.15 mS/cm ²
E_L	-70 mV
\bar{g}_{Na}	50 mS/cm ²
\bar{g}_K	5 mS/cm ²

Table 3.2: Parameters for IN cells.

The variable \bar{g}_j represents the maximal conduction for ion j , while m_j and h_j are the activation and inactivation variables, respectively. The realizations of these variables are governed by a two-state kinetic scheme as in [36, 39]. The reversal potential is E_j . The intrinsic parameters for these two cell types are shown in Tables 3.1 and 3.2.

The voltage equation for the membrane potential, V_{GPe} , is

$$\begin{aligned} C_m \frac{\partial}{\partial t} V_{GPe} = & -I_l - I_K - I_{Na} - I_T - I_{Ca} \\ & -I_{STN,GPe} - I_{GPe,GPe} + I_{str,GPe} + I_z. \end{aligned} \tag{3.4}$$

The same nomenclature for I_l , I_K , I_{Na} , and I_{Ca} as with the STN neurons is used. The GPe neurons have an additional ionic current which is a T-type calcium current, denoted as I_T . It is assumed that there is excitatory input from STN neurons and inhibitory input from other GPe neurons, represented by $I_{STN,GPe}$ and $I_{GPe,GPe}$, respectively. Additionally, the input to the GPe neurons from the striatum is modeled as a constant current, $I_{str,GPe}$. Cell parameters are given in Table 3.3.

The GPi neurons are very similar to the GPe neurons and have the membrane

Parameter	Value
\bar{g}_L	0.1 mS/cm ²
E_L	-55 mV
\bar{g}_{Na}	120 mS/cm ²
E_{Na}	55 mV
\bar{g}_K	30 mS/cm ²
E_K	-80 mV
\bar{g}_{Ca}	0.15 mS/cm ²
E_{Ca}	120 mV
\bar{g}_T	0.5 mS/cm ²
\bar{g}_{AHP}	30 mS/cm ²

Table 3.3: Parameters for GPe cells.

potential equation

$$C_m \frac{\partial}{\partial t} V_{GPe} = -I_l - I_K - I_{Na} - I_T - I_{Ca} - I_{STN,GPe} + I_{app} + I_z. \quad (3.5)$$

The same types of ionic currents are present as with the model GPi neurons. However, there is no assumed inhibitory inputs between individual neurons within the brain structure. It is also important to note that I_{app} , a constant current input, is applied in order to ensure that the intrinsic firing rate of the GPi neurons is higher than GPe neurons, in agreement with experimental data [17]. Cell parameters are given in Table 3.4.

The voltage equation for the membrane potential, V_{STN} , is

$$C_m \frac{\partial}{\partial t} V_{STN} = -I_l - I_K - I_{Na} - I_{Ca} - I_{GPe,STN} + I_{DBS} + I_z. \quad (3.6)$$

The leak current is denoted by I_l , while the potassium, sodium, and calcium ionic currents are denoted by I_K , I_{Na} , and I_{Ca} , respectively. Inhibitory synaptic current from afferent GPe neurons, $I_{GPe,STN}$, is also included in the model and is a weighted sum of the inputs from all presynaptic GPe neurons. Since the STN neurons are the

Parameter	Value
\bar{g}_L	0.1 mS/cm ²
E_L	-55 mV
\bar{g}_{Na}	120 mS/cm ²
E_{Na}	55 mV
\bar{g}_K	30 mS/cm ²
E_K	-80 mV
\bar{g}_{Ca}	0.15 mS/cm ²
E_{Ca}	120 mV
\bar{g}_T	0.5 mS/cm ²
\bar{g}_{AHP}	30 mS/cm ²
I_{app}	3 μ A

Table 3.4: Parameters for GPi cells.

Parameter	Value
\bar{g}_L	2.25 mS/cm ²
E_L	-60 mV
\bar{g}_{Na}	37.5 mS/cm ²
E_{Na}	55 mV
\bar{g}_K	45 mS/cm ²
E_K	-80 mV
\bar{g}_{Ca}	0.15 mS/cm ²
E_{Ca}	140 mV
\bar{g}_T	0.5 mS/cm ²
\bar{g}_{AHP}	9 mS/cm ²
I_{app}	-15 μ A height

Table 3.5: Parameters for STN cells.

target of the DBS, the stimulation current, I_{DBS} , is incorporated into the voltage equation above. Parameters for this cell type are given in Table 3.5.

The voltage equation for the membrane potential, V_{TC} , is

$$C_m \frac{\partial}{\partial t} V_{TC} = -I_l - I_K - I_{Na} - I_T - I_e - I_{GPi,TC} + I_z. \quad (3.7)$$

The current denoted I_e represents time-varying excitatory synaptic inputs from cells not explicitly included in the simulation. These cells also receive excitatory inputs

Parameter	Value
\bar{g}_L	0.05 mS/cm ²
E_L	-70 mV
\bar{g}_{Na}	3 mS/cm ²
E_{Na}	50 mV
\bar{g}_K	5 mS/cm ²
E_K	-90 mV
\bar{g}_T	5 mS/cm ²
E_T	0 mV
\bar{g}_e	0.05
E_e	0 mV

Table 3.6: Parameters for TC cells.

from GPi cells, as represented by $I_{GPi,TC}$. The parameters for the TC cells are given in Table 3.6.

3.2 Nuclei Models

Each structure in the BG is represented by 16 model neurons, totaling 64 model neurons for the entire network, plus for every STN cell there is an accompanying PY and IN cell in the modeled cortical layer. The links between these neurons, i.e. the synaptic connections, are randomly determined at the beginning of the simulation and the strength of these connections evolves over time according to the synaptic conductivity differential equations. We determine this random synaptic connectivity map by assuming that each cell i receives a fixed number n_x of inputs from a presynaptic cell type x . Thus n_x indices are selected by sampling uniformly without replacement from the index set of presynaptic cell type x . This is done independently for each cell i . For example, STN cell 1 may receive inputs from GPe cells 2 and 4, while STN cell 2 could simultaneously be connected to GPe cells 2 and 3 since the random assignments are done independently. We chose the numbers of links per cell type, n_x , to match empirical data and previous reports of approximate density of connections

(Presynaptic Cell Type, Postsynaptic Cell Type)	Number of Connections
(GPe, STN)	2
(STN, GPe)	3
(GPe, GPe)	2
(STN, GPi)	1
(GPi, TC)	2

Table 3.7: Parameters for randomly generate synaptic connections between cells.

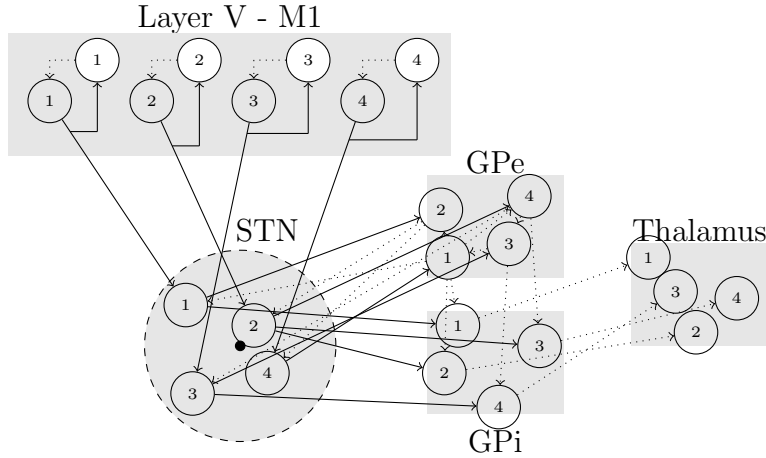


Figure 3.2: Cartoon showing synaptic connectivity for a small network with four model neurons per structure. Excitatory connections are depicted with solid lines and inhibitory connections are depicted with dotted lines. The dark circle in the middle of the STN neurons represents the DBS electrode. The white-colored cells in Layer V - M1 are the IN cells, where each IN cell forms a feedback loop with one of the PY cells.

between nuclei [37, 41]; this is presented in Table 3.7.

The connectivity assignments were selected to be made according to a uniform distribution because it provides maximal randomness in the model of connectivity, which is most appropriate when using a small number of model neurons to globally represent activity in a brain structure which in practice has many orders of magnitude more cells. Additionally, each PY cell projected to a unique STN neuron and IN cell, which has a feedback projection to the original PY cell. To illustrate the connectivity model assumed, a smaller example network is depicted in Fig. 3.2.

For the STN neurons, a notion of distance is also introduced into the model. It

has been shown that voltage potential change induced by a current pulse decays as a function of the distance between the neuron and the current source [42, 43]. Thus, we uniformly distributed the STN neurons inside a sphere of radius r , where the DBS electrode is defined to be located at the center of the sphere. Since the STN can be approximated as an ellipsoid with the smallest axis of length around 4 mm [44], we assume that $r = 4$ mm for the sphere.

The output of the computational model simulations are a set of voltage waveforms as a function of time, with one waveform per cell. Example activity is shown in Fig. 3.3. Notice that in the Parkinsonian state, the average firing rate is modulated and the firing pattern of all cells is more bursty. These voltage waveforms are then transformed into spike train data, where spikes are detected when the voltage exceeds a pre-determined threshold which is type-dependent. The spike train data is processed to analyze changes in the average firing rate and the distribution of the interspike intervals.

3.3 Regular and Irregular DBS

We incorporate DBS into the network model by including an additional current input to the STN neurons, which represents the current from the DBS electrode. The STN neurons are uniformly distributed inside a sphere so that each cell i is distance d_i mm away from the current source and the input to cell due to the DBS current, I_{stim} , is scaled by a function of this distance. The current at the STN neuron i is

$$I_{DBS} = I_{stim} \exp\{-(d_i/\sigma_d)^2\}, \quad (3.8)$$

where d_i is the Euclidean distance from the sphere center and σ_d is selected such that there is a large range in current amplitudes seen throughout the sphere. For the results presented in this work, $\sigma_d = 0.5$ mm.

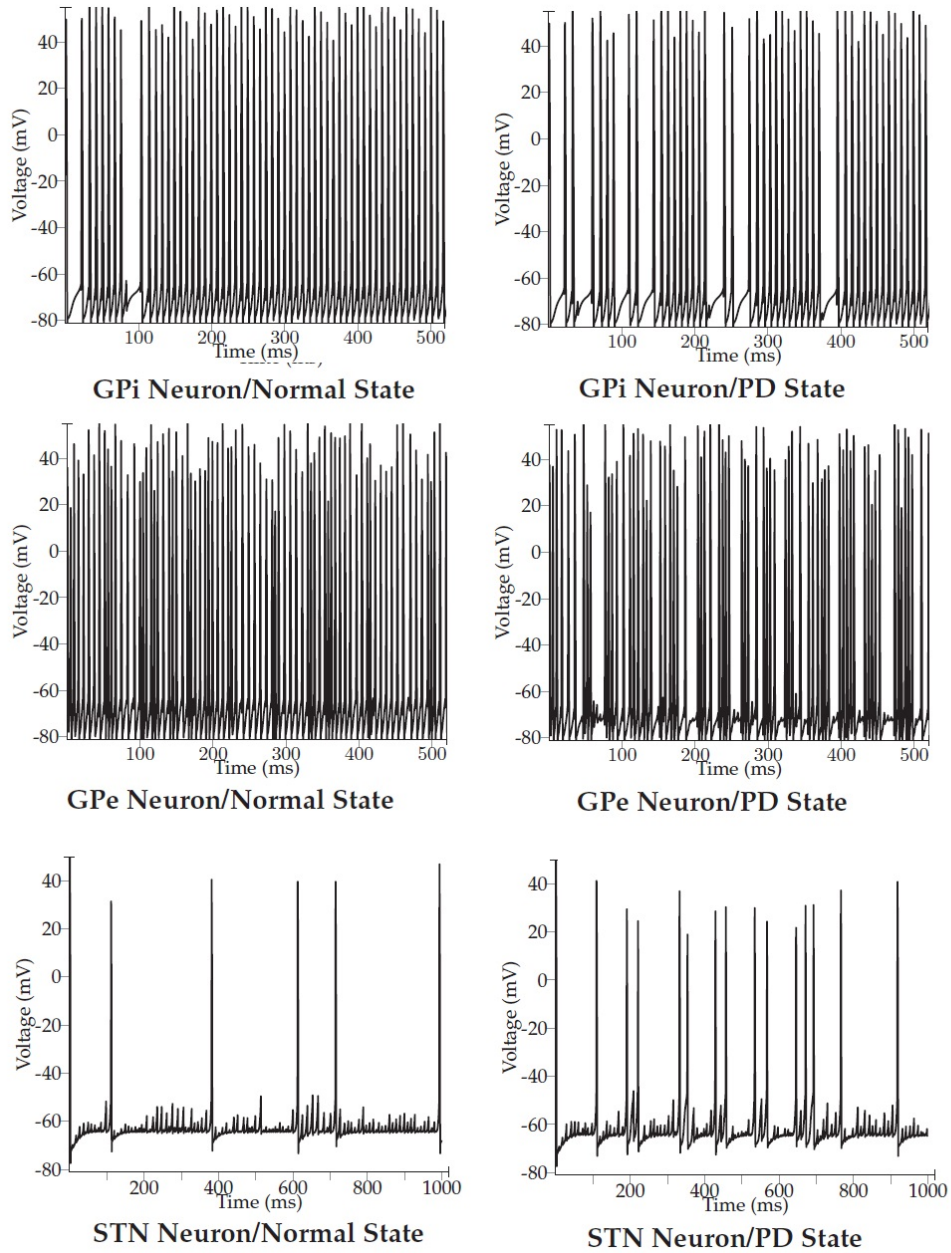


Figure 3.3: Example activity of GPi, GPe, and STN model cells. The left column depicts activity when the system model is in the normal (a.k.a. healthy) state and the right column depicts activity when the system model is in the Parkinsonian state.

In practice, DBS pulses are bi-phasic, so current alternates directions between electrical contacts on the electrode. This is done so that charge does not accumulate due to the capacitive nature of neural tissue. Here we model the electrode as a point source, so we assume that the DBS current signal, I_{stim} , consists of a pulse train with uni-phase pulses of width ω microseconds and amplitude α pA/ μm^2 . A single pulse, $p_\alpha(t)$, can be described as

$$p_\alpha(t) = \begin{cases} -\alpha & 0 \leq t \leq \omega \\ 0 & \text{otherwise} \end{cases}. \quad (3.9)$$

Assuming for simplicity of notation that stimulation begins at $t = -\infty$, we have

$$I_{stim}^{reg}(t) = \sum_{n=-\infty}^{\infty} p_\alpha\left(t - \frac{n}{f}\right), \quad (3.10)$$

where f is the stimulation frequency. The above signal has regularly spaced pulses at intervals of $1/f$. To create an irregular pattern of stimulation, noise is added to the timing of these pulses. In this case,

$$I_{stim}^{irr}(t) = \sum_{n=-\infty}^{\infty} p_\alpha\left(t - z_n - \frac{n}{f}\right), \quad (3.11)$$

where z_n are i.i.d. uniform random variables over the range $[-s, s]$ for some $s \in \mathbb{R}$ for all n . The average inter-pulse period between pulses is still $1/f$, but the period is no longer deterministic.

3.4 Mixture of Response

For a particular realization of synaptic connectivity and STN neuron topology, parkinsonian neural activity is simulated in response to (1) a regular, 150 Hz sequence of square current pulses and to (2) the same sequence of pulses with Gaussian jitter

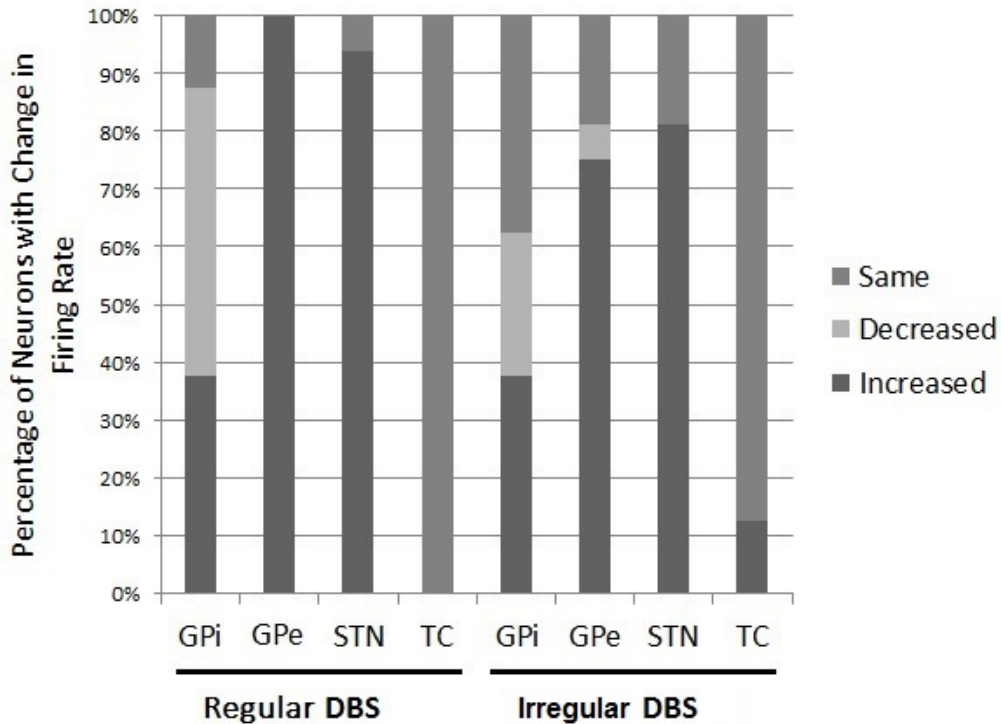


Figure 3.4: Distribution of changes in firing rates experienced by neurons while stimulation is administered, relative to the firing rates from the preceding time period without stimulation.

added to the timing of the current pulses to create an irregular stimulus pulse pattern. The random perturbations to the stimulus pulse times were uniform over $[-1, 1]$ ms. In each scenario, neural activity in response to stimulation is simulated for 10 seconds, with 10 second epochs without stimulation included preceding and following the stimulation period. The final 10 second interval was used to verify that the network activity returned to the Parkinsonian state after stimulation ended. The step size in the time domain was 0.01 ms, which was small enough to capture the dynamics of the system. The parameters $\omega = 60$ and $\alpha = 40$ were selected based on what values are used in practice and how consistently the resultant neural activity matched previous reports [37, 38, 41].

Changes in firing rate, with and without random perturbations, were characterized in order to determine how the stimulation influenced the average spiking activity of

	r (Pearson)	p	95 % C.I.
STN	0.921	1.21e-15	(0.783, 0.973)
GPi	0.995	6.35e-3	(0.986, 0.998)
GPe	-0.651	4.14e-7	(-0.867, -0.229)

Table 3.8: Correlations between change in C_v for regular and irregular DBS.

all of the neurons. Additionally, the coefficient of variation of the inter-spike intervals (ISI), defined as

$$C_v = \frac{\sigma}{\mu}, \quad (3.12)$$

was used as a measure of regularity. Spike trains with a low C_v are considered highly regular, or near periodic, while spike trains with high C_v are considered to be more irregular and have more variability in firing time.

Stimulus-locked firing was observed for a subset of STN and GPi neurons in response to both regular and irregular DBS, meaning these neurons had an average firing rate of 150 Hz computed over the 10 second interval. The lack of entrainment of GPe neurons is likely due to the inhibitory connections between GPe neurons. This matches neural activity that has been correlated with improvement in motor symptoms [11, 41]. For non-stimulus-locked neurons, changes in both firing rate and ISI C_v occurred. A mixture of responses was observed with stimulation: some neurons had increased firing rates, some had decreased firing rates, and some neurons remained unchanged. This mixture of responses is also consistent with previous computational and *in vivo* studies [11, 41, 45]. However, we find that there is greater variability in the distribution of firing rate changes induced by DBS with jitter. In Fig. 3.4, the percentage of neurons that display the three types of changes in firing rate is depicted for each brain structure simulated; the bars on the right half of the graph for the jittered case display a more diverse range of responses.

In comparing the change in the C_v in response to regular DBS and DBS with irregular pulse timing, there is an interesting correlation between the two for neural

activity in the GPe. While the changes in C_v for both STN neurons and GPi neurons are positively correlated, the change in C_v experienced by GPe neurons in the case of regular DBS is negatively correlated with the case of jitter DBS. Exact values are shown in Table 3.8. The neurons with a decreased C_v in response to regular DBS tended to have an increased C_v with irregular DBS.

3.5 Antidromic Spiking

Descending connections from the output layer of the cortex to the STN form the hyperdirect pathway. When administering DBS in the STN, the stimulation can activate both afferent and efferent axons [17, 46]. It has been shown that modulation of cortical activity may be important for therapeutic benefit [47, 48] and demonstrated that stimulating the STN in the rodent model evokes antidromic spikes in the motor cortex [40]. Antidromic spikes originate in the axon and propagate towards to cell body of the presynaptic cell. They are evoked by the stimulus pulse and appear at the presynaptic cell body, in this case the body of a projection neuron in M1, with a short fixed latency. Antidromic spikes may collide with orthodromic spikes, which are action potentials moving in the standard direction along the axon.

In [40], a frequency-dependent relationship for the fidelity and rate of antidromic spikes was found. The paper reports that with increasing stimulation frequency, there is a monotonic decrease in the fidelity of the pyramidal cell to the stimulus pulse. Thus, when stimulating at low rates (~ 10 Hz) in STN, there is a high probability that for a given stimulus pulse there will be a corresponding antidromic spike in Layer V of M1 after a short latency. However, when stimulating at high rates (~ 150 Hz), the probability of inducing an antidromic spike is lower.

In order to replicate this behavior in a model of M1, more than PY cells are necessary since alone they will have increasing firing rates with increasing rate of

inputs. In my model, I use an interneuron in a negative feedback loop with the PY cell. The PY cell synapses onto the STN cell that receives stimulation, as well as the IN. When stimulation is administered in the model, antidromic input appears at the PY cell body, as well as at the IN synapse of the axonal branch of the PY cell. Thus, as the rate of stimulation increases, the activity of both the IN and PY cells increase, with the IN cell increasing its inhibition of the PY cell activity.

Results from simulations similar to what was described in the previous section are shown in Figs. 3.5 and 3.6. For the four frequencies simulated, I was able to reproduce similar trends as reported for *in vivo* recordings [40] and those found in this body of work (see Fig. 5.4). The firing rate of IN cells increases monotonically with the stimulation frequency, which is expected since there are no inputs inhibiting the activity of these cells. However, the shape of the firing rate tuning curve for the PY cells is concave. This is because while the excitatory antidromic input to the PY cell increase with frequency, so does in the inhibitory synaptic input from an IN cell. The strength of the synaptic conductivity for the IN→PY synapse is the key parameter that is tuned to achieve the desired level of inhibition at the PY cell when stimulation is administered at different frequencies. The results are more robust to variations in the synaptic conductivity of the PY→IN synapses, the amplitude of the DBS current arriving at the PY soma, and the amplitude of the DBS current arriving at the IN synapse, though all of these variables must be considered jointly when adjusted to fit data.

Additionally we compute the entropy of the ISIs for the orthodromic spikes. The entropy describes how much uncertainty or randomness there is for the variable considered, namely the ISIs. If the firing is more regular, the entropy will be low, and if the firing is more bursty, the entropy will be higher. Entropy results are shown in Fig. 3.7 for both types of stimulus patterns considered at multiple frequencies. The general trend is the entropy of the orthodromic spike ISIs decreases with increasing

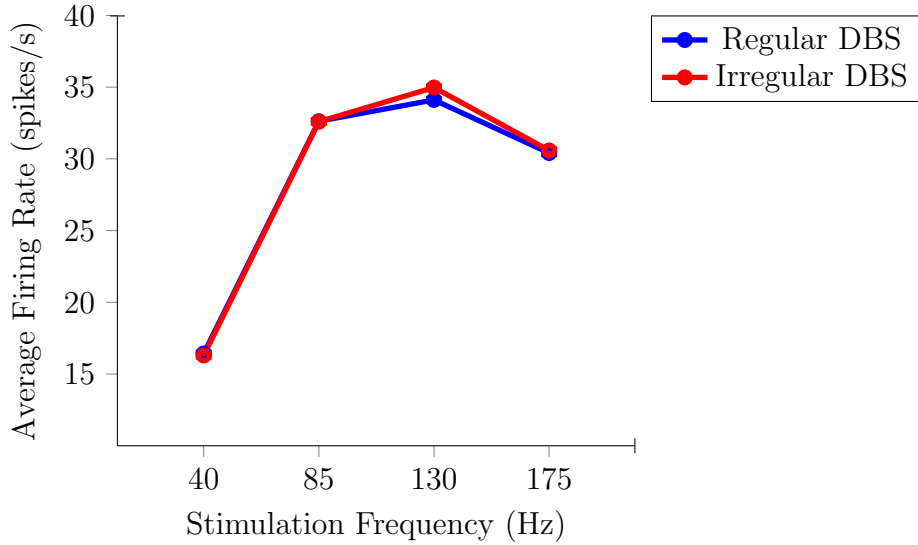


Figure 3.5: Average firing rate of the PY cells with regular DBS administered to the efferent STN cells at various frequencies. Values are the mean firing rate \pm S.D.

frequency, which corresponds to the burstiness of the firing being reduced. The irregular DBS decreases the entropy more than regular DBS. Since the average firing rate for the PY and IN cells is not significantly different for the two stimulus patterns, the main change induced by the irregular DBS is in the firing patterns of the PY cells.

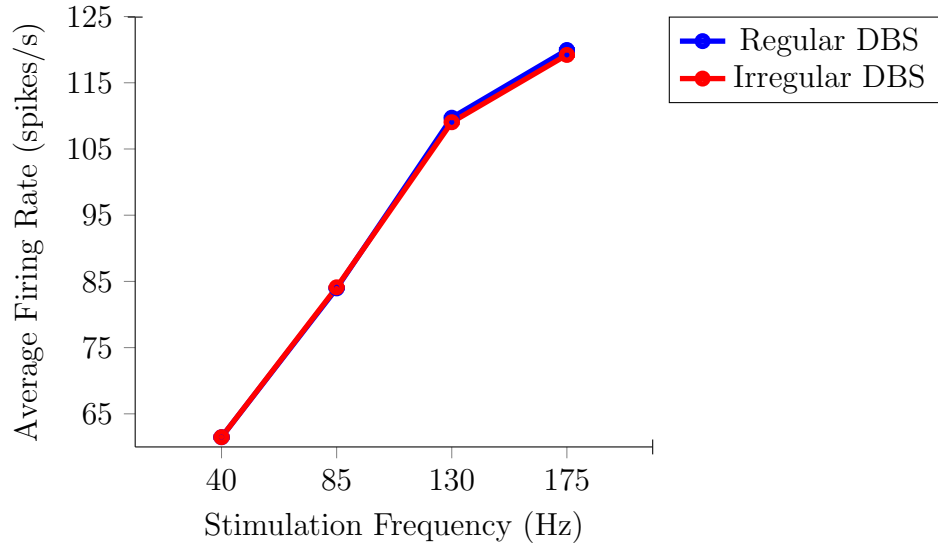


Figure 3.6: Average firing rate of the IN cells with regular DBS administered to the efferent STN cells at various frequencies. Values are the mean firing rate \pm S.D.

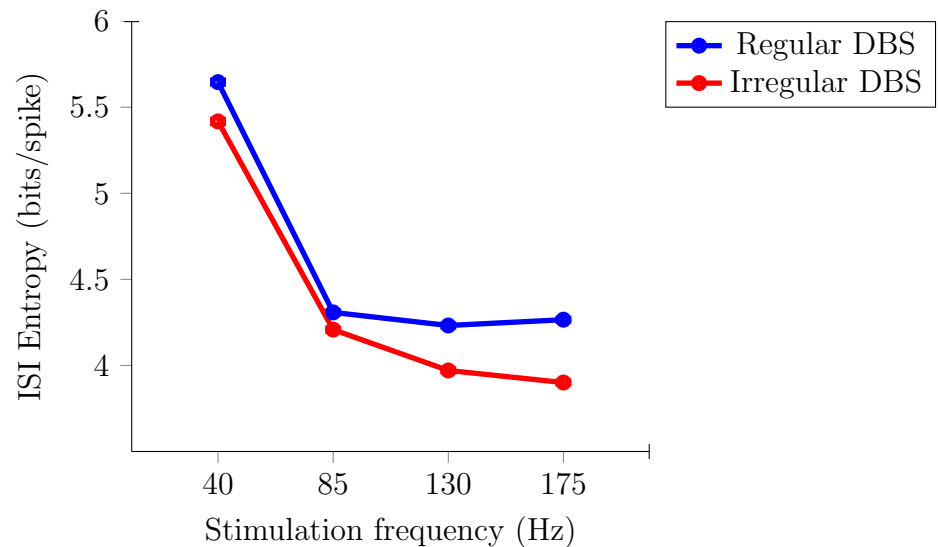


Figure 3.7: ISI entropy computed from the cortical computational model.

CHAPTER 4

Hemi-Parkinsonian Rodent Model

The 6-hydroxydopamine (6-OHDA) rodent model has frequently been used to study PD and DBS [3–12,29], but no prior work has developed the relationship between motor symptoms of PD in behaving rats and the effects of GPi-DBS. In order to address this, the work presented here provides a systematic characterization of behavior tuning in response to stimulation frequency and validation of the translational value of the 6-OHDA rodent model to study GPi-DBS. Animals were evaluated using a suite of behavioral paradigms to probe their motor ability, mood and impulsiveness. We assayed their performance in three different states: naive (intact), hemi-Parkinsonian, and with stimulation (i.e. hemi-Parkinsonian state with unilateral GPi-DBS). Thus, each subject served as its own control and eliminated the need for multiple cohorts. In many DBS studies, animal and human, it has been found that high frequencies (> 90 Hz) are more effective than low frequencies for stimulation in both GPi and STN [10,11,25,27,30]. In order to fully ascertain behavior tuning with stimulation frequency, we considered a range of frequencies spanning untherapeutic and therapeutic regimes.

Two populations of rats were used. The population ($n = 10$) was hemi-Parkinsonian and studied in a variety of motor tasks to understand how stimulation frequency tuned

motor behavior. A rotation task determined the asymmetrical limb use attributed to the unilateral 6-OHDA lesion and the reduced asymmetry under ten stimulation frequencies. This was further characterized in a cylinder task, where ipsilateral and contralateral forelimb wall touches were recorded for the same settings. The open field task was used to investigate the horizontal and vertical ambulation of the subjects in the hemi-Parkinsonian state and with five different stimulation frequencies. The second population of subjects ($n = 10$) was evaluated in motor and cognitive tasks in three possible states: naive (intact), hemi-Parkinsonian, and with GPi-DBS at a stimulation frequency verified to be therapeutic from the first population (130 Hz). This group was evaluated in a reaction time task to monitor the level of akinesia and bradykinesia in subjects, as well as to measure their level of impulsiveness. Additionally, anhedonia was measured via a sucrose preference task.

4.1 Animal Model

Male Long-Evans rats (Charles River Laboratories) weighing 400-550g were housed individually under a 12/12 hr light/dark cycle. To facilitate behavioral training, animals were given a food restricted diet such that they reached approximately 85% of their initial weight. Water was given *ad libitum*, except preceding the sucrose preference task. A bottle of evaporated milk sweetened with saccharin (Sweet-N-Low) was placed in the rats' cages 1-3 days before initial training in the reaction time task to prime the rats, as it was used as a liquid reward during the task. Additionally, they were given Reese's Pieces and peanuts as treats at the experimenter's discretion. All experiments were approved by the Institutional Animal Care and Use Committee of Rice University.

Following behavior training and/or behavior evaluation in the naive state, the rats received a unilateral injection of 6-OHDA in the right hemisphere and were implanted

with a stereotrode in the right entopeduncular nucleus (EP), the rat equivalent of the GPi. Prior to the procedure, buprenorphine (0.01-0.05 mg/kg) was administered subcutaneously (SQ) and desmethylimipramine (DMI, 10-20 mg/kg) was administered intraperitoneally (IP) to protect noradrenergic neurons from the neurotoxin. Rats were placed in a stereotactic apparatus (Kopf Instruments, California, USA) throughout the procedure. Under anesthesia (0.5-5% isoflurane in oxygen), 6-OHDA ($2 \mu\text{l}$ of $4 \mu\text{g}/\mu\text{l}$ in 0.9% saline; Sigma, Zwijndrecht, The Netherlands) was stereotactically injected into the medial forebrain bundle (MFB, coordinates from Bregma: AP -4, ML 1.2, DV -8.1). The injection needle was left in place for an additional 7-10 minutes following the injection to reduce the probability of the neurotoxin going up the needle track prior to absorption. In the same procedure, a platinum iridium or tungsten stereotrode ($R = 10 \text{ k}\Omega$; MicroProbes, Maryland, USA) was implanted in the EP (coordinates from Bregma: AP -2.5, ML 3, DV -7.9). Craniotomies were sealed with silicone elastomer (World Precision Instruments, Florida, USA), and the electrode connector was affixed in place with 6-12 stainless steel skull screws, as exposed skull surface space allowed, and dental acrylic. The electrode was fixed in place in such a manner that a plug connected to the electrode remained accessible for connection to the stimulator. The rats were given 2 days of post-operative care and all rats began the behavior tasks 2 weeks following the injection of 6-OHDA, which is sufficient time for a dopaminergic lesion to develop [49]. The loss of dopaminergic neurons is supported by the behavioral results of all subjects and posthumously through histological processing of the brains.

Following the experiments, the rats were anesthetized and the stimulating sites were marked by electrolytic lesions. The rats were given an overdose of Euthasol (0.5 – 1ml; Virbac AH Inc.) and then perfused intracardially with a 10% isotonic sucrose solution followed by 4% paraformaldehyde (PFA) in PBS. The brains were cryoprotected in a 30% sucrose solution in PFA (typically 4-5 days), then frozen

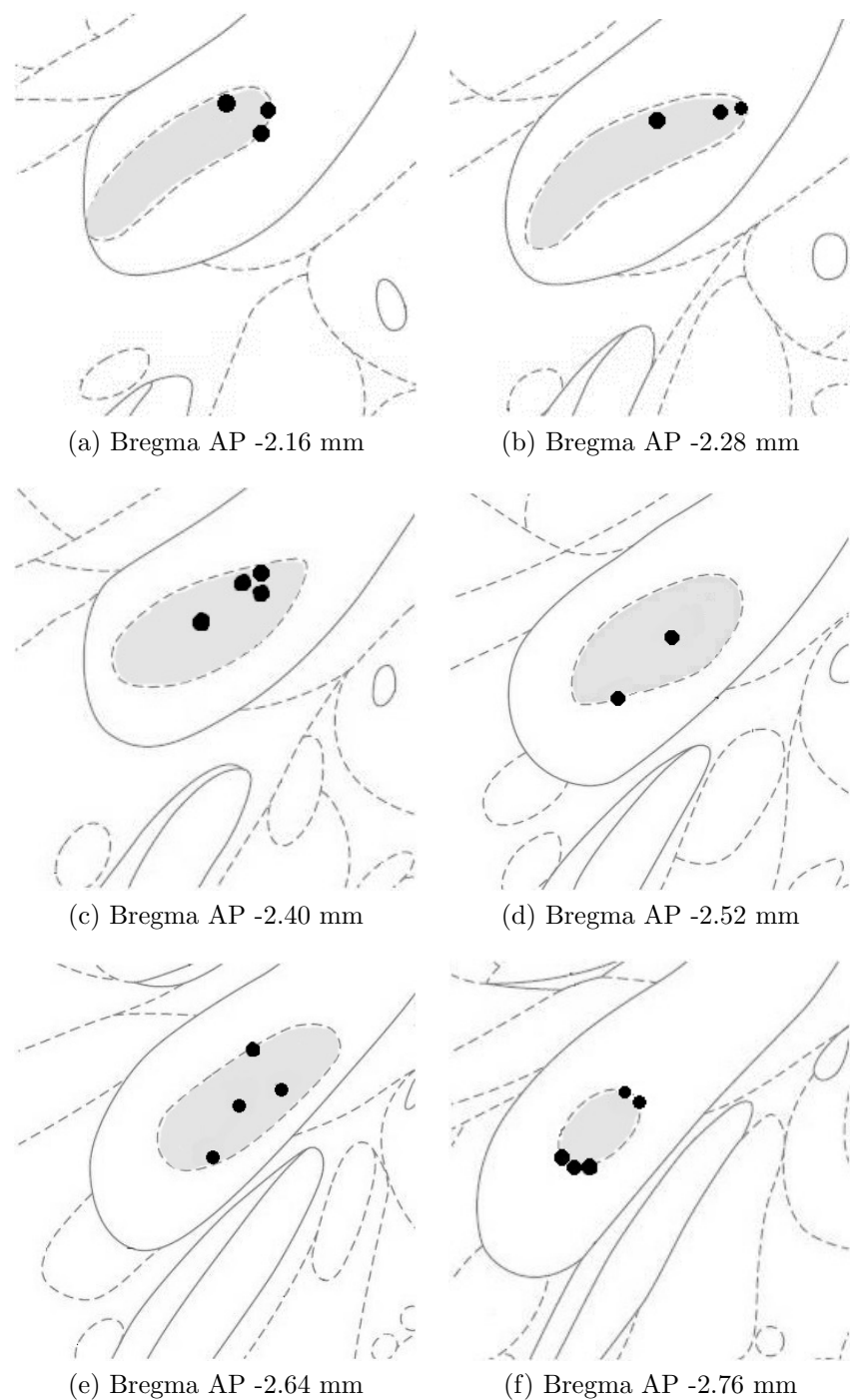


Figure 4.1: Approximate locations of the electrode positions for all subjects with one marker per subject and the EP (GPi) shaded in gray. Each image is a depiction of a coronal section that is 2-4 mm lateral and 7-9 mm ventral from Bregma, with solid and dashed lines demarcating neighboring nuclei. (a) Section is -2.16 mm posterior to Bregma. (b) Section is -2.28 mm posterior to Bregma. (c) Section is -2.4 mm posterior to Bregma. (d) Section is -2.52 mm posterior to Bregma. (e) Section is -2.64 mm posterior to Bregma. (f) Section is -2.76 mm posterior to Bregma.

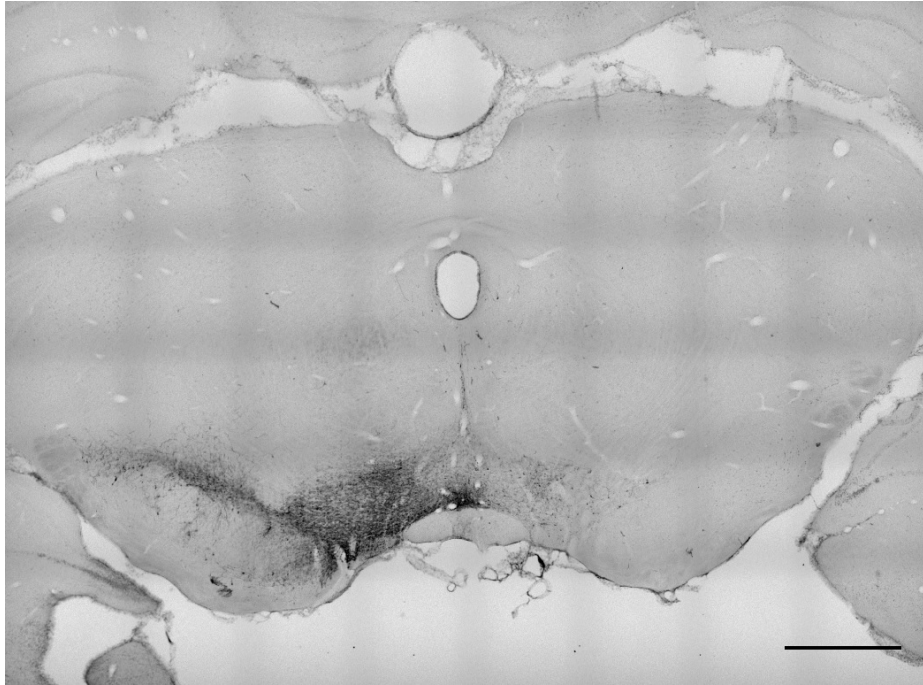


Figure 4.2: Representative image of THir cells in the SNc on the left lateral and right lateral sides of a 50 μm slice. Scale bar is 1 mm. TH positive cells appear darker than the surrounding tissue.

in Tissue-Tek OCT and stored at -80° Celsius. Frozen brains were sliced along the coronal plane and 50 μm sections were immunostained for tyrosine hydroxylase (TH; primary rabbit anti-TH antibody, 1:200 dilution; and biotinylated goat anti-rabbit secondary antibody, 1:400 dilution). A red fluorescent Nissl stain was used (Neurotrace, Invitrogen, 1:200 dilution) and slices were mounted using ProLong Gold Antifade Reagent with DAPI. The slices were imaged using a Nikon A1-rsi Confocal Microscope in order to determine electrode locations and lesion size. The electrode positions are depicted in Fig. 4.1, where the GPi is the shaded region in each figure and a black dot represents the tip location of a stereotrode for each subject. Also, the number of TH immunoreactive (THir) cells was quantified using Nikon Elements software (Nikon, Tokyo, Japan). Symptoms of PD are thought to become apparent after loss of a large fraction of dopaminergic cells. We quantified the extent of our unilateral 6-OHDA lesions both directly via histology and standard behavioral assays. Comparing the lesioned and unlesioned hemispheres, there was a significant 6-OHDA-

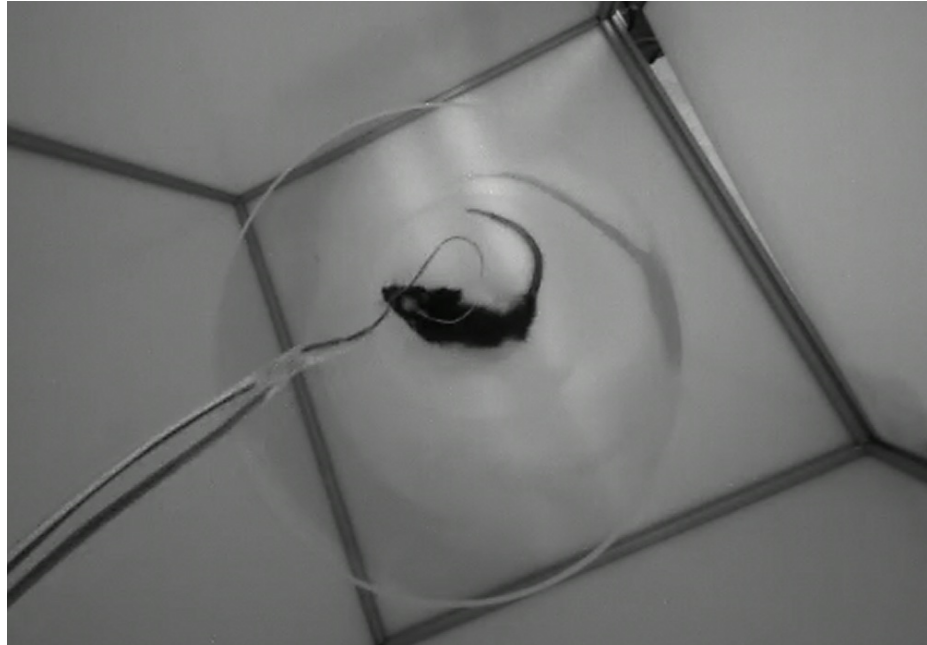


Figure 4.3: Photo of the cylindrical environment used in the rotation task. The cylinder was kept in an isolation chamber to limit distractions.. The cable from the stimulator was mounted on the the ceiling of the isolation chamber, so as not to impair the rats' movements.

induced depletion of $83.97 \pm 4.41\%$ (mean \pm SEM) THir cells in the SNC (results of one-way ANOVA: $F(1,40) = 56.24$, $p < 0.001$). A sample image in Fig. 4.2 demonstrates the considerable difference in THir cells in the left lateral and right lateral SNC.

4.2 Behavior Tests

4.2.1 Rotation Test

Methamphetamine induces rotation (circling behavior) in the direction ipsilateral to the SNC lesion and apomorphine induces rotation in the contralateral direction [11–13, 16, 30, 50, 51]. The rotation task was performed on the rats ($n = 10$) twice using each drug and the results were averaged. The number of rotations per minute is used as an indicator of extent of the lesion, i.e. the loss of dopamine function in



Figure 4.4: Cartoon describing a block of stimulation epochs for the rotation test. A two minute period of stimulation is represented with a numbered white box, which is bordered by black boxes represented the three minute control periods where no stimulation is administered. Eleven conditions are tested, which includes one test of baseline stimulation with no stimulation, and the order of the conditions is randomized per test.

6-OHDA lesioned rats [12,30,50,51], as this circling behavior is not present if striatal dopamine is not depleted. With effective DBS the number of rotations is attenuated. Methamphetamine dissolved in saline was administered IP (1.875 mg/kg) [11] under anesthesia (5% isoflurane in oxygen). Rats regained consciousness in 1-2 minutes and rested for an additional 15 minutes. This resting period allowed the methamphetamine to take effect in the rats. Rats were then placed in a cylindrical environment (diameter 30 cm, height 45 cm) made of clear acrylic and allowed to behave spontaneously. A photo of the experiment setup is featured in Fig. 4.3, showing an overhead view of a subject inside the cylinder. The task was performed similarly for apomorphine, except that apomorphine was dissolved in saline and administered SQ (0.1 mg/kg) [13,16,50].

The task consisted of eleven epochs. One epoch was allocated for assaying the rat in the hemi-Parkinsonian state (i.e., stimulation was off) and then ten epochs were allocated for the ten different stimulation frequencies ranging from 40 to 175 Hz. Each epoch was two minutes in duration and was followed by a control period that was 3 minutes in duration with stimulation off; this design is depicted in the Fig. 4.4. The order of the epochs was randomized within each block to reduce bias. The task was performed four times per animal for each drug, in line with other rodent studies [11,52].

Video data in 3D was captured using a Microsoft Kinect (Microsoft, Washington, USA) and was processed in Matlab to determine the angular movement of the rat over time. For each frame of the video, the morphology of the rat is detected and

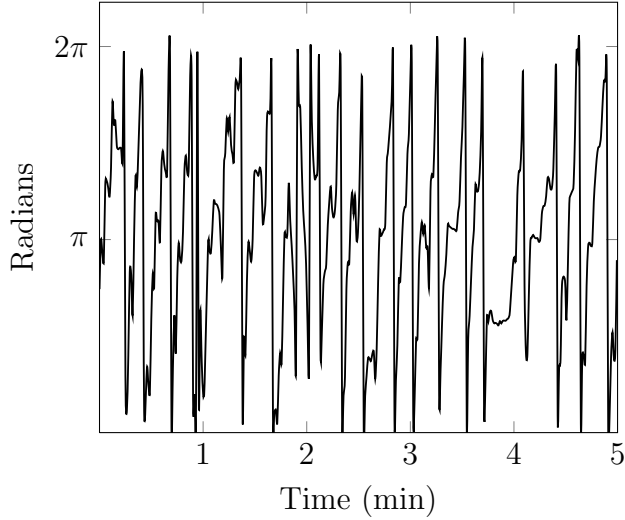


Figure 4.5: Example of rotation of rat over time.

the shape of it's body is fit with an ellipsoid using the Khachiyan algorithm [53]. The angle between the major axis of this ellipse and a pre-defined coordinate axis is tracked over time, as shown in Fig. 4.5. When the rat has rotated 2π radians (360 degrees), a complete rotation is counted and the instantaneous angle is reset to zero. These techniques enables us to calculate the angular velocity, total angular movement, and net number of unilateral rotations.

4.2.2 Cylinder Test

A cylinder task is traditionally used to measure the asymmetric forelimb use in the hemi-Parkinsonian rat, with the extent of the asymmetry indicating the extent of the unilateral lesion induced by the 6-OHDA injection [9, 51]. In this task, the rat was placed in a cylindrical environment (inner diameter 20 cm, height 46 cm) and permitted to behave spontaneously, as shown in Fig. 4.6. Typically rats rear on their hind limbs and lean against the wall of the environment using their forelimbs. A unilateral 6-OHDA lesioned rat uses the forelimb ipsilateral to the lesion with higher frequency than a normal rat, which uses each forelimb with close-to-equal probability.



Figure 4.6: Image of a subject rearing against the walls of an acrylic cylinder, as in the cylinder test.

Rats ($n = 10$) were allowed to rear freely 25 times and the proportion of paw presses with the limb ipsilateral to the 6-OHDA lesion was counted. This task was repeated while stimulation was administered for ten different stimulation frequencies, with at least 30 seconds between periods of stimulation.

4.2.3 Open Field Task

The open field task is used to evaluate ambulation, which is measured via horizontal and vertical activity (i.e. rearing) [54–57]. The open-field task was conducted on a square arena, 1 m \times 1 m, which was raised 1 m off the floor and marked into a grid dividing it into 25 equal-sized squares. The environment is shown in Fig. 4.7. Low lighting was used to illuminate the room and a camera was mounted on the ceiling above the arena. Video recordings were used to extract performance data. The number of squares traversed was recorded, which was calculated as the number of



Figure 4.7: Image of a subject in the open field environment.

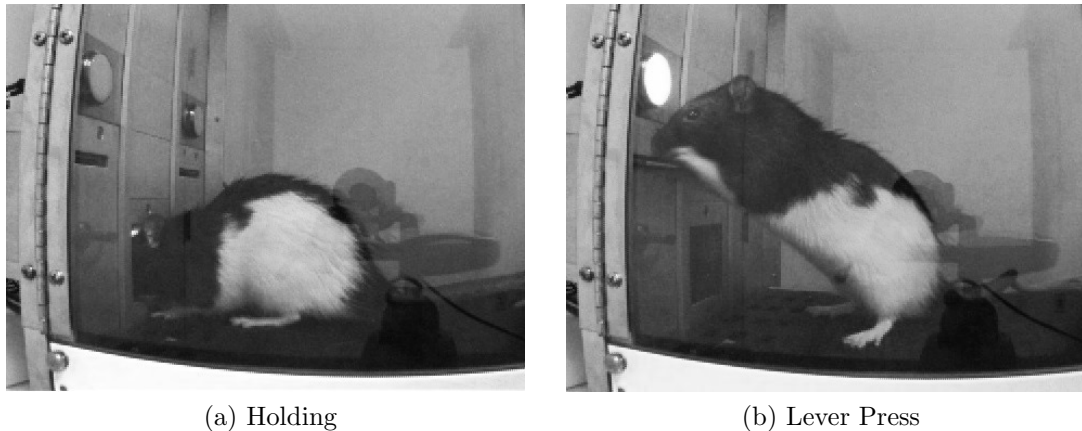


Figure 4.8: Depiction of the RT task. (a) The rat places its head above milk well for a random time interval, with an early head withdrawl termed a premature response. Time to correctly withdrawl head at end of interval is the reaction time. (b) Following correct head withdrawl a lever is extended and the time until lever depression is the motor time.

squares the rat occupied with at least three paws crossing the grid lines demarcating the square. Additionally, the number of rears, defined as the standing on its hind legs only, was counted. Each animal ($n = 10$) was evaluated at most once per day for 25 minutes. The task was repeated five times per animal, with a different frequency each time, and the order of the frequencies randomized for each animal. Between animals, the arena was cleaned using Sani-wipes.

4.2.4 Reaction Time Task

The reaction time (RT) task, which is similar to the task presented in [10], yielded measures of both motor and cognitive status. The task employs an operant conditioning box (Med Associates, inner dimensions: $30.5 \times 24.1 \times 21$ cm) equipped with two retractable levers flanking a liquid reward dispenser. A sensor at the dispenser detected when head insertions and withdrawals occurred. There were cue lights above each component, which indicated to the rat that an action be executed in relation to that component. The box was positioned inside an isolation chamber and time was recorded to a resolution of 10 ms.

The reaction time (RT) task was composed of four phases: a holding phase, lever-pressing phase, reward phase and time-out phase. Each trial began with the cue light above the liquid reward dispenser turning on, indicating the rat should insert and hold its head in place for a random period (chosen uniformly between 0.6 and 1.5 s in steps of 0.1 s). This is depicted in Fig. 4.8a. The hold period time reset any time the rat prematurely withdrew its head from the dispenser area, which is termed a premature response. Once the rat successfully completed this phase, the cue light above the liquid dispenser was extinguished, a random lever was extended (left and right lever extensions were equally likely) and the corresponding lever cue light was illuminated. The rat then withdrew its head and pressed the lever, as depicted in Fig. 4.8b. Following depression of the lever, the rat was given a milk reward with 50% probability in order to increase the likelihood of an overall larger number of completed trials [58]. An inter-trial time out phase lasted 10 seconds, allowing rats time to drink and potentially exit the dispenser area prior to the next trial.

We define three behavioral measures for this task: (1) RT, (2) motor time (MT), and (3) the proportion of premature responses (PPR). The RT was defined as the time between the lever extension and the withdrawal of the rat's head. This is a model of the rats' ability to initiate movement, which is impaired when in an akinetic state. Times longer than 1.5 seconds were disregarded as they are considered to be times not related to the task [29, 58]. The MT was measured as the time following the head withdrawal until the lever was pressed; times longer than 2 seconds were generally considered as not task-related (e.g. rat lost interest task) and thus were excluded from analysis [29, 58]. This measure relates to bradykinesia and how well the rats were able to execute a movement. Finally, the PPR was computed as the ratio of premature responses to total responses, i.e. premature responses plus correct responses,

$$\text{PPR} = \frac{\text{Number of premature responses}}{\text{Number of premature + correct responses}}. \quad (4.1)$$

This metric indicates the impulsiveness of the rat [10].

The rats were trained on this task until their performance was stable, which took 4-6 weeks. The performance was considered stable if the means RT and MT were within the mean \pm standard error of the mean (SEM) for the previous two days. Additionally, we required that the 5-day sliding average PPR was within the 5-day sliding mean \pm SEM from the previous two days. Once stability was achieved, the rats were evaluated in the behavior box once a day for three consecutive days, which defined their performance in the naive state. Following surgery, the rats were re-trained for three days to ensure that the behavior had not been unlearned during the post-op recovery period before they were assayed in the hemi-Parkinsonian state. The performance for the hemi-Parkinsonian state and the treated state with 130 Hz GPi-DBS was measured over non-overlapping three consecutive day periods, one task per day.

4.2.5 Sucrose Preference Test

Given a choice, rats prefer sucrose-sweetened water to plain water, but this preference decreases in an anhedonic state [59]. The animals were deprived of water for 8 hours to ensure that they were thirsty prior to the task. They were then allowed one hour to drink freely from two identical bottles filled with water and a 1% sucrose solution. This task took place in the same behavior box as the reaction time task, as shown in Fig. 4.9, but without the lever and milk dispenser components being active. Thus, the environment was familiar to the rats. The bottles were alternated between tests on the left and right side of the behavior box in order to minimize spatial preference. The sucrose preference index (SPI) was the metric associated with this task and is defined as

$$\text{SPI} = \frac{\text{grams of sucrose solution consumed}}{\text{grams of sucrose solution + water consumed}}. \quad (4.2)$$

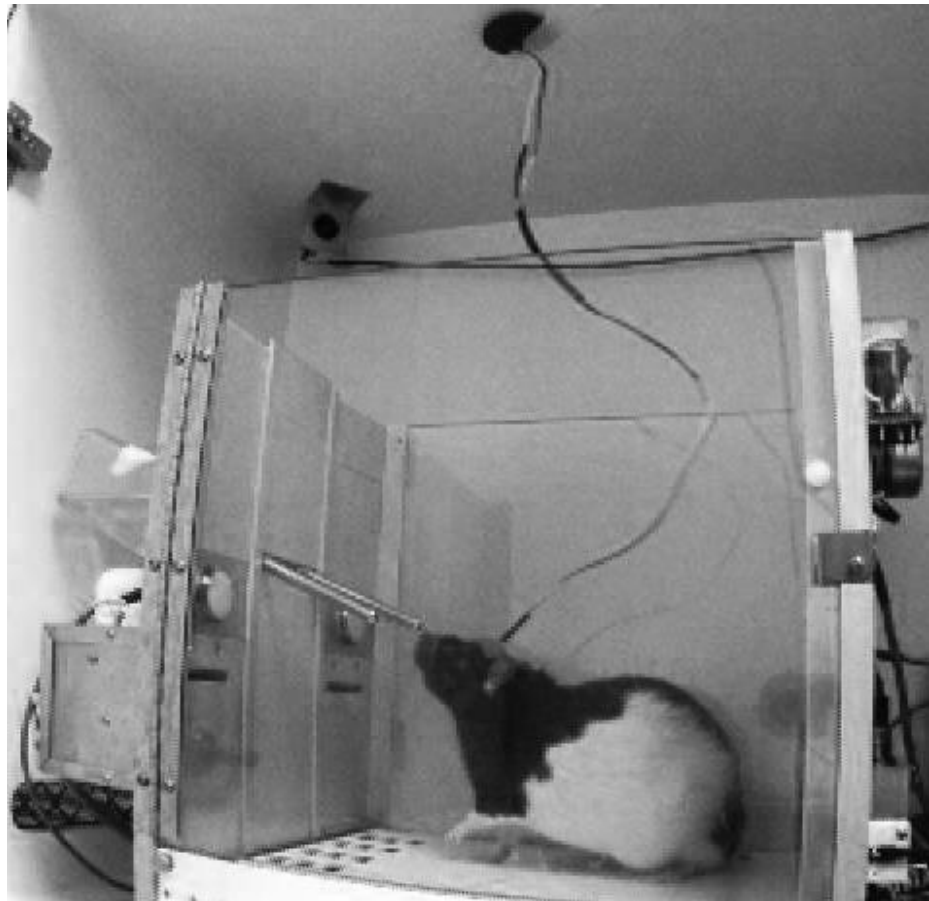


Figure 4.9: Image of a subject performing a sucrose preference test. Two identical bottles are presented to the subject and the volume of fluid consumed from each bottle is used to determine the anhedonic state.

This task was performed twice per state for each subject, with at least 24 hrs of water available *ad libitum* between tasks. The rats were assayed in the naive state, hemi-Parkinsonian state, and with 130 Hz GPi-DBS.

4.3 Behavioral Results

4.3.1 Motor Asymmetry

To evaluate the efficacy of GPi-DBS on motor asymmetry, we used methamphetamine and apomorphine to induce locomotory rotation. We surveyed performance for ten stimulation frequencies in addition to the hemi-Parkinsonian state without stimulation. Two minute epochs of stimulation were preceded and followed by three minute no-stimulation control periods. The rotation rates during the prior and post control periods were averaged and used to normalize the rotation rate of the stimulation epoch, i.e. the rotation rate with stimulation was divided by the average rotation rate from neighboring control periods so that the normalized rotation rate reflected the relative decrease in rotation when stimulation was administered. Results for the average normalized rotation rate for all conditions are shown in Fig. 4.10 for circling induced by methamphetamine (a) and by apomorphine (b). The general trend for both drugs was that the normalized rotation rate decreased with increasing stimulation frequency. Additionally, we characterized the total angular distance traveled by the rat, which is the total angular movement in both directions (as opposed to the net movement in one direction which gives the rotation rate). The total angular movement for a stimulation epoch is normalized by the values for the preceding and following control epochs, as before, and then average across the population. Results for the average normalized angular distance is shown in Fig. 4.10 for circling induced by methamphetamine (c) and by apomorphine (d)

For the methamphetamine rotation task, repeated measures ANOVA indicates

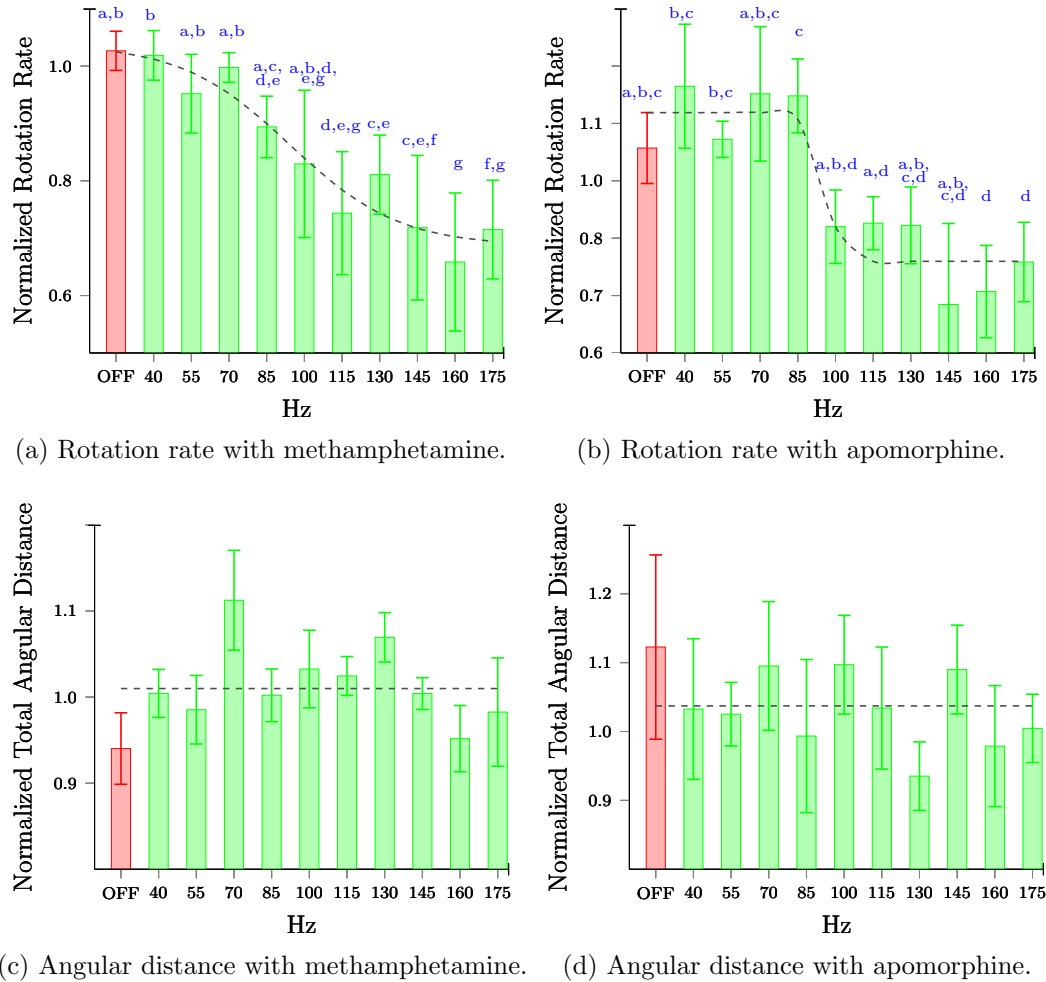


Figure 4.10: The normalized rotation rate and total angular distance traveled are presented above for the rotation task using methamphetamine and apomorphine. Different alphabetical characters indicate significant differences determined from post-hoc LSD tests ($p < 0.05$).

that there is a significant difference in the normalized rotation rate across the stimulation conditions ($F(10, 90) = 4.625, p < 0.001$). Post-hoc LSD tests indicate that a significant difference in the average normalized rotation rate from the off condition occurs for stimulation frequencies greater than 100 Hz, which is around where we hypothesize there is a therapeutic threshold. For frequencies of 115 Hz and larger, there is a significant reduction in the normalized rotation rate. In considering the total angular distance traveled (i.e. the rotational movement in both directions), we find that there is no significant change across the conditions ($F(10, 90) = 1.559$); thus, net movement in one direction was reduced but not the overall movement. We conclude that high-frequency GPi-DBS reduces the circling behavior induced by methamphetamine.

The same task was performed using apomorphine and again it was found that higher frequencies were more effective in reducing the normalized rotation rate of the subjects on average. There was a significant difference in average performance across the conditions ($F(10, 90) = 3.052, p < 0.01$) and no significant change in total angular distance traveled was found ($F(10, 90) = 0.46$), though post-hoc tests show that it not until 160 Hz that significant reduction in the rotation rate is achieved. We attribute this result to the short and intense time course of the drug. In general, the effects of the drug lasted between 25 - 50 minutes, which is less than half the time that the methamphetamine induced circling behavior. Additionally, rotation rates during peak epochs reached values greater than 50 rotations/minute. Stimulation during these epochs was ineffective. Other studies have found that for high dosages of methamphetamine, STN-DBS was ineffective in reducing rotation rates in hemi-Parkinsonian rats, even for the stimulation frequencies up to 250 Hz [11, 52]. We believe that our results may be confounded by these extremely high periods of rotation caused by the apomorphine.

To further understand how GPi-DBS may improve the motor asymmetry in the

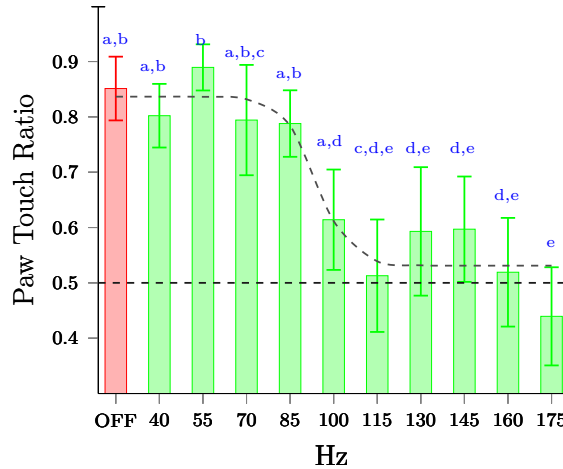


Figure 4.11: The ipsilateral to total paw touch ratio in the cylinder task. The number of times the rat reared against the side of the cylinder environment and made contact using each forelimb was recorded. The total number of times the rat used the paw ipsilateral to the 6-OHDA lesion was divided by the total number paw touches to create the paw touch ratio. Different alphabetical characters indicate significant differences determined from post-hoc LSD tests ($p < 0.05$).

hemi-Parkinsonian model as a function of the stimulation frequency, we performed a cylinder task on the rats ($n = 10$) for the same ten frequencies evaluated in the rotation task. We found that again motor asymmetry improves as stimulation frequency increases ($F(10, 90) = 4.455, p < 0.001$). The results are consistent with those found in the methamphetamine rotation task - frequencies above 100 Hz are effective in reducing the normalized rotation rate. For stimulation frequencies at 115 Hz and above, the average paw touch ratio is within errorbars of 0.5, which represents an equal number of touches by the contralateral and ipsilateral paws and indicates that the motor asymmetry is essentially eliminated with higher frequency GPi-DBS.

4.3.2 Ambulation

The open field task was used to evaluate exploration and ambulation by measuring the number of squares traversed and the number of rears. The horizontal exploration of the rats was quantified in terms of the interior squares that they traversed (the inner 4×4 square area) and the outer squares that they traversed (the 16 outer

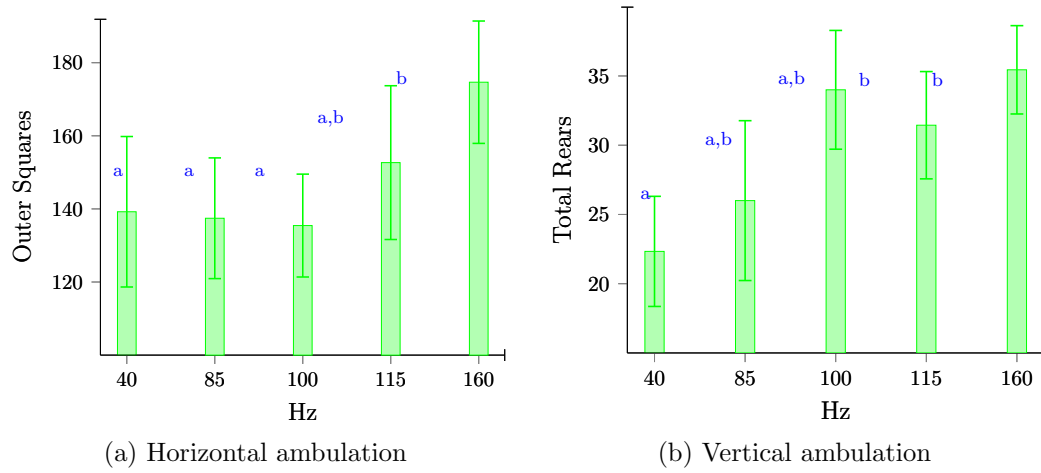


Figure 4.12: Total number of outer squares traversed and number of rears during open field task. Different alphabetical characters indicate significant differences determined from post-hoc LSD tests ($p < 0.05$).

squares that encompass the inner squares). The interior of the area is the most anxiogenic area, so normal animals spend more time in the corners and outer areas of the environment [56, 57]. Analyzing the animals across states, there were significant differences in the vectors of mean values of the dependent variables (repeated measures MANOVA; $F(12, 96) = 49.629, p < 0.001$).

There was no change in the average number of inner squares traversed for all of the conditions ($F(4, 32) = 0.88$), which indicates that the anxiogenic state of the subjects was unchanged with stimulation. However, the dopaminergic lesion and subsequent GPi-DBS impacted the average number of outer squares traversed. There was a significant difference in the mean number of outer squares traversed by the rats across all states (repeated measures ANOVA; $F(4, 32) = 2.938, p < 0.05$), as shown in Fig. 4.12a. Specifically, there was a significant increase in horizontal movement as the stimulation frequency increased, indicating that GPi-DBS improved horizontal ambulation in the subjects. The rearing rate, a measure of vertical ambulation, was also found to have a significant difference in the mean number of rears across conditions, as shown in Fig. 4.12b (repeated measures ANOVA; $F(4, 32) = 2.897, p <$

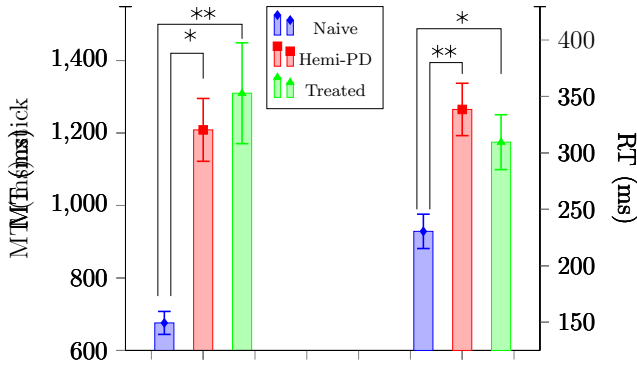


Figure 4.13: Measures of akinesia and bradykinesia. Bars represent mean \pm SEM. Mean MT and RT are shown on the left and right, respectively ($n = 10$). Significant differences were found between states. $*p < 0.05$ and $**p < 0.01$

0.05). For stimulation at 115 Hz and 160 Hz, there is a significant increased in the number of rears from the lowest stimulation frequency, 40 Hz.

4.3.3 Hypokinesia

There are two motor metrics associated with the RT task: reaction time, i.e. the time to initiate a head withdrawal, and motor time, i.e. the time to press the extended lever. Compared to their naive behavior, hemi-Parkinsonian rats ($n = 10$) showed increased mean RTs and MTs with and without DBS (see Fig. 4.13). The effects of DBS treatment on motor metrics was complex. With DBS, no rat achieved the same level of performance as in the naive state, though some rats experienced a reduction in mean RT and MT. To evaluate the significance of the results, repeated measures MANOVA was first used to evaluate the multivariate trends. This test indicated that there was a significant difference in the vectors of mean values of the dependent variables, RT, MT and PPR ($F(6, 30) = 5.068, p < 0.001$). Hence, we proceeded with univariate tests of significance.

There was a significant difference in the mean MT performance of the rats across the clinical states ($F(1.177, 9.417) = 16.351$ with Greenhouse-Geisser correction, $p < 0.005$) and subsequent post-hoc analysis was done to evaluate pairwise differences.

Under both LSD and Bonferroni tests, there was a significant increase in MT between the naive state and hemi-Parkinsonian state ($p < 0.005$), and no significant difference in mean MT between the hemi-Parkinsonian and treated states. For four out of ten rats there was an improvement in mean MT and two out of ten had no change in mean MT, but mean MT for the remaining four rats increased.

Similar trends were found in the analysis of RT data. Analyzing the group data, we found significant differences across states in the mean RTs (repeated measures ANOVA; $F(2, 16) = 11.885, p < 0.001$), that were significant pairwise (LSD and Bonferroni; naive and hemi-Parkinsonian state: $p < 0.02$, naive and treated state: $p < 0.05$). Three of the ten rats had lower mean RTs when receiving stimulation than when hemi-Parkinsonian, while seven of out ten rats had no change in mean RTs.

This lack of global improvement when DBS treatment was given is likely attributed to the fact that only a single current amplitude was used and there is high variation in terms what stimulation is effective across subjects [11, 21, 27, 49]. Since the parameters of the stimulation signal were fixed across the population of rats ($65\mu\text{A}$ current amplitude and 130 Hz stimulation frequency), it is not surprising that an overall therapeutic benefit of GPi-DBS was not found with respect to these two variables. The benefits of DBS are strongly tied to the stimulation amplitude and frequency, and generally must be tuned in order to maximize efficacy of the treatment [10, 11, 52, 60]. This is true not only in computational and experimental studies in animals, but in human studies as well [21, 22]. Although global motor improvement was not found, the quantified behavior is interesting in relation to the other variables examined throughout the experiment.

4.3.4 Cognition and Mood

Consistent with previous reports [10], we found hemi-Parkinsonian rats displayed increased impulsivity, as measured by premature responding (PPR), defined in (4.1).

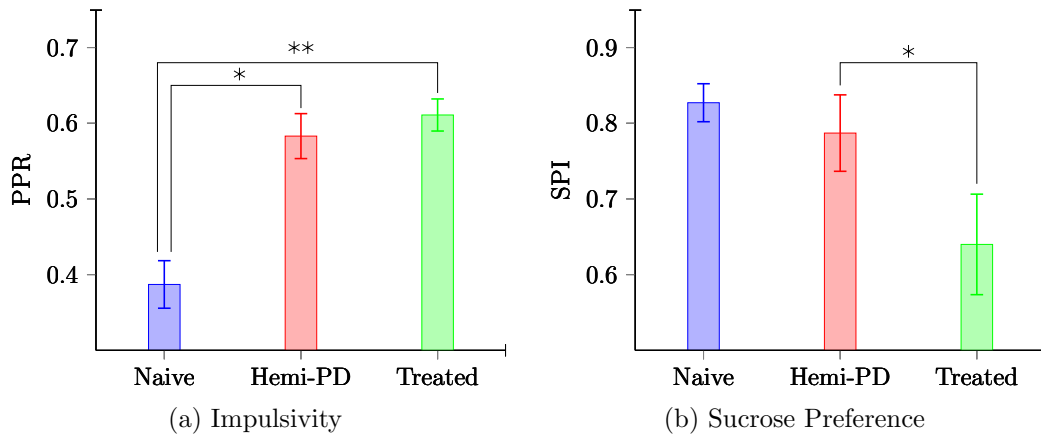


Figure 4.14: Measures of cognition. Data is shown as mean \pm SEM. (a) Mean PPR in the RT task ($n = 10$). The mean PPR across the states were determined to be significantly different. $*p < 0.05$ and $**p < 0.01$. (b) Mean SPI ($N = 10$). The mean SPI across the states was not equal. $*p < 0.05$.

Results are given in Fig. 4.14a, which shows an increasing trend in PPR. A significant difference in mean PPR was found (repeated measures ANOVA; $F(2, 16) = 20.387, p < 0.001$) and post-hoc analysis showed that the rats were significantly more impulsive in both the hemi-Parkinsonian and treated states relative to the naive state (LSD and Bonferroni; $p < 0.05$ and $p < 0.01$, respectively). The increased impulsivity between the treated and hemi-Parkinsonian state was not significant (LSD: $p = 0.114$). However, nine of ten rats were most impulsive while receiving electrical stimulation.

In addition to impulsivity, we evaluated the rats for symptoms of depression. We found a significant change in the rats preference for sucrose (SPI, Fig. 4.14b) defined in (4.2), across the three experimental states (repeated measures ANOVA; $F(2, 18) = 6.992, p < 0.01$). Pairwise comparisons showed that there was not a significant decrease in the mean SPI from the naive state to the hemi-Parkinsonian state. However, there was a significant decrease from the hemi-Parkinsonian state to the treated state (LSD and Bonferroni; $p < 0.05$). Thus, 130 Hz GPi-DBS increased anhedonia in the subjects.

4.4 Correlations Between Tasks

It has been shown that when behavior is averaged over a moderately large cohort of animals, higher frequency GPi-DBS decreases hemi-Parkinsonian symptoms, such as pathological rotation and a lack of ambulation and rearing in an open field. However, it is unclear whether the variation in measured responses at higher frequencies or across different behavioral tasks simply reflects temporal randomness in DBS efficacy or actual graded differences in the responses of individual animals to GPi-DBS. Thus, I examined the correlation across subjects of responses at different frequencies within and across behavioral tasks. All *p*-values indicated here are from t-tests of significance.

I first examined the responses of different subjects in the open field to GPi-DBS. For frequencies of 85 Hz and higher, I found that an increased ambulation metric at one frequency was strongly correlated with increased ambulation metrics at other frequencies. For example, the amount of rearing observed with 85 Hz GPi-DBS is strongly positively correlated with the number of outer squares traversed during stimulation at frequencies of 85 Hz and above (all pairwise combinations: $r^2 > 0.5$; $p < 0.05$). Thus, at frequencies of 85 Hz and higher, benefits were consistent across behavioral measures.

I found similar results when examining methamphetamine-induced rotation. Normalized rotation rate under GPi-DBS for frequencies above 100 Hz were strongly correlated ($r^2 > 0.5$; $p < 0.01$). Thus, rats that have reduced rotation at one high frequency tended to also experience reduced rotation at other high frequencies. The same strong correlations were not as broadly observed for the rotation task with apomorphine, which is likely due to the highly variable rotation rate induced by the drug as previously discussed. However, the normalized rotation rates under apomorphine and methamphetamine were positively correlated for frequencies above 100 Hz ($r^2 > 0.4$; $p < 0.01$). Open field behavior presumably reflects slightly different, internally-generated mechanisms than pharmacologically-induced rotation. However,

I found that the number of outer squares traversed in the open field was negatively correlated with the rotation rate of the rats under both apomorphine and methamphetamine for the highest frequency tested in the open field test, 160 Hz, suggesting therapeutic benefit in open field behavior was correlated with benefit under pharmacological rotation.

The open field and rotation tasks were studied in a different cohort of rats than the RT, sucrose preference, and open field tasks. I found similar correlated responses in these second subjects. With 130 Hz GPi-DBS, the motor times were positively correlated with reaction times ($p < 0.001$), so rats with lower levels of bradykinesia also tended to experience lower levels of akinesia. Regardless of DBS, increased impulsivity predicts anhedonia and a decrease in locomotion: PPR was negatively correlated with SPI ($p < 0.05$), number of squares ($p < 0.02$), and number of rears ($p < 0.05$).

4.5 Conclusions for GPi-DBS

The work here demonstrates that there is a therapeutic threshold for the stimulation frequency above which GPi-DBS is effective in improving motor performance of the subjects and second that individual subjects display graded levels of response to DBS that is consistent across different behavioral measures. This graded response to DBS is consistent with what is observed in human studies, where stimulation parameters are tuned and adjusted over time to increase efficacy [61–63].

Multiple variables were considered in this novel study of GPi-DBS in the hemi-Parkinsonian rat. We found that stimulation significantly improved motor asymmetry and vertical motor activity relative to the hemi-Parkinsonian behavior, particularly when stimulation at higher frequencies (> 100 Hz) was administered. Post-hoc statistical data analysis demonstrated that significant improvements in performance

occurred for GPi-DBS beginning at around 100 Hz, which indicates that there is a therapeutic threshold of stimulation, below which stimulation tends to ineffective and above which it tends to effective. The strong correlations found for the frequencies within 15 Hz of this value additionally support this notion.

The sucrose preference task showed a significant increase in anhedonic behavior between the hemi-Parkinsonian state and with 130 Hz stimulation, which matches results of human studies where depression is found to be a side effect of DBS treatment. I conclude that GPi-DBS is effective in treating the motor symptoms in the PD rodent model and the results agree with human studies. Previously, several studies of STN-DBS have been performed in the rodent model, but results on GPi-DBS were lacking. The data presented here serves as a foundation for future animal studies and models of GPi-DBS.

CHAPTER 5

Cortical Recording with DBS

To appreciate the effects of DBS, it is critical to go beyond the observable behavior to examine the induced neurological changes. Previous work on the Parkinsonian rat model has demonstrated the impact of regular DBS on firing properties of BG nuclei [11] and the motor cortex [40]. The changes in the primary motor cortex (M1) are of particular interest because they are caused by antidromic spike propagation from STN to layer V of M1 via the hyperdirect pathway. The striatum serves as the main input nucleus to basal ganglia structures, but the hyperdirect pathway bypasses the striatum and directly connects M1 to STN [64]. This pathway is made up of excitatory projection neurons (pyramidal cells) from Layer V that synapse onto STN neurons. Recent work has indicated that changes in M1 activity constitute a significant part of Parkinsonian pathology and that DBS modulation of this activity may be crucial towards alleviating motor symptoms of PD [65].

The work presented in [40] was the first report of M1 activity in awake, freely moving hemi-Parkinsonian rats receiving DBS. We extend this work by considering STN-DBS in the hemi-Parkinsonian rodent model using both regular and irregular stimulation patterns. Neural activity is recorded while the rats behave spontaneously, with both single-unit and local field potential (LFP) activity being captured. Mul-

tiple stimulation frequencies are studied so that frequency-dependent effects can be observed. Below the experimental setup and results are explained.

5.1 Microdrive Design

Microdrives were designed with cannulae to direct recording electrodes bilaterally to M1 and a stimulating electrode to STN. Recording electrodes were fabricated using nichrome wire (NiCr). The wire was twisted together to create four-channel recording electrodes (a.k.a. tetrodes) and then electrically connected to a four-pin connector using conductive silver paint. The tips of the tetrodes were electroplated with gold (Au) to decrease the impedance of the exposed surface area. Electroplating was performed using Neurolynx software (**CHECK**) and a two-electrode configuration in phosphate buffered saline (PBS), with a large-surface area electrode made of either steel or carbon serving as the return electrode. That target plating impedance for the tetrodes was 300 k Ω at 1 kHz in PBS.

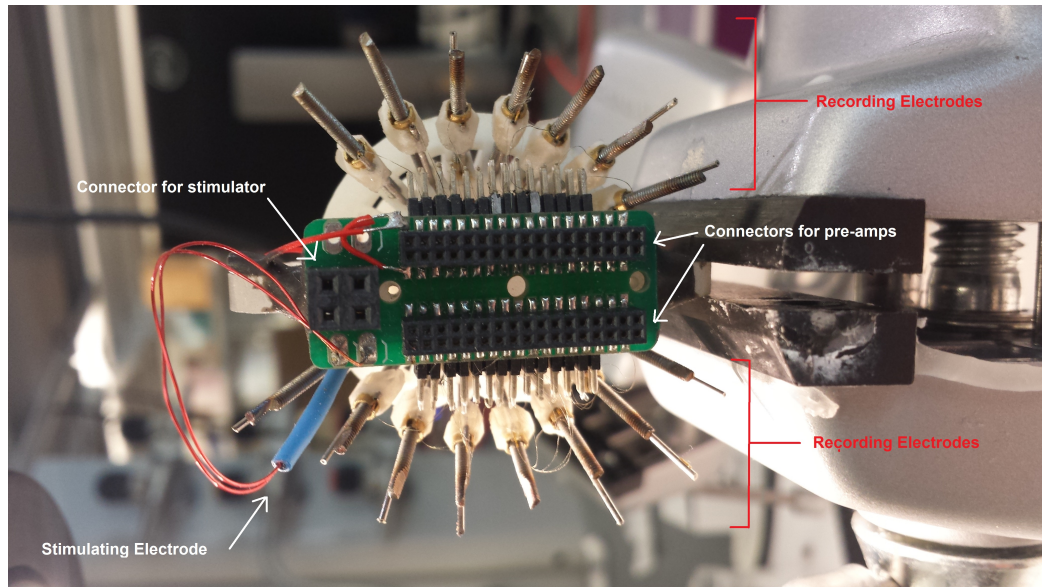
The microdrive was designed to have two cannulae positioned bilaterally at 1 mm anterior and \pm 2.2 mm medial/lateral from Bregma, which are coordinates coinciding with an area of M1 related to forelimb movement [66]. Each cannula holds seven tetrodes. Additionally, there was a cannula positioned at -3.6 mm posterior and 2.6 mm medial/lateral for the PtIr stimulating electrode (10 k Ω ; Microprobes). A PCB board with two rows of female connectors on the top and bottom was positioned on the top of the microdrive, with the male pins from the tetrode connectors fitting into the bottom side of the board. The female connectors on top are for the pre-amplifier circuit boards that are connected to the copper wire cables to plug into. A larger four-pin female to male connector was located at the back of the board and was electrically connected to contacts that the stimulating electrodes were soldered to. A picture of the top of a microdrive is shown in Fig. 5.1a and bottom is shown in Fig.

5.1b.

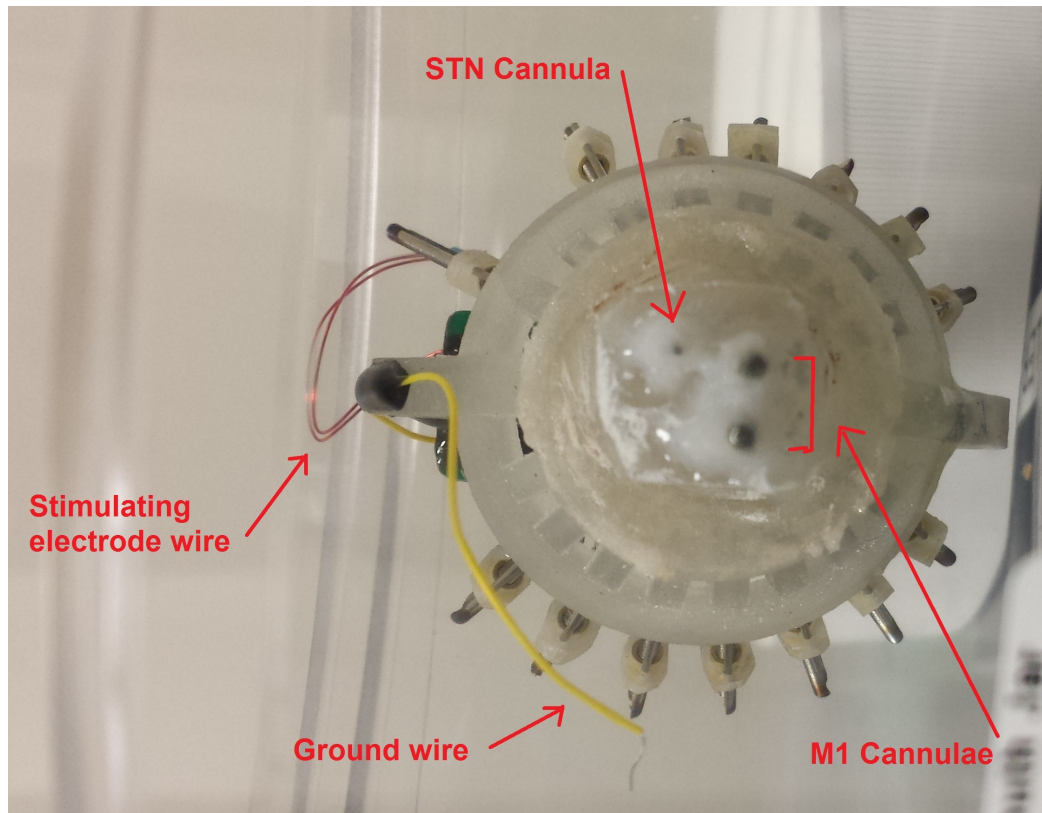
Dental acrylic held the cannulae fixed in place. Small shuttles made from a brass nut and dental acrylic served to move the electrodes along the axial dimension by turning the brass nut around a threaded rod. Each electrode was super-glued to a small tube guide, which itself was attached to the shuttle and thus when the shuttle moved up or down, the tetrode moved as well. This microdrive design allowed for post-operative movement of the recording and stimulating electrodes. For recording electrodes, this means that the position of the electrode could be adjusted over time in order to capture low-noise activity from many neurons.

5.2 Microdrive Implant and Placement of Electrodes

Male Long-Evans rats, 450 - 500 grams (g), were implanted with chronic microdrives for bilaterally recording in M1 ($n = 5$). Prior to the procedure, buprenorphine (0.01-0.05 mg/kg SQ) and DMI (10-20 mg/kg IP) is administered to protect noradrenergic neurons from the neurotoxin. Rats are placed in a stereotactic apparatus (Kopf Instruments, California, USA) throughout the procedure. Holes are drilled through the skull and bone anchor screws are placed (6 - 10) to help affix the microdrive to the skull. One screw with a wire soldered to it was placed in the most posterior portion of skull to serve as the ground screw. Craniotomies are made for the cannulae and the injection of 6-OHDA, which was stereotactically injected (2 μ l of 4 μ g/ μ l in 0.9% saline; Sigma, Zwijndrecht, The Netherlands) into the medial forebrain bundle (MFB, coordinates from Bregma: AP -4, ML 1.2, DV -8.1). Durotomies are performed at the craniotomy sites for the tetrode cannulae (from Bregma: AP 1, ML \pm 2.2). The microdrive cannulae are inserted through a small, sterilized piece of silicon sheeting and then the drive is positioned about the craniotomies. The sheet is trimmed to



(a) Top view



(b) Bottom view

Figure 5.1: Views of a microdrive designed for bilateral M1 recording and STN-DBS.

size and then glued to the skull. Finally, dental acrylic is used to cover the sheet and skull screws, adhering the microdrive to the rodent's head. The wire from the ground screw was soldered to a wire connected to a contact on the PCB which will have a connection with the ground pin of the pre-amp used for recording. While still anesthetized, the stimulating electrode is lowered to the target STN coordinates (from Bregma: AP - 3.6, ML 2.6, DB -7.8).

The rats were given 2 days of post-operative care and during this time the recording tetrodes were lowered into the brain tissue. Over a period of two weeks, while the dopaminergic lesion developed in SNc, the position of the recording electrodes was adjusted every 1 - 2 days. Net movement over an adjustment session ranged from 0 to 500 μm in the dorsal/ventral dimension. Positions of the recording tetrodes were localized in three ways: stereotactic coordinates, changes in firing properties, and the profile of sleep spindles in the LFP signal [67]. After this two week adjustment period, recording experiments, consisting of 1 - 5 recording sessions lasting up to 20 minutes in duration each, were implemented every 1 - 2 days over another two week period. During this time, tetrodes were adjusted between recording sessions for the purpose of capturing new cell activity, but they remained within the same cortical layer. The subjects were awake and freely moving during all recordings. Two environments were used for recordings: a sleep box, which was the environment where all tetrode adjusting took place, and the open field environment (described in Chapter 4).

5.3 Regular and Irregular Stimulation

The standard stimulation signal used in the PD rodent model consists of a sequence of brief bi-phasic constant-current square pulses delivered at a constant rate [9–12]. The amplitude of the stimulation was 100 μA and the pulse width was 60 μs . We chose to

perform the experiments using these stimulation parameters because they were found to be effective in previous work on STN-DBS of hemi-Parkinsonian rats [10,11]. Four different stimulation frequencies were tested: 40, 85, 130 and 175 Hz. This set of frequencies consists of a known untherapeutic frequency (40 Hz) and a known highly therapeutic frequency (175 Hz), as well as two frequency values in between. For regular DBS, a function generator (BK Precision; Yorba Linda, CA) is set to the desired stimulation frequency and outputs to a current stimulator (A&M Systems; Elkhart, IN) that outputs bi-phasic current pulses. The current stimulator connects to an output cable that plugs into a connector on the microdrive PCB. For irregular DBS, the function generator is connected to an Arduino Uno (Arduino; Ivrea, Italy), shown in Fig. 5.2. When an input pulse is detected, the Arduino waits a random period of time and then generates an output pulse. The random time period is uniformly selected from the interval 0 to 2 ms, with 2 μ s resolution. The output of the Arduino feeds into the current stimulator, so the stimulator is now triggered at irregular periods but with an average rate equal to the original stimulation frequency.

5.4 Data Capturing and Processing

NSpike software was used to acquire neural activity data in the freely moving rats. The LFP signal was recorded on either one or all channels of the tetrodes at a sampling rate of 30 kHz. The signals were referenced to one tetrode that served as a designated reference electrode. This electrode was referenced to the ground screw, which is connected to the ground pin of the pre-amp. The reference electrode was selected based on a low baseline level of activity, which enabled a higher SNR signal to be acquired from the other electrodes. Additionally, threshold-crossing event waveforms from all channels were saved when activity on one channel exceeded a tetrode-specific threshold, which was set between 35 and 60 μ A (depending on the quality of the

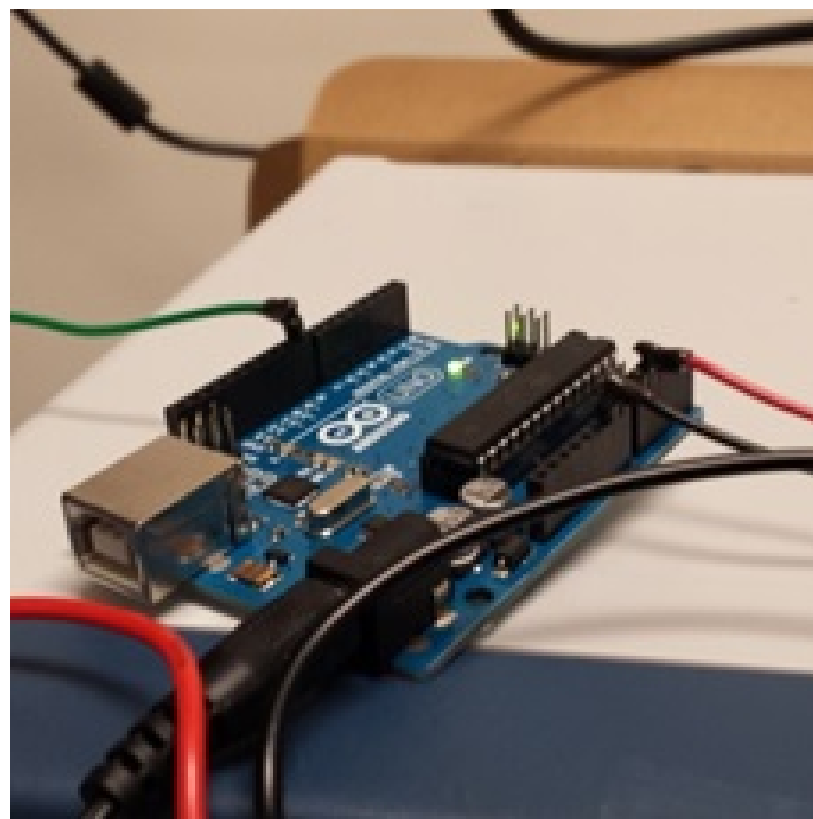


Figure 5.2: Arduino Uno used to generate irregular DBS pulse patterns.

signal). These waveforms are forty samples with a sampling rate of 10 kHz and were digitally filtered between 300 Hz and 6 kHz.

All data was processed off-line in Matlab. The LFP data was initially divided into 60-second windows for ease of processing and filtering. If stimulation was administered during the recording period, the stimulation artifact was removed from the LFP signal by blanking a 1.5 ms period, starting at the CPU timestamp for the beginning of the stimulation signal. The samples that were blanked are then replaced by values generated from linear interpolation from the data points at the two ends of the blanking period. The entire window is then downsampled to a rate of 1 kHz and then low-pass filtered using a finite impulse response (FIR) least-squares lowpass filter with a cutoff frequency of 200 Hz. Individual units were identified from the threshold-crossing events by clustering spikes using peak amplitude and spike width. All analysis of LFP and single-unit data was performed using custom Matlab code or the Chronux toolbox [68, 69].

5.5 Spike Results

Well-isolated single-units are identified as described in the previous section and example spike waveforms are shown in Fig. 5.3. After spike data is processed, several descriptive metrics of the spiking activity can be quantified. The two main metrics emphasized in this work are the average firing rate and the entropy of the interspike intervals (ISI). Together these values describe the general level of activity of a neuron and how regularized this activity is.

Previously work describes the frequency-dependent relationship that the firing rate of projection neurons in the cortex have with the DBS signal. In Fig. 5.4, results are shown for the average rate in the Parkinsonian state (i.e. stimulation frequency is 0 Hz) and for multiple stimulation frequencies. As can be seen from the

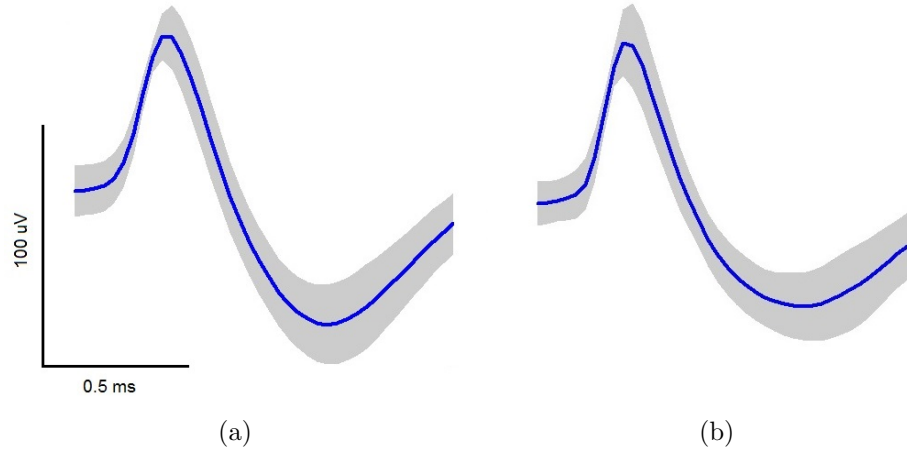


Figure 5.3: Example average spike waveforms acquired from well-isolated single neurons during *in vivo* recording.

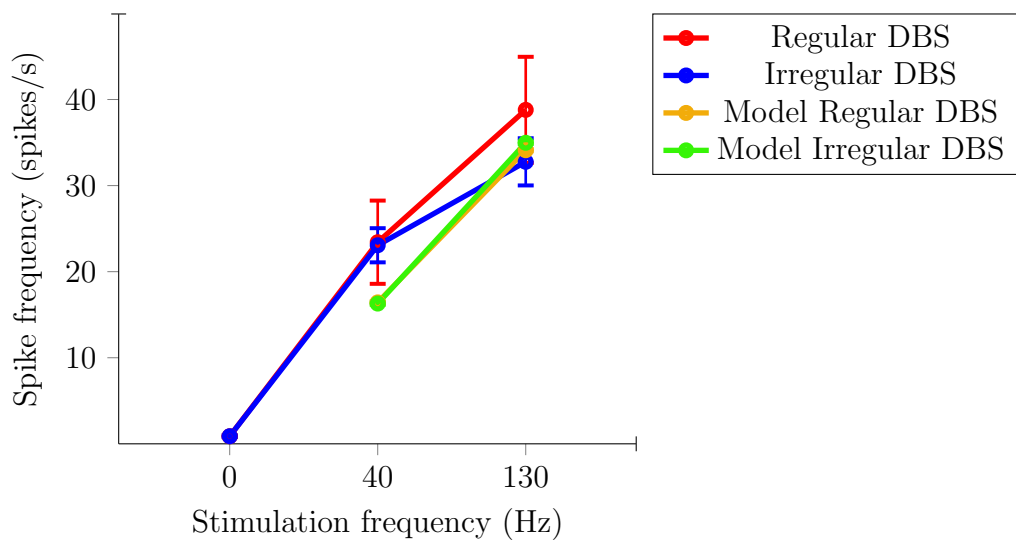


Figure 5.4: Average *in vivo* firing rate of neurons with and without stimulation administered. For reference, the results from the computational model are also plotted here. Values reported are the mean \pm SEM.

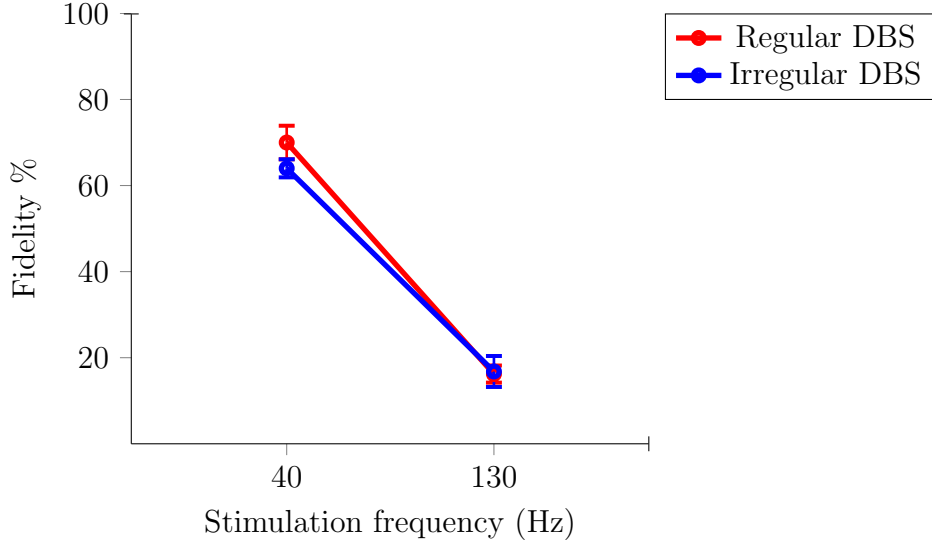


Figure 5.5: Ratio of antidromic spikes to total stimulus spikes as a function of the stimulus spike frequency.

figure, the spiking rate increases with the stimulation frequency. However, the shape of the spiking rate curve is concave. This agrees with previous work describing the decreasing fidelity of cortical neurons to antidromic activation [40], where spiking rate values were reported to decrease starting with DBS at 200 Hz. It was determined that the irregular DBS no significant effect on the firing rate relative to the regular DBS, which is expected since the average rate of stimulation is the same in both cases.

Entropy is a measure of randomness or variability. In this work, we consider how the entropy of the spike trains changes under the different stimulation conditions. The first step is to define what variable we are interested in determining the randomness of. In our case, the ISIs serve the purpose. Low entropy for the ISIs means that there is not much variability in the ISIs, in turn indicating that spiking happens at almost regular intervals. On the other side, high entropy means that there is high variability for the ISIs and spiking is very irregular.

Let X be a discrete random variable with probability mass function (pmf) $p_X(x)$.

The entropy of X , $H(X)$, is defined as

$$H(X) = - \sum_i p_X(x_i) \log_2 (p_X(x_i)), \quad (5.1)$$

where the summation is over all possible realizations of X . In general, the ISI may be represented by a continuous random variable. However, since we are working with *in vivo* data that must be quantized, ISI is considered to be modeled as a discrete random variable and the above definition holds.

To find the entropy of the ISI for M1 activity in the healthy state, we use the single-unit activity recorded from the intact hemisphere of the subjects while no stimulation was administered. The mean firing rate of the pyramidal cells was 3.6924 ± 1.44 Hz (mean \pm SEM). The empirical pmf computed from the cumulative activity of the cells analyzed is shown in Fig. 5.6. The entropy of the ISI in the hemi-parkinsonian state was computed using single-unit activity recorded from the hemisphere ipsilateral to the lesion. The mean firing rate in the hemi-parkinsonian state was 0.8821 ± 0.3393 (mean \pm SEM). The pmf of the hemi-Parkinsonian ISIs is shown in Fig. 5.7. The shapes of the two densities, for the healthy and Parkinsonian state, are very different. Healthy activity favors smaller ISIs, while the Parkinsonian activity has a larger spread of probable ISIs. The longer tail of the Parkinsonian pmf is indicative of more variable spiking activity relative to that in the healthy state and this increase in phasic activity is related to the Parkinsonian pathology.

When stimulation is administered in the STN ipsilateral to the dopaminergic lesion, antidromic spikes are induced in the projection neurons of Layer V of the motor cortex. By examining the peristimulus time histogram (PSTH), the induction of these spikes is clear based on the large peak in the distribution for low latency (≤ 2 ms) from the stimulus pulse onset. An example PSTH is shown in Fig. 5.8. After identifying antidromic spikes, we can consider the ISI pmfs for all observed

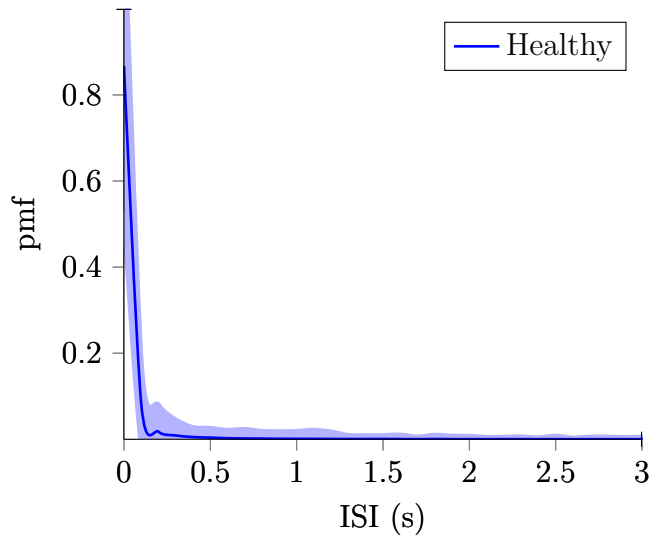


Figure 5.6: Empirical pmf of the ISI for the healthy state, computed using activity from the intact hemisphere.

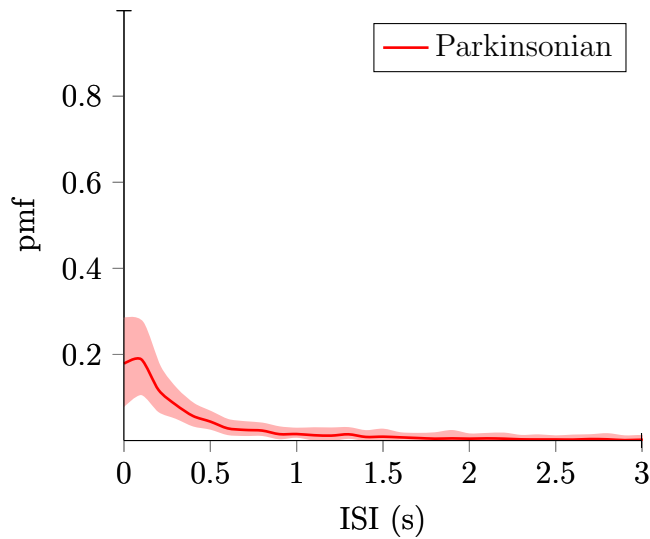


Figure 5.7: Empirical pmf of the ISI for the Parkinsonian state. The ISIs for the Parkinsonian state were computed using activity from the lesioned hemisphere.

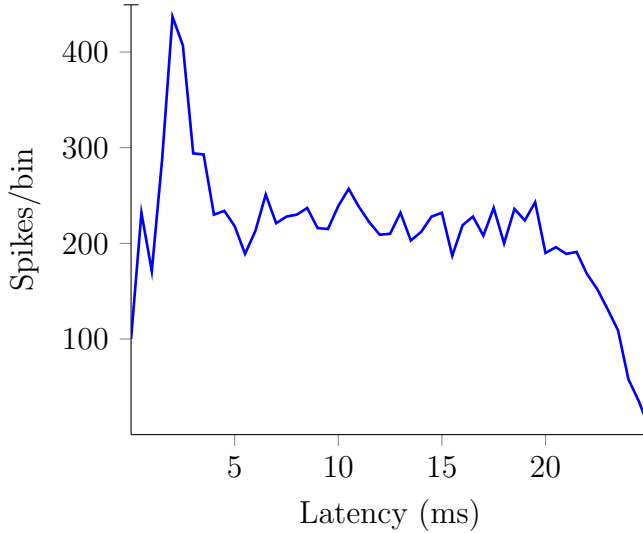


Figure 5.8: PSTH for 40 Hz irregular DBS. There is a peak in the distribution of spike times following the stimulus which indicates stimulus-locked antidromic firing of the M1 cell.

spiking and for orthodromic spiking only (i.e. no antidromic spikes). For a low rate of stimulation, the ISI distribution does not change significantly (see Fig. 5.9), but for higher rates of stimulation there is a notable difference with the presence of the antidromic spikes (see Fig. 5.10).

After calculating the appropriate pmfs, the entropy in bits per spike can be computed. Using 10 ms resolution for the ISI bins, the resultant entropy values under various conditions is shown in Fig. 5.11. Low ISI entropy is characteristic of the healthy (intact) state and the lesioning causes increased bursty firing, resulting in higher ISI entropy in the Parkinsonian state (labeled “PD” in the figure). The entropy is increased with 40 Hz stimulation, both regular and irregular, when antidromic spikes are considered but is close the Parkinsonian ISI entropy value when antidromic spikes are excluded from the computation. This is likely because 40 Hz stimulation is not intrinsically changing the firing properties of the cells and the ISI only appears more variable because of the antidromic firing. When antidromic spikes are considered, the entropy with 130 Hz stimulation (regular and irregular) is slightly lower than

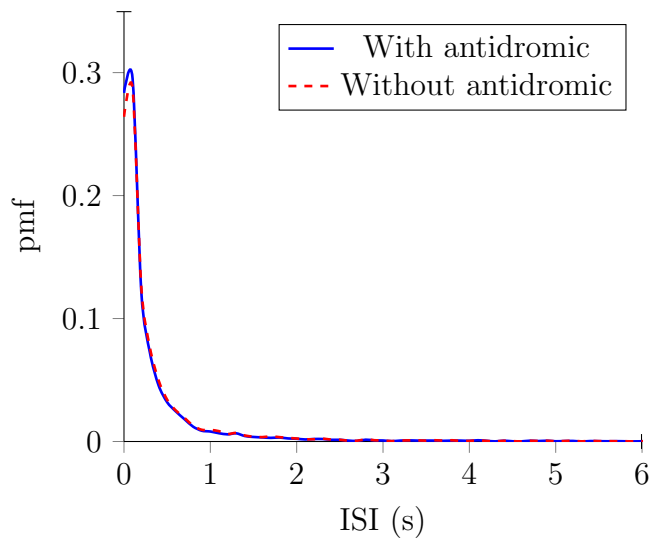


Figure 5.9: ISI pmf for 40 Hz irregular DBS.

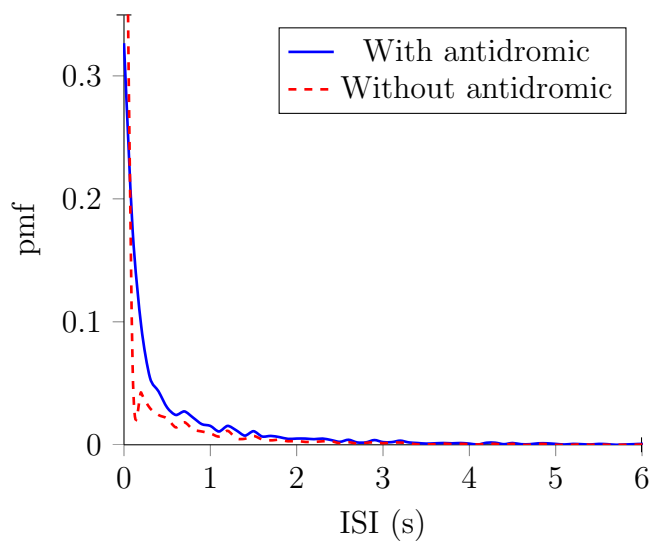


Figure 5.10: ISI pmf for 130 Hz irregular DBS.

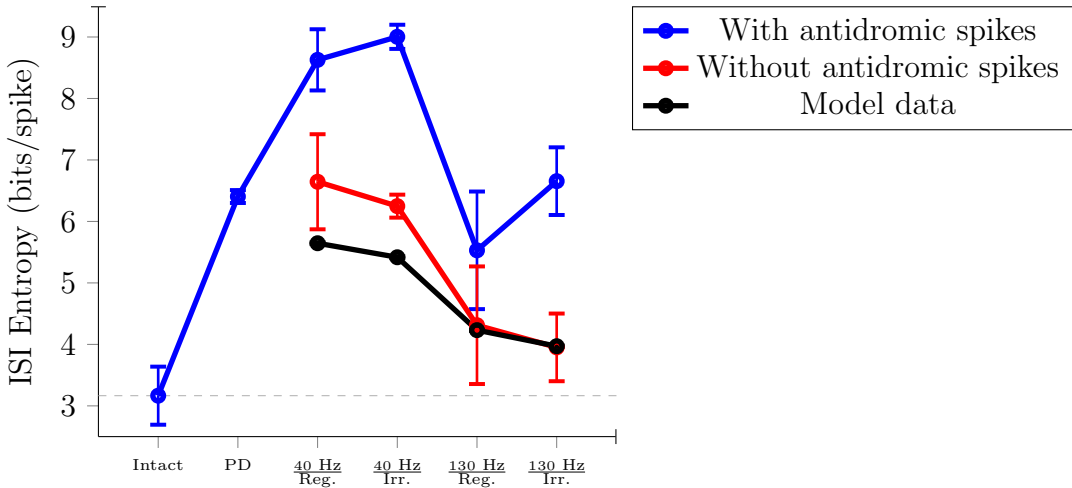


Figure 5.11: ISI entropy under multiple conditions, computed with pmfs using 10 ms bins.

that with 40 Hz stimulation. This is because the high rate stimulus-locked antidromic spikes makes the activity more regularized. However, when antidromic spikes are excluded from the analysis, the ISI entropy is much lower than in the PD state for both regular and irregular stimulation and it is clear that the firing properties of the cells have been altered. Irregular 130 Hz DBS achieves slightly lower entropy values than regular 130 Hz stimulation and drives entropic state closer to the intact condition.

5.6 LFP Results

The LFP is dominated by the voltage produced by the cumulative synaptic current flowing across the extracellular volume of tissue. An example of the raw LFP signal is shown in Fig. 5.12a. The LFP signal is initially filtered using a zero-phase finite impulse response (FIR) filter with passband from 0 to 200 Hz, resulting in a signal as shown in Fig. 5.12b. The power spectra is estimated with a multitaper method using a time-bandwidth product of 5 seconds \times Hz and 9 leading Slepian tapers [68,69]. The power spectrum is computed per tetrode per recording session and trial averaging is performed over the channels of the tetrode. Normalized power spectra under different

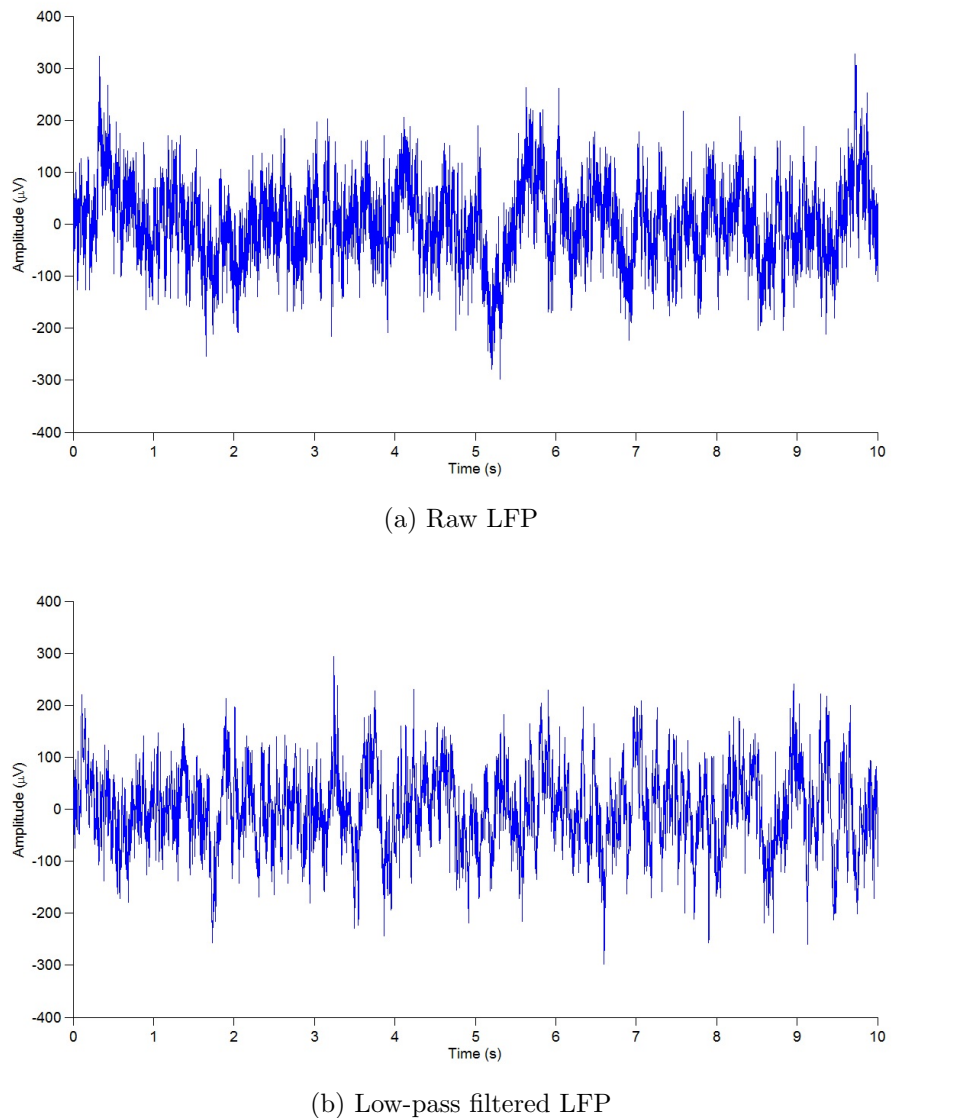


Figure 5.12: Example traces over a 10 s time window of a (a) raw LFP signal and (b) low-pass filtered LFP signal.

stimulation conditions are shown in Fig. 5.13. Confidence intervals shown as shaded regions of the same color are 95% χ^2 confidence intervals.

In the parkinsonian state, there is increased pathological activity in the β -band (13- 30 Hz). With increasing stimulation frequency, this β -band power is increasingly attenuated. Irregular DBS has a greater attenuation of the the power relative to regular DBS, as shown in Fig. 5.14. In the zoomed in view, it appears that the frequency at which the LFP signal achieves peak power within the β -band shifts depending on the stimulation frequency. In Fig. 5.15, I show the frequency at which the peak power occurs. Irregular DBS downshifts the frequency where the peak is attained, though therapeutic stimulation frequency values restore the peak frequency to around 16 Hz, which matches where the peak occurs in the healthy LFP data.

If the peak power in the β -band is considered, it is seen on average that this peak decreases with increasing stimulation frequency. In Fig. 5.16, it is clear that the lowest peak power value is achieved for 175 Hz stimulation. Additionally, the peak is attenuated more significantly with irregular DBS relative to regular DBS. For a non-therapeutic stimulation frequency , 40 Hz, there is no difference in average attenuation achieved, which is likely due to the fact that this low frequency value is generally ineffective in correcting the pathology whether or not the timing of the stimulus pulses are regular. As we increased the stimulation frequency, however, performance gains are seen when the random perturbations are added to the pulse timing. For the highest frequency tested, 175 Hz, though, the average peak power value is roughly the same. This is attributed to the fact that the shorter the period between the stimulus pulses, the smaller the temporal space is to create variation in the stimulus pulse times. Essentially, the 175 Hz stimulus train with irregular spacing has low entropy and the distribution of the inter-stimulus pulse periods is very narrow.

Similar trends are seen with the integral power in the entire β -band is calculated;

these results are shown in Fig. 5.17. The power in the Parkinsonian state is greater than in the healthy state. With increasing stimulation frequency, the total power in the β -band decreases. Adding irregularity to the stimulus pulse times also has an improved effect on the amount of β -band attenuation achieved. Thus, irregular DBS outperforms regular DBS in terms of reducing both the peak and total power in this pathological frequency band. One curiosity is the increased in peak and integral power with 40 Hz DBS relative to the power in the Parkinsonian state. This could indicate that low frequency stimulation is not only therapeutically ineffective but also possibly mildly exacerbates the pathology. High frequency stimulation, however, succeeds in treating the motor symptoms, as discussed in the previous chapter, and ameliorating the abnormal neural activity.

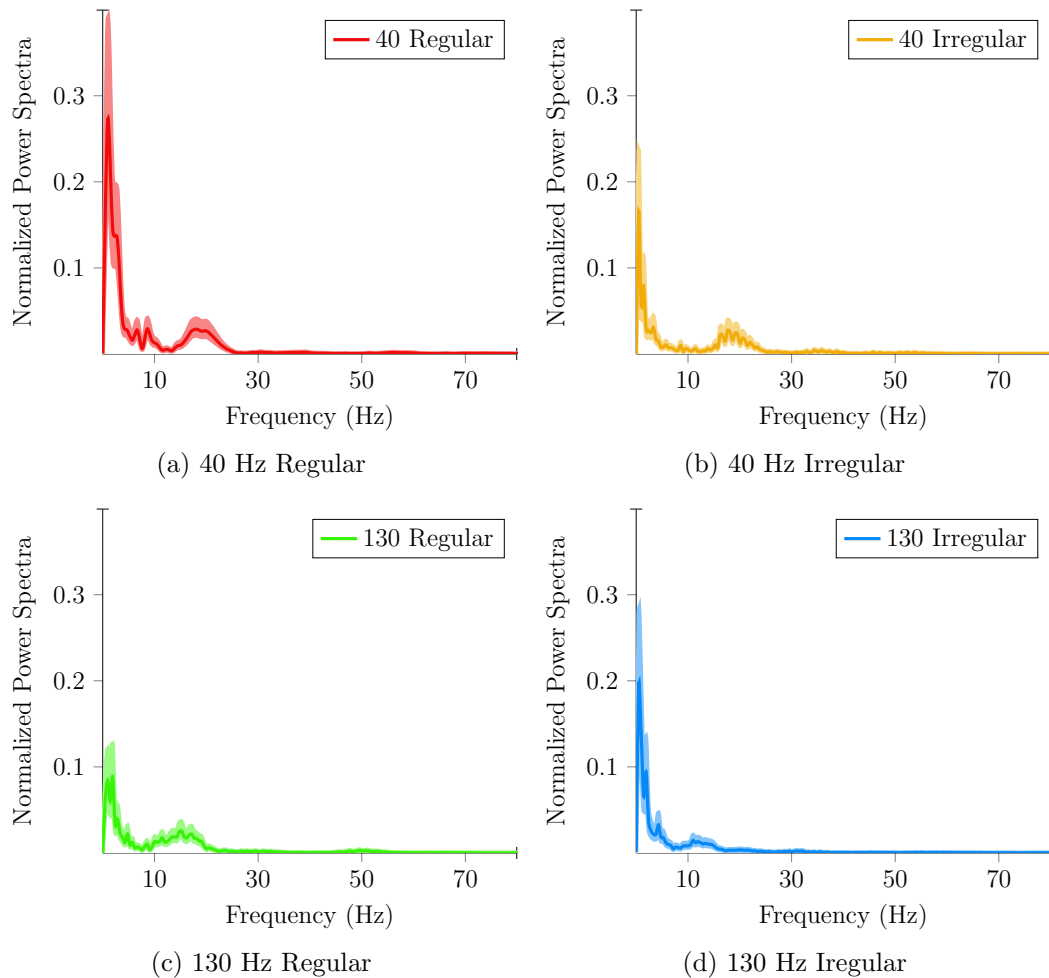


Figure 5.13: Normalized power spectra computed by using the multitaper estimation of the power spectra over the frequency window $[0, 100]$ Hz.

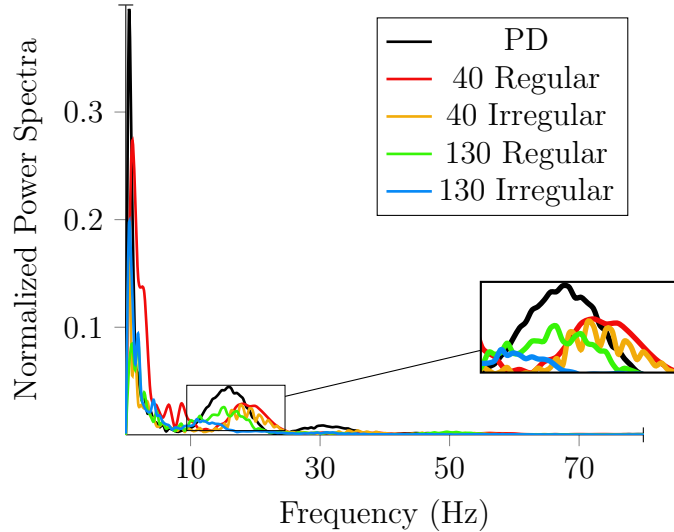


Figure 5.14: Comparison of power spectra under four different stimulation conditions.

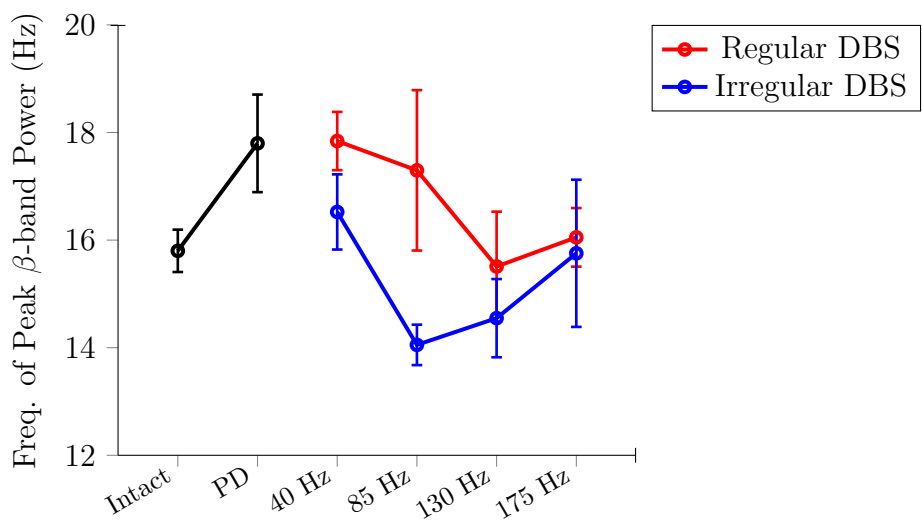


Figure 5.15: Frequency at which the peak normalized power in the β -band (13-30 Hz) occurs. Error bars are SEM.

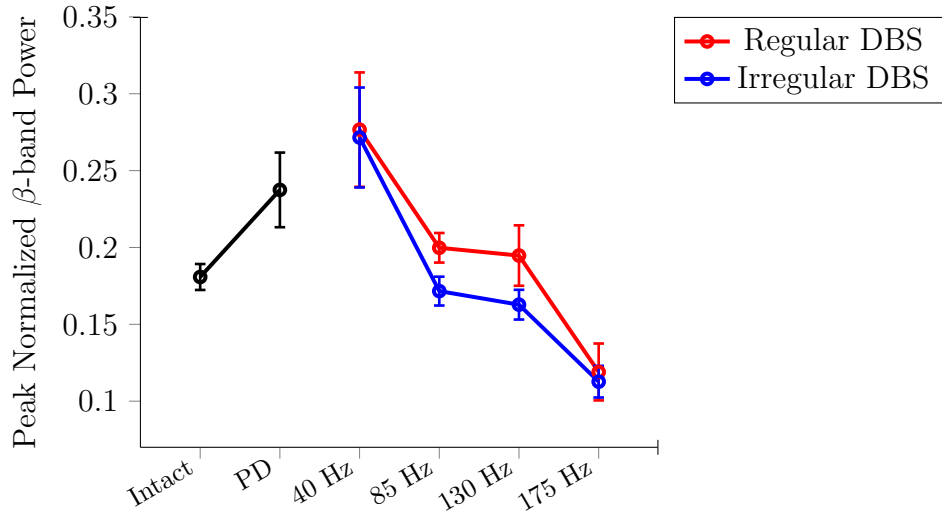


Figure 5.16: Peak normalized power in the β -band (13-30 Hz). Error bars are SEM.

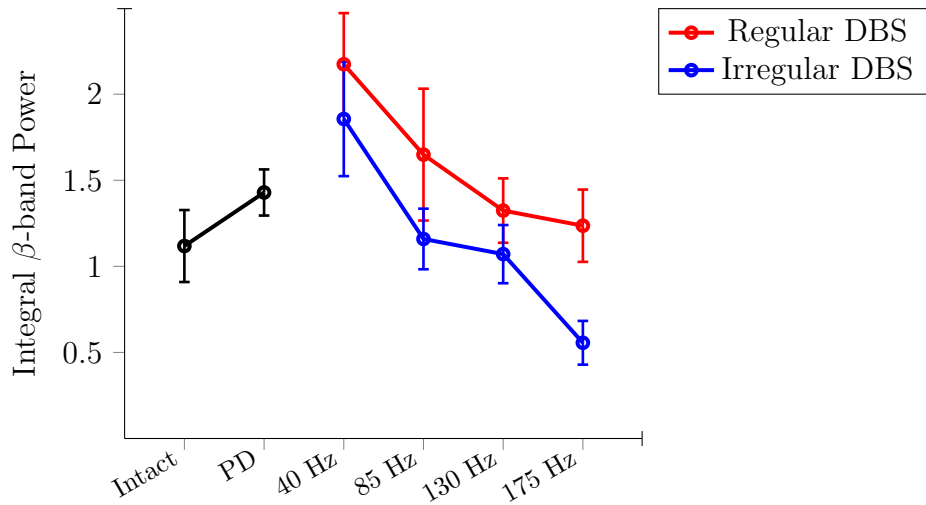


Figure 5.17: Total power in the β -band (13-30 Hz). Error bars are SEM.

CHAPTER 6

Carbon Nanotube Fiber Electrodes

For electrical stimulation, the essential component is that the electrode delivers the required amount of charge to initiate a functional response in the neural structures. Stimulating electrodes must be able to deliver the necessary amount of charge without exceeding the safety voltage potential limit (namely the “water window”), beyond which an irreversible faradaic hydrolysis reaction in the tissue will occur, remain functional for chronic use without degradation and change in the electrochemical properties, and without causing any cytotoxic effect. The charge density inversely depends on the size of the electrode contact (a.k.a. active site), and thus represents the greatest barrier towards the miniaturization of stimulating electrodes [34]. Small electrodes enable high spatial resolution and selectivity of neural responses. Moreover, the minimization of the device footprint may reduce the inflammatory foreign-body response and the mechanical damage caused by the relative micromotion with brain tissue, thus improving the overall biocompatibility of the implant [35].

Metal microelectrodes, however, are intrinsically limited in the maximum currents and charge density that can be delivered through capacitive or reversible faradaic mechanisms. Moreover, the impedance of metal microelectrodes is generally high ($> 1 \text{ MOhm}$), which greatly affects the signal-to-noise ratio and resolution of neu-

ral recordings. Tthe use of large electrodes imposed by charge density and safety requirements not only does not allow the precise targeting of stimulation.

A wide variety of materials for use in neural electrode design have been explored. Platinum (Pt) and platinum-iridium (PtIr) alloys are the most commonly adopted materials for large DBS and cochlear implants electrodes, because of the good biocompatibility and resistance to corrosion. However, due to the low charge injection limits [34] ($0.05 - 0.15 \text{ mC/cm}^2$), Pt cannot be used for the fabrication of small surface area electrodes.

Carbon nanotubes (CNT) possess electrochemical, electrical and mechanical properties at the molecular level that, alongside with large surface area and biological stability [70], make them an ideal material for neural electrode fabrication. CNTs have been used to fabricate microelectrodes for *in vitro* stimulation of hippocampal neurons, [71] as conductive coatings for metal microelectrodes [72–74], and for *in vitro* electrophysiology [75, 76]. Recently the capability of recording a low frequency signal in the rat motor cortex with a stand alone CNT-composite microelectrode has been demonstrated [CITATION]. However, because of the challenge of translating the single molecule properties in microscopic assembly and the difficulties of reliably fabricating CNT electrodes, the potential of CNT for neural electrodes has not been fully explored. Recently the Pasquali Lab at Rice University has developed CNT fibers that possess a unique combination of electrical conductivity, mechanical strength, flexibility and microscale size [77]. CNT fibers show superior specific electrical conductivity than metals and, thanks to the improved tensile strength, can be fabricated with small diameter (as low as $\approx 10\mu\text{m}$) without a significant risk of breaking. Small diameter, in turn, allows for increased flexibility, reduced impact and risk of damage to tissue surrounding the implant, and lower GSA. CNT fibers appear to be a suitable material for the fabrication of microelectrodes capable of stimulating and recording the activity of neural ensembles, but a complete study that encompasses a

comparative characterization of the *in vitro* properties and the *in vivo* assessment of biocompatibility and stimulation efficacy is still lacking.

In this study I demonstrate the method for straightforward fabrication of CNT fiber electrodes and precise insertion in deep brain structures. I show the effectiveness of CNT fibers as DBS electrodes in the rat model of Parkinson's disease and assess the biocompatibility through the analysis of long-term tissue response. Finally, I provide evidence of the neural recording quality of CNT fiber electrodes implant in the hemi-Parkinsonian rodent model.

6.1 Fabrication

CNT fibers were fabricated in the Pasquali Lab at Rice University with a wet-spinning method previously described [77]. Briefly, high concentration solutions of high quality CNTs were spun out of an orifice into a coagulant bath. The yield of a single spinning process is approximately hundreds of meters of fiber, with the diameter of individual filaments varying between 10 and 100 μm depending on the diameter of the spinning orifices and the CNT solution concentration. In this work, we used CNT fibers with diameter of 13 μm for fabrication of recording electrodes and 43 μm for fabrication of stimulating electrodes. Individual filaments of CNT fibers were coated with a $2.4 \pm 1.7 \mu\text{m}$ layer of a copolymer of polystyrene-polybutadiene (PS-b-PBD, Sigma Aldrich) for insulation, leaving only the tip exposed as an electrically active site.

Stereotrodes, i.e. two channel electrodes, were fabricated by twisting together two coated fibers with a diameter of $43 \pm 4.6 \mu\text{m}$ and average impedance of $11.2 \pm 7.6 \text{ k}\Omega$. Each channel was connected to a male pin of a male-to-male connector using conductive silver paint. For the fabrication of recording electrodes, only one channel of the tetrode's four channels was made of CNT fiber. One filament of 13 μm diameter CNT fiber was twisted with four filaments of NiCr wire, the standard material used

in this work for recording. One of the four NiCr channels was only mechanically, but not electrically, functional, essentially ensuring that the stiffness of the tetrode was sufficient to not buckle when lowered into brain tissue. The remaining three NiCr channels and CTNf channel were connected to a four-pin male-to-male connector using silver paint, which was then loaded into a microdrive and implanted as described in the previous chapter.

6.2 Stimulating Electrode

In vivo experimental studies in the hemi-Parkinsonian rodent model were performed to evaluate the efficacy of CNTf stereotrodes as stimulating electrodes for DBS. This population of rats ($N = 4$) was induced to be hemi-Parkinsonian by receiving a unilateral injection of the neurotoxin 6-hydroxydopamine (6-OHDA) in medial forebrain bundle (MFB) for retrograde transport to substantia nigra pars compacta (SNC), as described in Chapter 4. CNTf stimulating electrodes were implanted in the right entopeduncular nucleus (EP), the rat equivalent of the GPi. The same type of PtIr microelectrodes used for the previous studies were implanted contralaterally in the left EP and used as a control (Figure 6.1a). To assess the efficacy of the CNTf stereotrode for GPi-DBS, an methamphetamine rotation test was performed. Methamphetamine, a dopamine agonist, was administered intraperitoneally (I.P.) to the subjects (1.875 mg/kg; Sigma Aldrich) to induce locomotory rotations in the direction ipsilateral to the SNC lesion [11, 12, 50]. Recall, reduction in the rotation rate with DBS indicates how efficacious the therapy is. We found that DBS with CNT fiber electrodes were able to significantly reduce the normalized methamphetamine-induced rotation rate (Figure 6.1b). Moreover, it was also determined that the efficacy of treatment with CNT fiber electrodes improved as the frequency of the stimulating electrical current pulses was progressively increased from 85 to 130 Hz, thus replicating not only

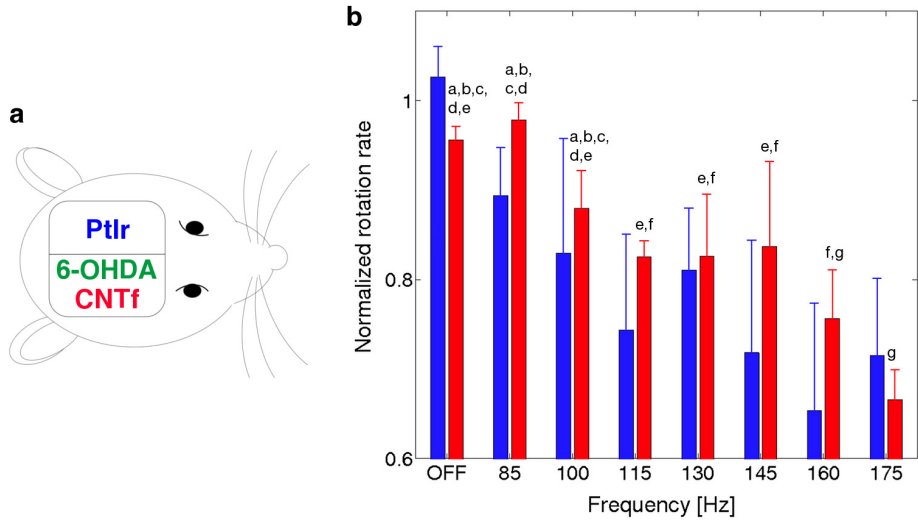


Figure 6.1: *In-vivo* characterization of CNT fiber electrodes for DBS: a) 6-OHDA dopaminergic lesion was induced on the right hemisphere. CNT fiber electrodes were implanted in the entopeduncular nucleus (EP) ipsilateral to the lesion. Commercial PtIr electrodes were in the left EP, and used as control; b) Results of the metamphetamine rotation test: average normalized rotation rate of a population of 4 Long-Evans rats implanted with CNT fiber electrodes and comparison with PtIr electrodes (error bars: SEM). Repeated measures ANOVA showed that there was significant difference between treatment conditions ($p < 0.05$). Pairwise comparison across frequencies was performed with post-hoc least square difference (LSD, $p < 0.05$). Frequencies are significantly different when do not share a letter.

qualitatively but also quantitatively the modulation of motor-symptoms with DBS we had previously observed using conventional PtIr electrodes [78]. To the authors' knowledge, our CNTf electrode is the smallest surface area electrode ever shown for successful alleviation of motor symptoms of PD via DBS in any animal model.

6.3 Recording Electrode

CNTfs of smaller diameter than used for fabricating the stimulating electrodes were used in the fabrication of recording tetrodes. These fibers were $\sim 12 \mu\text{m}$ in diameter, which is similar size to the standard NiCr wire used to create the tetrodes. This small geometric surface area allows for high spatial resolution, which is a desirable property for a recording electrode. Additionally, the fiber used had low impedance (18 – 110

$\text{k}\Omega$) which provides a better signal-to-noise ratio (SNR). Typically low impedance indicates a large conducting surface area, which corresponds to low SNR. However with the CNTf the low impedance is paired with a small geometric surface area and large effective surface area, yielding recordings with reasonable SNRs.

Tetrodes were fabricated with four NiCr wire channels and one CNTf channel. Of the four NiCr channels, three were electrical and one was mechanical. This design ensured that the electrode was stiff enough to penetrate the brain tissue without additional support. The NiCr wire channels were electroplated with gold, as previously described, to lower the impedance at the active site. The CNTf was not electroplated. Two such tetrodes were fabricated and will be referred to in the remainder of the document as CNTf tetrodes, though it is understood that only one of the four channels is made from the CNTf. The CNTf tetrodes were loaded into a microdrive that was implanted in one of the subjects that participated in the cortical recording experiments described in the previous chapter.

LFP and single-unit activity was recorded using the CNTf tetrodes over a period of two weeks following two weeks of recovery time post-operatively. The data was processed in the same fashion as data recording using NiCr tetrodes. An example waveform recorded on the CNTf channel is shown in Fig. 6.3; this waveform has a peak-to-peak voltage greater than $100 \mu\text{V}$, which is indicative of a high SNR regime. Spikes were determined to originate from the same neuron by clustering techniques previously described and an example of the resultant spike clusters is shown in Fig. ???. Since only one channel of the CNTf tetrode was fabricated from the CNTf, clustering was done using its neighboring NiCr wire channels. It is clear from the figure that the spikes can be clustered well using activity recorded from a CNTf electrode.

The LFP recorded on the CNTf channel had similar SNR and spectral properties as what was recorded on the NiCr channels of the CNTf tetrode. An overlay of a raw LFP waveform recorded from a CNTf channel and a neighboring NiCr channel is

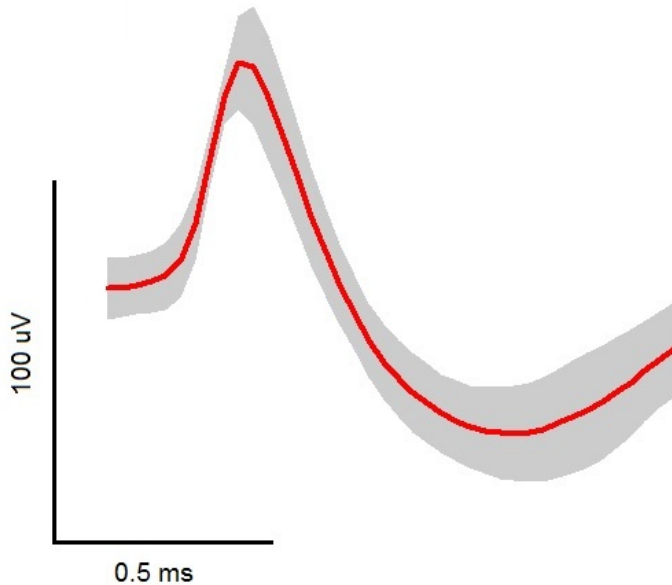


Figure 6.2: Average single-unit waveform recorded using a CNTf electrode. The shaded region indicates the S.D. of the mean waveform values.

shown in Fig. 6.4. Although the two electrodes are in different spatial locations, the extracellular activity is very similar and results in almost identical raw LFP traces. This supports the conclusion that the CNTf is a suitable material for neural recording since it provides good recording quality without electroplating the electrical contact, a process that imposes issues of degradation and lack of long-term stability which critically limits the use for chronic recording.

6.4 Histology

6.4.1 Acute Histology

In the case of neural microelectrodes, the acute reaction is caused by the trauma from surgical insertion of the electrode and is strongly dependent on the insertion strategy as well as implant size. The stab wound created during surgical insertion may induce disruption of blood vessels and the blood brain barrier (BBB), causing

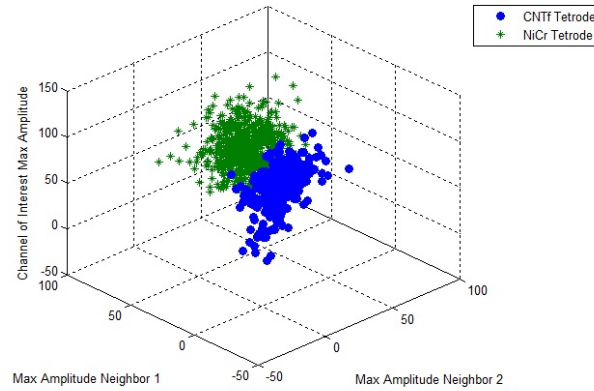


Figure 6.3: Example clusters formed by plotting the peak waveform amplitudes recorded across three of the four channels from two different tetrodes. The z-axis shows the peak amplitude on either the CNTf channel of a CNTf tetrode or on a NiCr channel of a standard tetrode. The x- and y-axes are peak waveform amplitudes from two of the NiCr channels in the same tetrode as the channel shown on the z-axis.

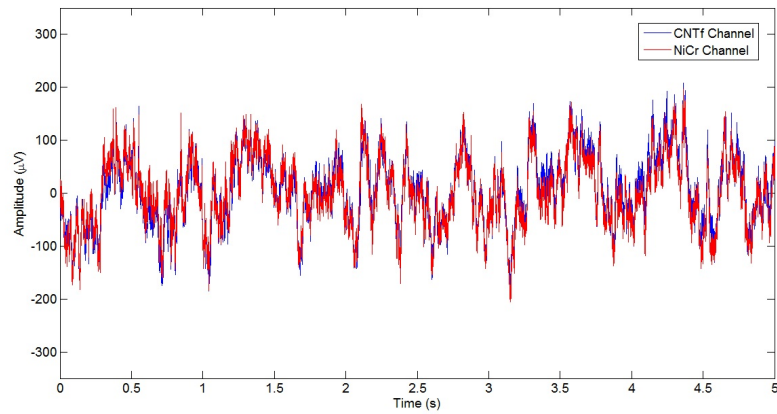


Figure 6.4: Raw LFP signal from a CNTf channel and a NiCr channel of the same tetrode.

the extravasation of erythrocytes, activation of the coagulation cascade, edema, and accumulation of activated microphages, microglia and astrocytes around the injured area. This initial response serves to protect against inflammation and enable tissue repair. However, an excessive extension of the acute lesion can result into a worsening of the chronic inflammation [79–81]. Thus, the use of flexible microelectrodes can allow for the minimization of both the acute damage and the chronic inflammatory response.

We implanted rats ($n = 3$) with electrodes made from two different materials, CNTf and PtIr, and analyzed the acute damage caused to the BBB. 1,1'-Dioctadecyl-3,3,3',3'-tetramethylindocarbocyanine (DiI) was used to paint the blood vessels of the rat and visualize the microvasculature in the brain [82]. The presence of DiI outside of the microvasculature is an indication of a disruption of the BBB since the dye is impermeable to the BBB. The dye was prepared by mixing the crystalline powder in methanol solvent, at a concentration of 6 mg/ml, and then placing it covered on a rocker overnight at room temperature to dissolve; this preparation is consistent with previous work [82]. The mixture was filtered following dissolution of the powder in methanol.

Two electrodes were implanted bilaterally in STN (AP -3.6, ML +/- 2.6, DV - 8.1). A platinum-iridium electrode was implanted in the left hemisphere and a CNTf electrode was implanted on the right hemisphere. Following the implantation, the rat received an intravascular (IV) injection of DiI (1 ml of 6 mg/ml in methanol) at a rate of 0.5 ml/min. Immediately following dye injection, the rat received a fatal IP injection of Euthasol.

The rat was then transcardially perfused with 100 ml of pH 7.4 PBS followed by 250 ml of 4% paraformaldehyde (PFA) to fix the brain tissue, in the manner as [35] (see Supplementary Methods). The brain was removed and stored in the same PFA until it sunk in the container. Sucrose was added to create a 30% sucrose solution

in PFA and the brain was maintained in this cryoprotective solution until it reached total absorption. The brain was then frozen in Tissue-Tek and kept at -86 degrees Celsius until it was sliced. Slices were mounted using Pro-Long Gold Anti-Fade with DAPI and then imaged using a confocal microscope.

Analysis of the fluorescence intensity of the DiI from the microscope images, as shown in Fig. 6.5, demonstrates that the bleeding around CNT fiber implant is comparable both as intensity and length scale with the PtIr electrode, even at the terminal site, where the size of PtIr is almost 10 times smaller than the complex CNT electrode-PI shuttle. Summary results are shown in Fig. 6.6. It is hypothesized that the contained acute damage is due to the combined effects of CNT fiber flexibility and the presence of the PEG, which dissolves during the insertion and contributes to the reduction of the shear stress at the interface between the CNT fiber implant and the tissue [83].

6.4.2 Chronic Histology

At 6 weeks post-op, subjects were anesthetized and administered a fatal I.P. injection of Euthasol (0.5 - 2 ml; Virbac AH Inc.) and then transcardially perfused with 250 ml of a 10% isotonic sucrose solution followed by 250 ml of 4% PFA. The brain was removed and the electrodes were explanted at this time. The tissue was allowed to fix in PFA for 1-2 days at 4 degrees Celcius, to ensure complete absorption. Sucrose was then added to create a 30% sucrose solution in PFA to aid in cryoprotection of the tissue and the brain was maintained in this solution at fridge temperature until it sunk in the solution. The tissue was then frozen in Tissue-Tek OCT and kept at -80 degrees Celsius until it was sliced. Frozen tissue was sliced coronally into 30 μ m sections using a cryostat machine (microtome) and stored in PBS. Sections were then immunostained for laminin (vasculature), endothelial barrier antigen (EBA; endothelial cells), glial fibrillary acidic protein (GFAP; astrocytes), ionized calcium

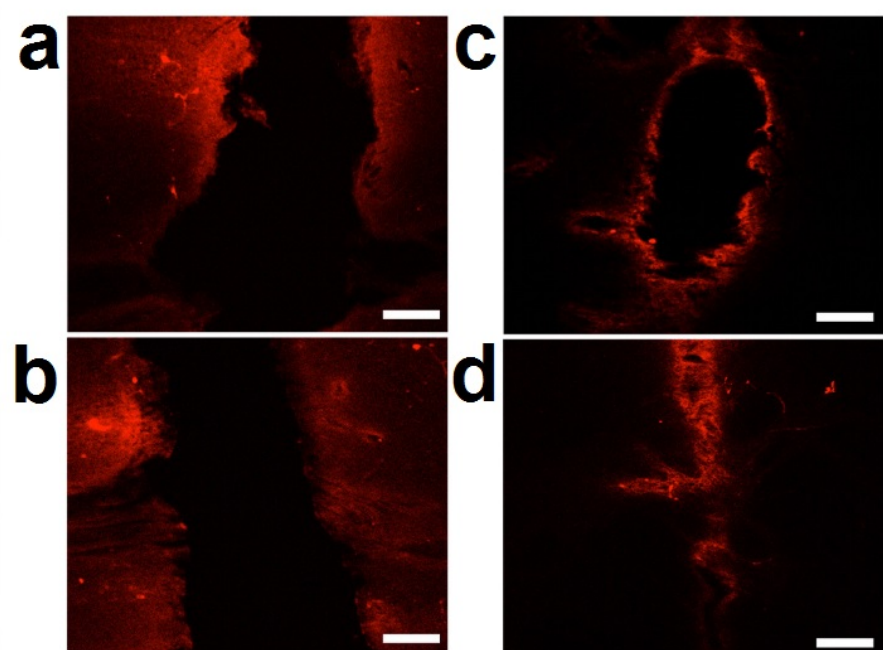


Figure 6.5: Histological analysis of the acute damage to the BBB due to electrode insertion: a) CNT fiber electrode at the entry location, and b) at the tip; c) PtIr electrode at the entry location and d) at the tip (scale bars: 100 μm ; error bars: SEM).

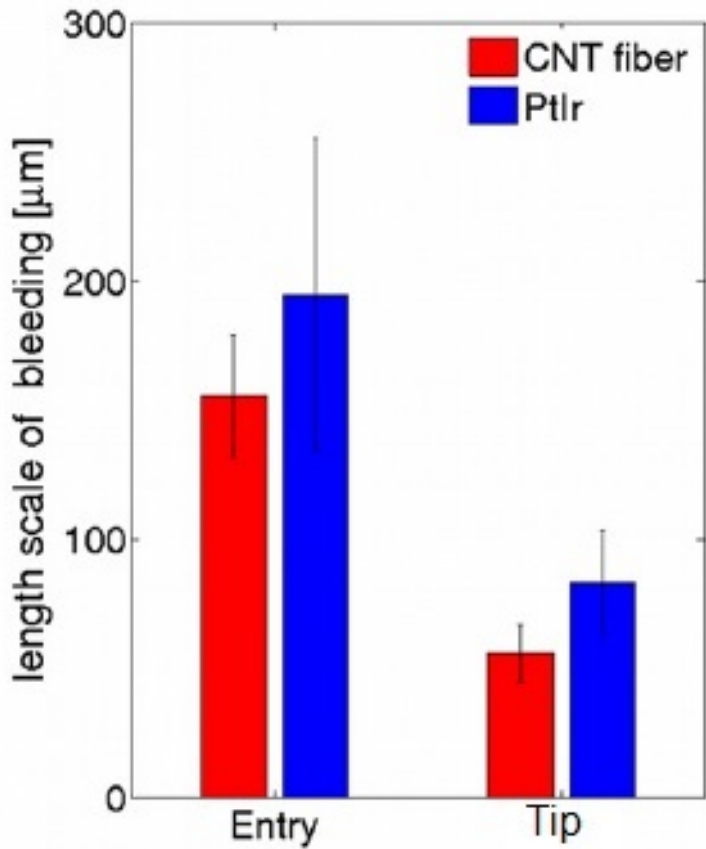


Figure 6.6: Fluorescence intensity profiles from the center of the electrode at the entry point and at the tip (error bars: SEM).

binding adapter molecule 1 (Iba1; microglia), neuronal nucleic acid (neurons), and nucleic acid (all cells).

CNT fiber electrodes caused a four-fold reduction in the accumulation of astrocytes, as marked by the expression of GFAP, and a two-fold reduction in the expression of general microglia, as marked by the expression of Iba1, at the implant site, indicating a reduction in the reactive gliotic scar formation and electrode encapsulation [80, 84]. Even more interesting results were observed for the analysis of the inflammatory response. Activated macrophages expression was found to be confined to be within approximately 50 μm adjacent to the implant and to be more than two times lower than at the site of the PtIr implant, where the zone of activation extended to more than 150 μm away from the implant. Recently, several studies have revealed the importance of the different macrophage phenotype in determining the effects of the inflammatory response. Depending on the nature and on the time-course of the injury, activated microglia/macrophage can differentiate into predominantly ‘pro-inflammatory’ phenotype M1 or into ‘anti-inflammatory’ phenotype M2 [84–86]. M1 macrophages produces oxidative metabolites and proinflammatory cytokines that are toxic to the surrounding tissue and have neurodegenerative effects, whereas M2 phenotype has been found to promote angiogenesis, matrix remodeling and fibrosis. Thus, upregulated expression of M1 macrophages is an indication of active, neurotoxic inflammatory processes and upregulation of M2 expression can be indicative of tissue repair processes, but also of formation of fibrotic scar [86]. When stained for surface markers of M1 and M2 macrophages, a very low upregulation of both phenotypes could be observed at the site of CNT fiber implant; conversely, an evident increase with respect to background levels was observed around the PtIr electrodes, particularly in the case of the M2 phenotype. These results could suggest a more extended fibrotic scar around the PtIr electrode, which is also consistent with the higher levels of GFAP and Iba1 that was found after 6 weeks post-implantation.

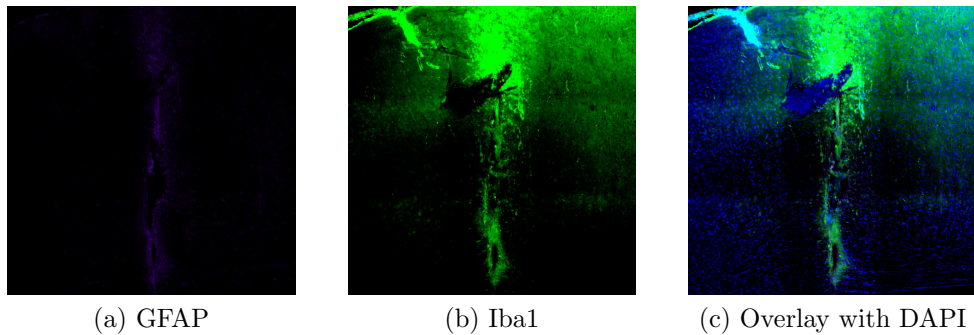


Figure 6.7: Two markers are used to characterize the gliosis that occurs after chronic implantation of the PtIr electrode. (a) Astrocyte marker (GFAP), (b) Microglia marker (Iba1), (c) Overlay with DAPI.

A weaker neuronal population was found in correspondence of CNT fiber implant, with a two time more extended zone of neurodegeneration in comparison with PtIr. We hypothesize that this was caused by the electrode implant procedure [81], where the footprint of the complex CNT fiber electrodes and PI stiffener was larger than the PtIr microelectrode. BBB function is crucial for the regulation of tissue homeostasis and protection of neurons from exposure to neurotoxic blood serum proteins [87, 88]; moreover, damage to the BBB has been shown to correlate with degradation of electrode functions [89]. The integrity of the BBB was observed by the amount of laminin, as this is normally excluded from healthy, uninjured brain tissue; the amount of laminin around the electrode was found to be higher in the case of CNT fiber electrode; however, the distribution of laminin is broader around the PtIr electrode with a characteristic length scale of fluorescence decrease of $100 \mu\text{m}$, indicating a wider diffusion of the extravasation of blood serum proteins than caused by the CNT fiber electrode, where the length scale was found to be $60 \mu\text{m}$. Overall the result of the chronic histology analysis suggest that CNT fibers do not induce cytotoxic reactions and, thanks to the flexibility and reduced size, allow for an improvement of the overall biocompatibility of the device.

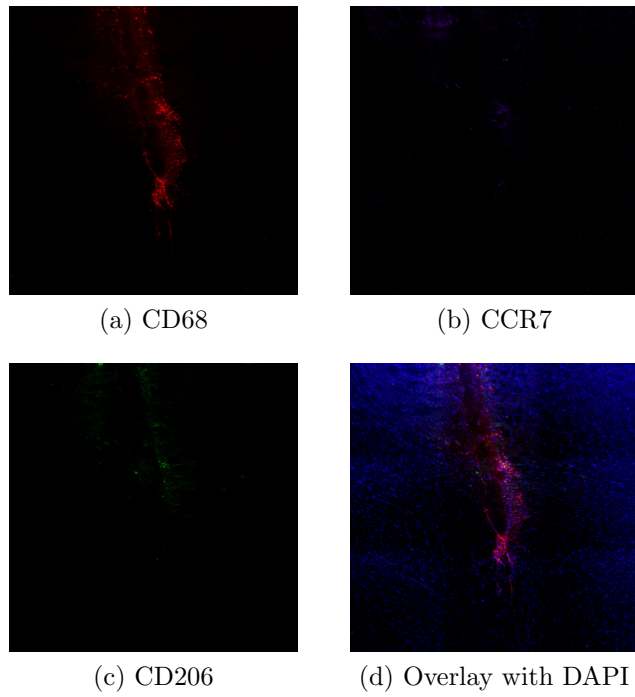


Figure 6.8: Presence of activated macrophages is used to classify the level of inflammation induced from the PtIr electrode implant. (a) General stain for activated macrophages, (b) M1 macrophages, (c) M2 macrophages, (d) Overlay image with DAPI.

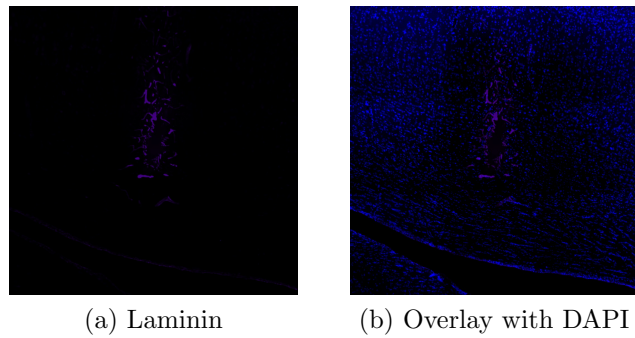


Figure 6.9: Laminin lines the blood vessels and staining for laminin may be used to indicate damage to the BBB due to the chronic presence of a PtIr electrode. (a) Laminin, (b) Laminin and DAPI co-stain.

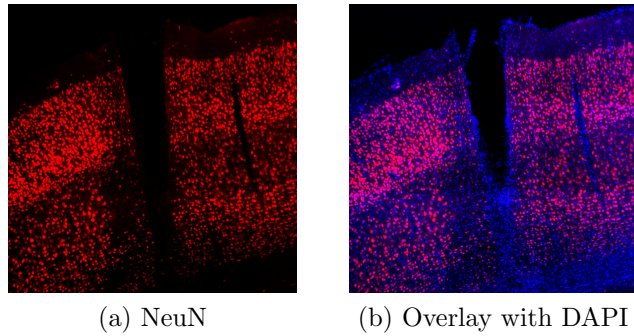


Figure 6.10: NeuN stain of tissue with PtIr implant. NeuN antibody identifies neuronal nuclei in order to label neurons. (a) NeuN, (b) NeuN and DAPI overlay. Recall that DAPI is a nuclei stain and labels all cells, including neurons.

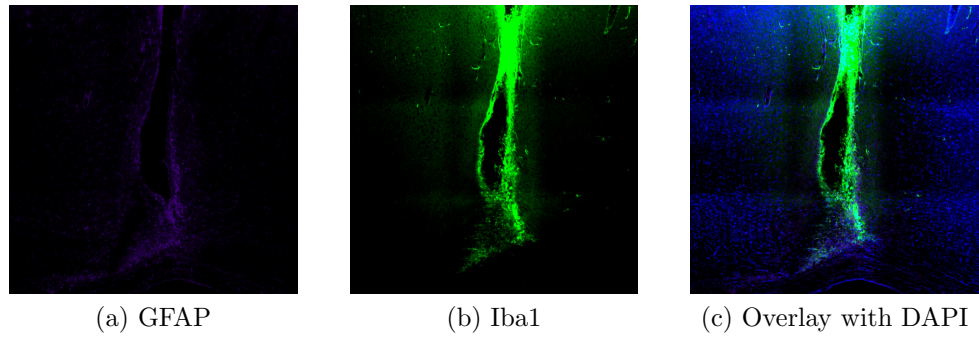


Figure 6.11: Two markers are used to characterize the gliosis that occurs after chronic implantation of the CNTf electrode. (a) Astrocyte marker (GFAP), (b) Microglia marker (Iba1), (c) Overlay with DAPI.

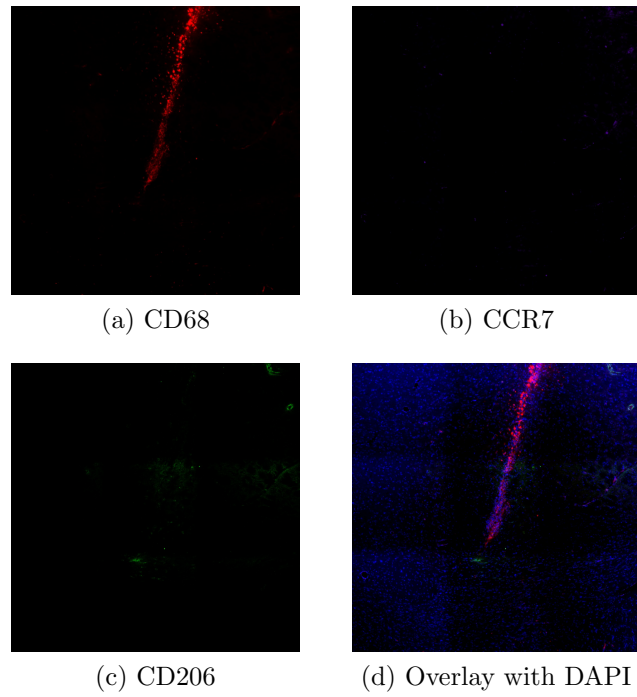


Figure 6.12: Presence of activated macrophages is used to classify the level of inflammation induced from the CNTf electrode implant. (a) General stain for activated macrophages, (b) M1 macrophages, (c) M2 macrophages, (d) Overlay image with DAPI.

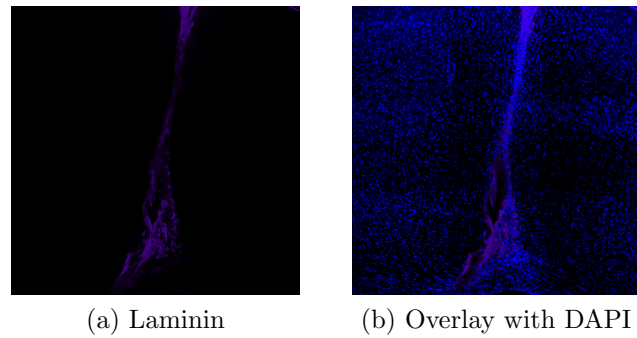


Figure 6.13: Laminin lines the blood vessels and staining for laminin may be used to indicate damage to the BBB due to the chronic presence of a CNTf electrode. (a) Laminin, (b) Laminin and DAPI co-stain.

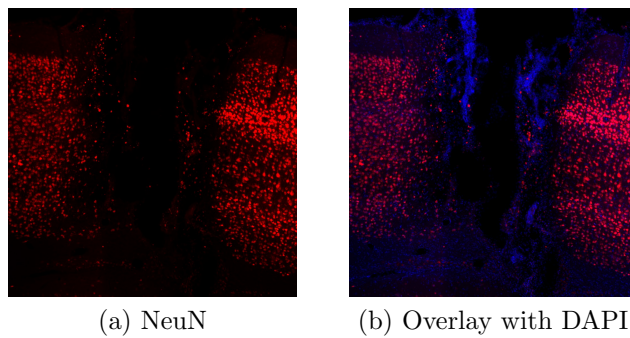


Figure 6.14: NeuN stain of tissue with CNTf implant. NeuN antibody identifies neuronal nuclei in order to label neurons. (a) NeuN, (b) NeuN and DAPI overlay. Recall that DAPI is a nuclei stain and labels all cells, including neurons.

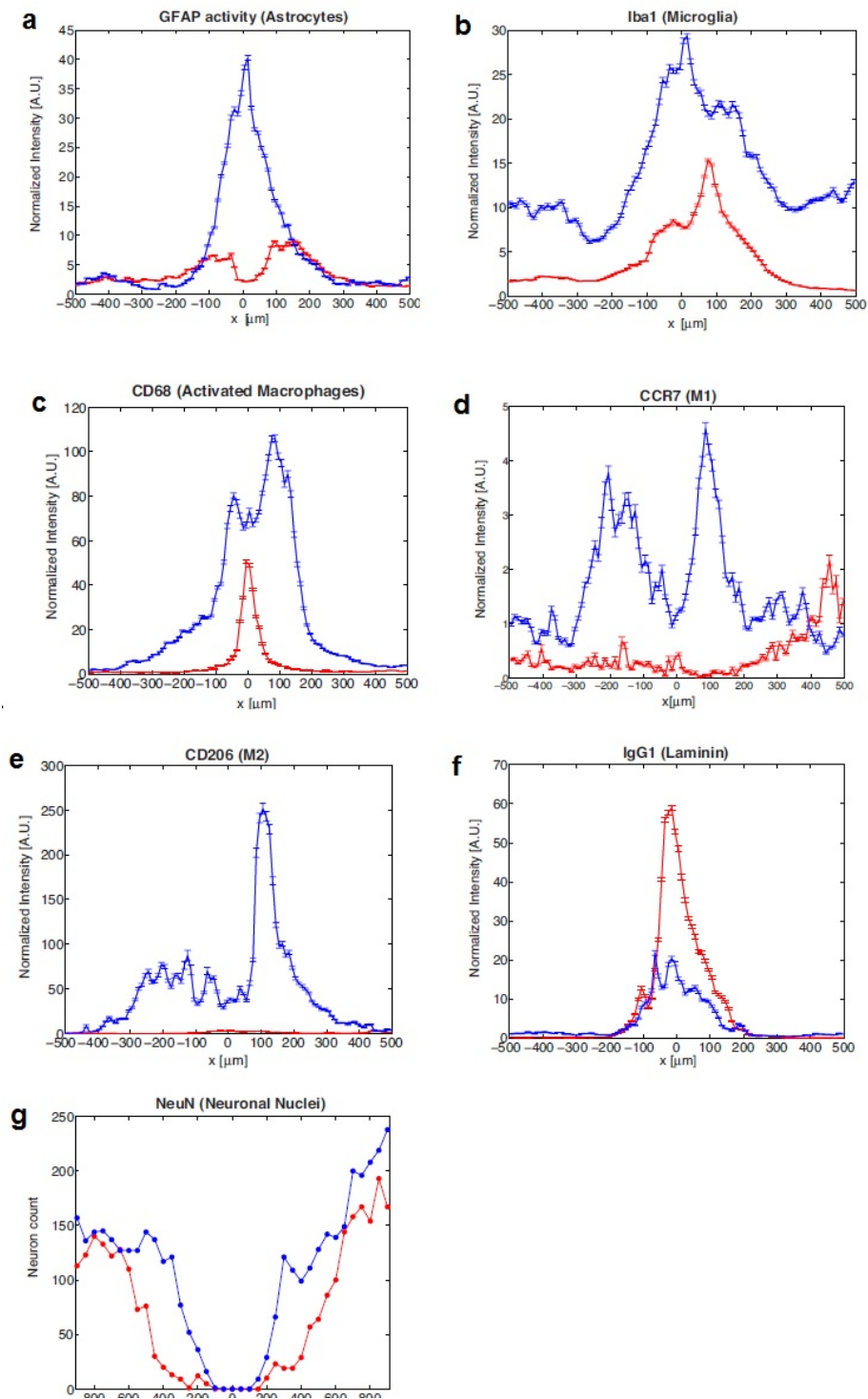


Figure 6.15: Fluorescence intensity profiles at increasing lateral distance from electrode tract: a) astrocytes, b) microglia, c) activated macrophages, d) M1 macrophages, e) M2 macrophages, f) laminin, g) neuronal count. Error bar: SEM

CHAPTER 7

Conclusions

This thesis studies multiple aspects of DBS as a treatment for PD, from evaluating models of the neural structures to investigating new materials for interfacing with the brain tissue. I presented system-level models of important BG structures, which were shown to replicate important characteristics of the biological nuclei. I represented the activity of a given nucleus using a small number (< 20) of conductance-based models of individual cells. Two different types of DBS stimulation patterns were evaluated using these models: regular and irregular DBS. It was shown that irregular DBS provided a greater mixture in firing rate change response, which has previously been shown to be correlated with therapeutic behavioral improvement. Also, the model of the activity traversing the hyperdirect pathway between the output layer of the primary motor cortex and STN was demonstrated to faithfully reproduce stimulation-frequency dependent effects reported in the literature [40].

The same stimulation patterns were also investigated for STN-DBS in the hemi-Parkinsonian rat model, which enabled simultaneous recording from both an intact and lesioned hemisphere while stimulation was unilaterally administered. Recordings were done in the primary motor cortex and it was shown that therapeutic DBS (130 Hz) reduced the pathological entropic noise. Also, the results indicated that

β -band power was monotonically decreased with increasing stimulation frequency, with greater attenuation occurring for irregular stimulation patterns. This same rodent model was also used to develop a model for the frequency-dependent behavioral changes associated with GPi-DBS. Two tests of motor asymmetry indicated improving alleviation of the asymmetry with increasing stimulation frequency. A therapeutic threshold was validated, where stimulation frequencies above this threshold provided statistically significant betterment in performance. Ambulation was characterized and similar trends were established. For a fixed frequency I also evaluated measures of hypokinesia and anhedonia. Without tuning of the current amplitude, the population was found to have a graded response to DBS, which is consistent with what is observed in human studies where stimulation parameters are tuned and adjusted over time to increase efficacy [61–63].

Finally, the same animal model was used as a vehicle for determining the biocompatibility of a potential new material for fabricating stimulating and recording electrodes. Carbon nanotube fibers are highly conductive, electrochemically stable, strong, flexible, and microscale in size. These properties make it an attractive alternative to current materials. I show that a stimulating electrode made from this material works just as well as standard commercial electrodes in terms of the therapeutic benefits achieved with STN-DBS in the hemi-Parkinsonian rat model. Also, I show that recording electrodes made from this material achieve good signal-to-noise ratio (SNR) for single-unit and local field potential (LFP) recordings. Finally, the immunoresponse to acute and chronic damage is characterized. It is concluded that this fiber is a promising biocompatible alternative material to standard metals for electrode fabrication.

References

- [1] A. Lozano, J. Dostrovsky, R. Chen, and P. Ashby, “Deep brain stimulation for Parkinson’s disease: disrupting the disruption,” *Lancet Neurol.*, vol. 1, pp. 225–231, Aug. 2002. 1
- [2] S. A. Factor and W. J. Weiner, *Parkinson’s disease: diagnosis and clinical management*. Demos Medical Publishing, 2002. 1
- [3] M. Alam, H. H. Capelle, K. Schwabe, and J. K. Krauss, “Effect of deep brain stimulation on levodopa-induced dyskinesias and striatal oscillatory local field potentials in a rat model of Parkinson’s disease,” *Brain Stimul.*, vol. 7, pp. 13–20, Jan.-Feb. 2014. 1, 2, 4
- [4] W. Meissner, D. Harnack, N. Hoessle, E. Bezard, C. Winter, R. Morenstern, and A. Kupsch, “High frequency stimulation of the entopeduncular nucleus has no effect on striatal dopaminergic transmission,” *Neurochem Int.*, vol. 44, pp. 281–286, Mar. 2004. 1, 2, 4
- [5] W. Meissner, G. Paul, T. Reum, R. Reese, R. Sohr, R. Morgenstern, and A. Kupsch, “The influence of pallidal deep brain stimulation on striatal dopaminergic metabolism in the rat,” *Neurosci. Lett.*, vol. 296, pp. 149–152, Dec. 2000. 1, 2, 4
- [6] C. Perier, C. Marin, A. Jimenez, M. Bonastre, E. Tolosa, and E. C. Hirsch, “Effect of subthalamic nucleus or entopeduncular nucleus lesion on levodopa-induced neurochemical changes within the basal ganglia and on levodopa-induced motor alterations in the 6-hydroxydopamine-lesioned rats,” *J. Neurochem.*, vol. 86, pp. 1328–1337, Sep. 2003. 1, 2, 4
- [7] A. C. Sutton, W. Yu, M. E. Calos, L. E. Meuller, M. Berk, J. Shim, E. S. Molho, J. M. Brotchie, P. L. Carlen, and D. S. Shin, “Elevated potassium provides an ionic mechanism for deep brain stimulation in the hemiparkinsonian rat,” *Eur. J. Neurosci.*, vol. 37, pp. 231–241, Jan. 2013. 1, 2, 4
- [8] A. C. Sutton, W. Yu, M. E. Calos, A. B. Smith, A. Ramirez-Zamora, E. S. Molho, J. G. Pilitsis, J. M. Brotchie, and D. S. Shin, “Deep brain stimulation of the sub-

- stantia nigra pars reticulata improves forelimb akinesia in the hemiparkinsonian rat," *J. Neurophysiol.*, vol. 109, pp. 363–374, Jan. 2013. 1, 2, 4
- [9] J.-Y. Chang, L.-H. Shi, F. Luo, W.-M. Zhang, and D. J. Woodward, "Studies of the neural mechanisms of deep brain stimulation in rodent models of Parkinson's disease," *Neurosci. Biobehav. Rev.*, vol. 32, pp. 352–366, Oct 2007. 1, 2, 4, 4.2.2, 5.3
- [10] Y. Temel, V. Visser-Vandewalle, B. Aendekerk, B. Rutten, S. Tan, B. Scholtissen, C. Schmitz, A. Blokland, and H. W. Steinbusch, "Acute and separate modulation of motor and cognitive performance in Parkinsonian rats by bilateral stimulation of the subthalamic nucleus," *Exp. Neurol.*, vol. 193, pp. 43–52, May 2005. 1, 2, 4, 4.2.4, 4.2.4, 4.3.3, 4.3.4, 5.3
- [11] G. C. McConnell, R. Q. So, J. D. Hilliard, P. Lopomo, and W. M. Grill, "Effective deep brain stimulation suppresses low-frequency network oscillations in the basal ganglia by regularizing neural firing patterns," *J. Neurosci.*, vol. 32, pp. 15 657–15 668, Nov. 2012. 1, 2, 3, 3.4, 4, 4.2.1, 4.2.1, 4.3.1, 4.3.3, 5, 5.3, 6.2
- [12] F. Rauch, K. Schwabe, and J. K. Krauss, "Effect of deep brain stimulation in the pedunculopontine nucleus on motor function in the rat 6-hydroxydopamine Parkinson model," *Behav. Brain Res.*, vol. 210, pp. 46–53, Jun. 2010. 1, 2, 4, 4.2.1, 5.3, 6.2
- [13] M. T. Chen, M. Morales, D. J. Woodward, B. J. Hoffer, and P. H. Janak, "In vivo extracellular recording of striatal neurons in the awake rat following unilateral 6-hydroxydopamine lesions," *Exp. Neurol.*, vol. 171, pp. 72–83, Sep. 2001. 1, 4.2.1
- [14] M. Lundblad, M. Andersson, C. Winkler, D. Kirik, N. Wierup, and M. A. Cenci, "Pharmacological validation of behavioral measures of akinesia and dyskinesia in a rat model of Parkinson's disease," *Eur. J. Neurosci.*, vol. 15, pp. 120–132, Jan. 2002. 1
- [15] L. H. Shi, D. J. Woodward, F. Luo, K. Anstrom, T. Schallert, and J. Y. Chang, "High-frequency stimulation of the subthalamic nucleus reverses limb-use asymmetry in rats with unilateral 6-hydroxydopamine lesions," *Brain Res.*, vol. 1013, pp. 98–106, Jul. 2004. 1
- [16] J. L. Hudson, C. G. van Horne, I. Strömberg, S. Brock, J. Clayton, J. Masserano, B. J. Hoffer, and G. A. Gerhardt, "Correlation of apomorphine- and amphetamine-induced turning with nigrostriatal dopamine content in unilateral 6-hydroxydopamine lesioned rats," *Brain Res.*, vol. 626, pp. 167–174, Oct. 1993. 1, 4.2.1
- [17] T. Hashimoto, C. M. Elder, M. S. Okun, S. K. Patrick, and J. L. Vitek, "Stimulation of the subthalamic nucleus changes the pattern of pallidal neurons," *J. Neurosci.*, vol. 23, pp. 1916–1923, Mar. 2003. 2, 3, 3.1, 3.5

- [18] M. Magnin, A. Morel, and D. Jeanmonod, “Single-unit analysis of the pallidum, thalamus and subthalamic nucleus in Parkinsonian patients,” *Neurosci.*, vol. 96, pp. 549–564, Mar. 2000. 2
- [19] C. Beurrier, L. Garcia, B. Bioulac, and C. Hammond, “Subthalamic nucleus: a clock inside basal ganglia?” *Thalamus Relat. Syst.*, vol. 2, pp. 1–8, Dec. 2002. 2
- [20] V. C. Anderson, K. J. Burchiel, P. Hogarth, J. Favre, and J. P. Hammerstad, “Pallidal vs subthalamic nucleus deep brain stimulation in Parkinson disease,” *Arch. Neurol.*, vol. 62, pp. 554–560, Apr. 2005. 2
- [21] M. S. Okun, H. H. Fernandez, S. S. Wu, L. Kirsch-Darrow, D. Bowers, F. Bova, M. Suelter, C. E. Jacobson, X. Wang, C. W. Gorden Jr., P. Zeilman, J. Romrell, P. Martin, H. Ward, R. L. Rodriguez, and K. D. Foote, “Cognition and mood in Parkinson’s disease in subthalamic nucleus versus globus pallidus interna deep brain stimulation: The COMPARE trial,” *Ann. Neurol.*, vol. 65, pp. 586–595, May 2009. 2, 4.3.3
- [22] J. Massano and C. Garrett, “Deep brain stimulation and cognitive decline in Parkinson’s disease: a clinical review,” *Front. Neurol.*, vol. 3, pp. 1–13, Apr. 2012. 2, 4.3.3
- [23] M. S. Okun and K. D. Foote, “Subthalamic nucleus vs globus pallidus interna deep brain stimulation, the rematch: will pallidal deep brain stimulation make a triumphant return?” *Arch. Neurol.*, vol. 62, pp. 533 – 536, Apr. 2005. 2
- [24] L. Mallet, M. Schüpbach, K. N’Diaye, P. Remy, E. Bardinet, V. Czernecki, M. L. Welter, A. Pelissolo, M. Ruberg, Y. Agid, and J. Yelnik, “Stimulation of subterritories of the subthalamic nucleus reveals its role in the integration of the emotional and motor aspects of behavior,” *Proc. Natl. Acad. Sci. USA*, vol. 104, pp. 10 661 – 10 666, May 2007. 2
- [25] C. Hamani and Y. Temel, “Deep brain stimulation for psychiatric diseases: contributions and validity of animal models,” *Sci. Transl. Med.*, vol. 4, pp. 1–12, Jul. 2012. 2, 4
- [26] M. Troche, A. Brandimore, K. Foote, T. Morishita, D. Chen, K. Hegland, and M. Okun, “Swallowing outcomes following unilateral stn vs. gpi surgery: A retrospective analysis,” *Dysphagia*, pp. 1–7, Mar. 2014. 2
- [27] V. J. Odekerken, T. van Laar, M. J. Staal, A. Mosch, C. F. Hoffmann, P. C. Nijssen, G. N. Beute, J. P. van Vugt, M. W. Lenders, M. F. Contarino, M. S. Mink, L. J. Bour, P. van den Munckhof, B. A. Schmand, R. J. de Haan, P. R. Schuurman, and R. M. de Bie, “Subthalamic nucleus versus globus pallidus bilateral deep brain stimulation for advanced Parkinson’s disease (NSTAPS study): a randomised controlled trial,” *Lancet Neurol.*, vol. 12, pp. 37–44, Jan. 2013. 2, 4, 4.3.3

- [28] S.-Y. Lim, S. S. O'Sullivan, K. Kotschet, D. A. Gallagher, C. Lacey, A. D. Lawrence, A. J. Lees, D. J. O'Sullivan, R. F. Peppard, J. P. Rodrigues, A. Schrag, P. Silberstein, S. Tisch, and A. H. Evans, "Dopamine dysregulation syndrome, impulse control disorders and punding after deep brain stimulation surgery for Parkinson's disease," *J. Clin. Neurosci.*, vol. 16, pp. 1148 – 1152, Sep. 2009. 2
- [29] M. Amalric, H. Moukhles, A. Nieoullon, and A. Daszuta, "Complex deficits on reaction time performance following bilateral intrastratial 6-OHDA infusion in the rat," *Eur. J. Neurosci.*, vol. 7, pp. 972–980, May 1995. 2, 4, 4.2.4
- [30] P. Barnéoud, S. Parmentier, M. Mazadier, J. M. Miquet, A. Boireau, P. Dubédat, and J. C. Blanchard, "Effects of complete and partial lesions of the dopaminergic mesotelencephalic system on skilled forelimb use in the rat," *Neurosci.*, vol. 67, pp. 837–848, Aug. 1995. 2, 4, 4.2.1
- [31] M. Birdno, A. Kuncel, A. Dorval, D. Turner, and W. Grill, "Tremor varies as a function of the temporal regularity of deep brain stimulation," *Neuroreport*, vol. 19, pp. 599–602, Mar. 2008. 2
- [32] A. D. Dorval, A. M. Kuncel, M. J. Birdno, D. A. Turner, and W. M. Grill, "Deep brain stimulation alleviates parkinsonian bradykinesia by regularizing pallidal activity," *J. Neurophysiol.*, vol. 104, pp. 911–921, 2010. 2
- [33] M. J. Birdno, A. M. Kuncel, A. D. Dorval, D. A. Turner, and R. E. Gross, "Stimulus features underlying reduced tremor suppression with temporally patterned deep brain stimulation," *J. Neurophysiol.*, vol. 107, pp. 364–383, 2012. 2
- [34] S. F. Cogan, "Neural Stimulation and Recording Electrodes," *Annual Review of Biomedical Engineering*, vol. 10, no. 1, pp. 275–309, Aug. 2008. 2, 6
- [35] T. D. Y. Kozai, "Kozai2012," *Nature Materials*, vol. 11, no. 12, pp. 1065–1073, Nov. 2012. 2, 6, 6.4.1
- [36] A. Hodgkin and A. Huxley, "A quantitative description of membrane current and its application to conduction and excitation in nerve," *J. Physiol.*, vol. 117, p. 500544, Aug. 1952. 3, 3.1
- [37] J. E. Rubin and D. Terman, "High frequency stimulation of the subthalamic nucleus eliminates pathological thalamic rhythymicity in a computational model," *J. Comput. Neurosci.*, vol. 16, pp. 211–235, May 2004. 3, 3.2, 3.4
- [38] Y. Guo, J. E. Rubin, C. C. McIntyre, J. L. Vitek, and D. Terman, "Thalamocortical relay fidelity varies across subthalamic nucleus deep brain stimulation protocols in a data-driven computational model," *J. Neurophysiol.*, vol. 99, pp. 1477–1492, Jan. 2008. 3, 3.4
- [39] A. Destexhe, D. Contreras, and M. Steriade, "Mechanisms underlying the synchronizing action of corticothalamic feedback through inhibition of thalamic relay cells," *J. Neurophysiol.*, vol. 79, pp. 999–1016, Feb. 1998. 3, 3.1

- [40] Q. Li, Y. Ke, D. Chan, Z.-M. Qian, K. Yung, H. Ko, G. Arbuthnott, and W.-H. Yung, “Therapeutic deep brain stimulation in Parkinsonian rats directly influences motor cortex,” *Neuron*, vol. 76, pp. 1030–1041, Dec. 2012. 3, 3.5, 5, 5.5, 7
- [41] M. D. Humphries and K. Gurney, “Network effects of subthalamic deep brain stimulation drive a unique mixture of responses in basal ganglia output,” *Eur. J. Neurosci.*, vol. 36, pp. 2240–2251, 2012. 3.2, 3.4, 3.4
- [42] F. Rattay, “The basic mechanism for the electrical stimulation of the nervous system,” *Neurosci.*, vol. 89, pp. 335–346, 1999. 3.2
- [43] S. Miocinovic, M. Parent, C. Butson, P. Hahn, G. Russo, J. Vitek, and C. McIntyre, “Computational analysis of subthalamic nucleus and lenticular fasciculus activation during therapeutic deep brain stimulation,” *J. Neurophysiol.*, vol. 96, pp. 1569–1580, 2006. 3.2
- [44] E. Richter, T. Hoque, W. Halliday, A. Lozano, and J. Saint-Cyr, “Determining the position and size of the subthalamic nucleus based on magnetic resonance imaging results in patients with advanced parkinson’s disease,” *J. Neurosurg.*, vol. 100, pp. 541–546, 2004. 3.2
- [45] K. W. McCairn and R. S. Turner, “Deep brain stimulation of the globus pallidus internus in the Parkinsonian primate: Local entrainment and suppression of low-frequency oscillations,” *J. Neurophysiol.*, vol. 101, pp. 1941–1960, Apr. 2009. 3.4
- [46] C. Hammond, R. Ammari, B. Bioulac, and L. Garcia, “Latest view on the mechanism of action of deep brain stimulation,” *Mov. Disord.*, vol. 23, pp. 2111–2121, 2008. 3.5
- [47] V. Grdinaru, M. Mogri, K. Thompson, J. Henderson, and K. Deisseroth, “Optical deconstruction of Parkinsonian neural circuitry,” *Science*, vol. 324, pp. 354–359, 2009. 3.5
- [48] C. Dejean, B. Hyland, and G. Arbuthnott, “Cortical effects of subthalamic stimulation correlate with behavioral recovery from dopamine antagonist induced akinesia,” pp. 1055–1063, 2009. 3.5
- [49] K. Nowak, E. Mix, J. Gimza, U. Strauss, K. K. Sriperumbudur, R. Benecke, and U. Gimza, “Optimizing a rodent model of Parkinson’s disease for exploring the effects and mechanisms of deep brain stimulation,” *Parkinson’s Dis.*, vol. 2011, pp. 1–19, Apr. 2011. 4.1, 4.3.3
- [50] R. J. Mandel, “Effect of acute L-Dopa pretreatment on apomorphine-induced rotational behavior in a rat model of Parkinson’s disease,” *Exp. Neurol.*, vol. 161, pp. 212–219, Jan. 2000. 4.2.1, 6.2

- [51] G. E. Meredith and U. J. Kang, “Behavioral models of Parkinson’s disease in rodents: a new look at an old problem,” *Mov. Disord.*, vol. 21, pp. 1595–1606, Oct. 2006. 4.2.1, 4.2.2
- [52] R. Q. So, G. C. McConnell, A. T. August, and W. M. Grill, “Characterizing effects of subthalamic nucleus deep brain stimulation on methamphetamine-induced circling behavior in hemi-Parkinsonian rats,” *IEEE Trans. Neural Syst. Rehabil. Eng.*, vol. 20, pp. 626–635, Sep. 2012. 4.2.1, 4.3.1, 4.3.3
- [53] L. Khachiyan, “Rounding of polytopes in the real number model of computation,” *Math. of Oper. Res.*, vol. 21, pp. 307–320, May 1996. 4.2.1
- [54] Y. H. Lin, A. H. Liu, Y. Xu, L. Tie, H. M. Yu, and X. J. Li, “Effect of chronic unpredictable mild stress on brain-pancreas relative protein in rat brain and pancreas,” *Behav. Brain Res.*, vol. 165, pp. 63–71, Nov. 2005. 4.2.3
- [55] A. J. Keeney and S. Hogg, “Behavioral consequences of repeated social defeat in the mouse: preliminary evaluation of a potential animal model of depression,” *Behav. Pharmacol.*, vol. 10, pp. 753–764, Dec. 1999. 4.2.3
- [56] E. Choleris, A. W. Thomas, M. Kavaliers, and F. S. Prato, “A detailed ethological analysis of the mouse open field test: effects of diazepam, chloriazepoxide and an extremely low frequency pulsed magnetic field,” *Neurosci. Biobehav. Rev.*, vol. 25, pp. 235–260, May 2001. 4.2.3, 4.3.2
- [57] C. Del Seppia, L. Mezzasalma, E. Choleris, P. Luschi, and S. Ghione, “Effects of magnetic field exposure on open field behavior and nociceptive responses in mice,” *Behav. Brain Res.*, vol. 144, pp. 1–9, Sep. 2003. 4.2.3, 4.3.2
- [58] A. Blokland, “Reaction time responding in rats,” *Neurosci. Biobehav. Rev.*, vol. 22, pp. 847–864, Oct. 1998. 4.2.4
- [59] L. Carnevali, F. Mastorci, G. Graiani, M. Razzoli, M. Trombini, M. A. Pico-Alfonso, R. Arban, A. J. Grippo, F. Quaini, and A. Sgoifo, “Social defeat and isolation induce clear signs of a depression-like state, but modest cardiac alterations in wild-type rats,” *Physiol. Behav.*, vol. 106, pp. 142–150, May 2012. 4.2.5
- [60] A. M. Kuncel, S. E. Cooper, B. R. Wolgamuth, and W. M. Grill, “Amplitude- and frequency-dependent changes in neuronal regularity parallel changes in tremor with thalamic deep brain stimulation,” *IEEE Trans. Neural Syst. Rehabil. Eng.*, vol. 15, pp. 190–197, Jun. 2007. 4.3.3
- [61] D. J. Pedrosa and L. Timmermann, “Review: management of Parkinson’s disease,” *Neuropsychiatry Dis. Treat.*, vol. 9, pp. 321–340, Mar. 2013. 4.5, 7
- [62] F. Sprenger and W. Poewe, “Management of motor and non-motor symptoms of Parkinson’s disease,” *CNS Drugs*, vol. 27, pp. 259–272, Apr. 2013. 4.5, 7

- [63] R. M. deSouza, E. Moro, A. E. Lang, and A. H. Schapira, “Timing of deep brain stimulation in Parkinson disease: a need for reappraisal?” *Ann. Neurol.*, vol. 73, pp. 565–575, May 2013. 4.5, 7
- [64] E. Brunenberg, P. Moeskops, W. Backes, C. Pollo, L. Cammoun, A. Vilanova, M. Janssen, V. Visser-Vandewalle, B. ter Haar Romeny and, and B. Platel, “Structural and resting state functional connectivity of the subthalamic nucleus: identification of motor STN parts and the hyperdirect pathway,” *PLoS One*, vol. 7, pp. 1–14, Jun. 2012. 5
- [65] D. Whitmer, C. de Solages, B. Hill, H. Yu, J. Henderson, and H. Bronte-Stewart, “High frequency deep brain stimulation attenuates subthalamic and cortical rhythms in Parkinson’s disease,” *Front. Hum. Neurosci.*, vol. 6, pp. 1–18, Jun. 2012. 5
- [66] J. P. Donoghue and J. N. Sanes, “Organization of adult motor cortex representation patterns following neonatal forelimb nerve injury in rats,” *J. Neurosci.*, vol. 8, pp. 3221–3232, Sept. 1988. 5.1
- [67] A. Kandel and G. Buszaki, “Cellular-synaptic generation of sleep spindles, spike-and-wave discharges, and evoked thalamocortical responses in the neocortex of the rat,” *J. Neurosci.*, vol. 17, pp. 6783–6797, Sept. 1997. 5.2
- [68] Chronux analysis software. [Online]. Available: <http://chronux.org/> 5.4, 5.6
- [69] P. Mitra and H. Bokil, *Observed Brain Dynamics*. Oxford University Press, 2008. 5.4, 5.6
- [70] C. M. Voge and J. P. Stegemann, “Carbon nanotubes in neural interfacing applications,” *Journal of Neural Engineering*, vol. 8, no. 1, p. 1001, Feb. 2011. 6
- [71] K. Wang, H. A. Fishman, H. Dai, and J. S. Harris, “Neural Stimulation with a Carbon Nanotube Microelectrode Array,” *Nano Letters*, vol. 6, no. 9, pp. 2043–2048, Sep. 2006. 6
- [72] E. W. Keefer, B. R. Botterman, M. I. Romero, A. F. Rossi, and G. W. Gross, “Carbon nanotube coating improves neuronal recordings,” *Nature Nanotechnology*, vol. 3, no. 7, pp. 434–439, Jun. 2008. 6
- [73] E. Jan, J. L. Hendricks, V. Husaini, S. M. Richardson-Burns, A. Sereno, D. C. Martin, and N. A. Kotov, “Layered Carbon Nanotube-Polyelectrolyte Electrodes Outperform Traditional Neural Interface Materials,” *Nano Letters*, vol. 9, no. 12, pp. 4012–4018, Dec. 2009. 6
- [74] Y. Lu, T. Li, X. Zhao, M. Li, Y. Cao, H. Yang, and Y. Y. Duan, “Electrode-deposited polypyrrole/carbon nanotubes composite films electrodes for neural interfaces,” *Biomaterials*, vol. 31, no. 19, pp. 5169–5181, 2010. 6

- [75] I. Yoon, K. Hamaguchi, I. V. Borzenets, G. Finkelstein, R. Mooney, and B. R. Donald, “Intracellular Neural Recording with Pure Carbon Nanotube Probes.” *PloS one*, vol. 8, no. 6, p. e65715, 2013. 6
- [76] S.-R. Yeh, Y.-C. Chen, H.-C. Su, T.-R. Yew, H.-H. Kao, Y.-T. Lee, T.-A. Liu, H. Chen, Y.-C. Chang, P. Chang, and H. Chen, “Interfacing Neurons both Extracellularly and Intracellularly Using Carbon Nanotube Probes with Long-Term Endurance,” *Langmuir*, vol. 25, no. 13, pp. 7718–7724, Jul. 2009. 6
- [77] N. Behabtu, C. C. Young, D. E. Tsentalovich, O. Kleinerman, X. Wang, A. W. K. Ma, E. A. Bengio, R. F. ter Waarbeek, J. J. de Jong, R. E. Hoogerwerf, S. B. Fairchild, J. B. Ferguson, B. Maruyama, J. Kono, Y. Talmon, Y. Cohen, M. J. Otto, and M. Pasquali, “Strong, Light, Multifunctional Fibers of Carbon Nanotubes with Ultrahigh Conductivity,” *Science*, vol. 339, no. 6116, pp. 182–186, Jan. 2013. 6.1
- [78] S. R. Summerson, B. Aazhang, and C. T. Kemere, “Characterizing motor and cognitive effects associated with deep brain stimulation in the gpi of hemiparkinsonian rats,” *under review for IEEE Trans. Neur. Sys. and Rehab.*, 2014. 6.2
- [79] C. Marin, “Biocompatibility of intracortical microelectrodes: current status and future prospects,” *Frontier in Neuroengineering*, vol. 3, 2010. 6.4.1
- [80] V. S. Polikov, P. A. Tresco, and W. M. Reichert, “Response of brain tissue to chronically implanted neural electrodes,” *Journal of Neuroscience Methods*, vol. 148, no. 1, pp. 1–18, Oct. 2005. 6.4.1, 6.4.2
- [81] K. A. Potter, A. C. Buck, W. K. Self, and J. R. Capadona, “Stab injury and device implantation within the brain results in inversely multiphasic neuroinflammatory and neurodegenerative responses.” *Journal of Neural Engineering*, vol. 9, no. 4, p. 046020, Aug. 2012. 6.4.1, 6.4.2
- [82] Y. Li, Y. Song, L. Zhao, G. Gaidosh, A. M. Laties, and R. Wen, “Direct labeling and visualization of blood vessels with lipophilic carbocyanine dye DiI.” *Nature protocols*, vol. 3, no. 11, pp. 1703–1708, 2008. 6.4.1
- [83] J. Subbaroyan, D. C. Martin, and D. R. Kipke, “A finite-element model of the mechanical effects of implantable microelectrodes in the cerebral cortex,” *Journal of Neural Engineering*, vol. 2, no. 4, pp. 103–113, Oct. 2005. 6.4.1
- [84] J. Harris and D. Tyler, “Biological, mechanical, and technological considerations affecting the longevity of intracortical electrode recordings,” *Critical Reviews in Biomedical Engineering*, 2014. 6.4.2
- [85] S. David and A. Kroner, “nrn3053,” pp. 1–12, Jun. 2011. 6.4.2

- [86] P. J. Murray and T. A. Wynn, “Protective and pathogenic functions of macrophage subsets.” *Nature reviews. Immunology*, vol. 11, no. 11, pp. 723–737, Nov. 2011. 6.4.2
- [87] E. J. Foster, C. Weder, and J. R. Capadona, “Curcumin-releasing mechanically adaptive intracortical implants improve the proximal neuronal density and blood-brain barrier stability,” *Acta Biomaterialia*, 2014. 6.4.2
- [88] M. B. Gingrich and S. F. Traynelis, “Serine proteases and brain damage—is there a link?” *Trends in neurosciences*, vol. 23, no. 9, pp. 399–407, 2000. 6.4.2
- [89] T. Saxena, L. Karumbaiah, E. A. Gaupp, R. Patkar, K. Patil, M. Betancur, G. B. Stanley, and R. V. Bellamkonda, “The impact of chronic blood-brain barrier breach on intracortical electrode function,” *Biomaterials*, vol. 34, no. 20, pp. 4703–4713, Jul. 2013. 6.4.2